Wesleyan University

Improvements in the Construction and Detection Electronics of a Third Sound Resonator Used for the Observation of Stimulated Condensation in Superfluid ^{4}He

by

Yudhiakto Pramudya

Faculty Advisor: Dr. Fred M Ellis

A Dissertation submitted to the Faculty of Wesleyan University in partial fulfillment of the requirements for the degree of Doctor of Philosophy

Middletown, Connecticut December, 2012

Abstract

The detection of amplification of third sound by stimulated condensation in superfluid helium requires a high resonance quality factor and high sensitivity to the third sound signal. For the first time, a clean resonator has been built without dust particles bridging the small gap of the detection electrode capacitor, and a procedure was developed to verify the gap's integrity. Due to this improvement, the highest quality factor of the third sound in the open disk design required for the stimulated condensation experiment has been obtained, and a significant improvement in evidence supporting the validity of the stimulated condensation gain has been achieved. However, several further issues preventing a clean observation of the effect remain. These include a thickness oscillation amplitude of the experimental third sound and disk mechanical resonance signals that is not consistent with theoretical predictions, and a film flow dissipation about five time higher than expected. Improvements in the detection electronics were made to help compensate for these issues: A method to observe the stability of the detector LC circuit as it cools down into its normal operating range was developed and used to verify the its intended condition, and several adjustments to the overall stability of the cryogenic detector circuit were implemented. In spite of these improvements, the cause of the anomalous dissipation in the superfluid remains unknown.

Acknowledgment

Alhamdulillah, I accomplish my study and research. Many people deserve my gratitude for helping my research work, both directly and indirectly.

I would like to express my deep appreciation and gratitude to my advisor, Prof. Fred Ellis, for the patient guidance and mentorship he provided to me. He trained me to be a good experiment physicist. He taught me the consequence of every action in the laboratory. He shows me different perspective to be a scientist which is also a social human being.

I would also like to thank my committee members, Prof. Tsampikos Kottos and Prof. Greg Voth for the guidance. Prof. Kottos gave me opportunity to work with him in my first semester at Wesleyan University. He introduced me the important of testing the theory to convinced ourself and maybe to found different results. Prof. Voth gave me advice and revision for writing a good dissertation. I was fortunate to assist him in the Solid State Course that give me opportunity to simulate the crystal structure.

During my work in the research laboratory, I got many help from the fellow graduate and undergraduate students. Thank you to Tobias Glasser for your time to discuss the superfluid theory and the pipeline in the laboratory. Thank you to James Aisenberg for composing the Visual Basic for interfacing. Thank you to Anand Swaminathan for partnership to run the experiment. Thank you to Joshua Eddinger through your work and presentation so I can understand several aspects of the experiment. Lastly, thank you to Joey Schindler for providing the cheerful discussion in the laboratory.

Without the machine staff expertise, I would have hard time to build my apparatus. They gave helpful idea how to design and construct may parts of experiment apparatus. They seems to have ability to read what I want then realized it in very good piece of work.

Many thanks to Dr. Luis Fernando Vargas Lara and Beatriz Pazmino for having relationship

more than friend. Dr. Pennan Chinnasammy deserves my thankful for having fun time together in the department and the outdoor activities. Thank you to Ramesh, Dr. Shabnam, Dr. Iulian, Dr. Blum, Dr. Susantha, Dr. Bodyfelt, Dr. Steve Coppage, Dr. Roy, Paula, Shima, Hamid and Neda, William. Thank you also to my ethnomusicology friends who gave me opportunity to learn and enjoy the art. I wish to thank to my Indonesian friends with very authentic relationship that makes me feel like home. Many thanks to Prof. Sumarsam and Mr. Harjito family.

Special thank you for my family in Indonesia who endlessly support my study. My lovely wife Asty and daughter Kirana are giving courage and motivation during the day and night, the snow and sunny weather, and during good and bad day in the laboratory. Thank you for your great support.

Contents

List of Figures

List of Tables

Chapter 1

Introduction

This chapter outlines the attempt to perform a third sound amplification by stimulated condensation on superfluids ^{4}He [1]. The amplification needs a high sensitivity of the electronic detection system. My doctoral research was focused on the development of detection sensitivity. I also have done several projects to understand the behavior of electronic instruments as part of the detection system.

The third sound amplification experiment has been done in our research group for more than a decade. The third sound is an important accoustic mode in superfluid helium for probing the state of thin adsorbed films. It is expected that it is possible to amplify the third sound mode by condensing incoherence helium atoms into the coherence ground state. This phenomena is similar to photon amplification in a laser. Hence, we view this phenomena as an example of a matter laser.

However, several problems have prevented us from observing significant amplification of third sound mode. The quality factor of the mode is not high. It only gives us a small percentage of amplification. Moreover, a low signal to noise ratio has maked the situation worse. In my research, I investigated possible factors that can lower the quality factor. Further, by developing the detection system and improving the resonator assembly process, I have improved the quality factor. I also calculated and took data of the electronic detection system to get a better understanding of the signal characteristics of the third sound mode.

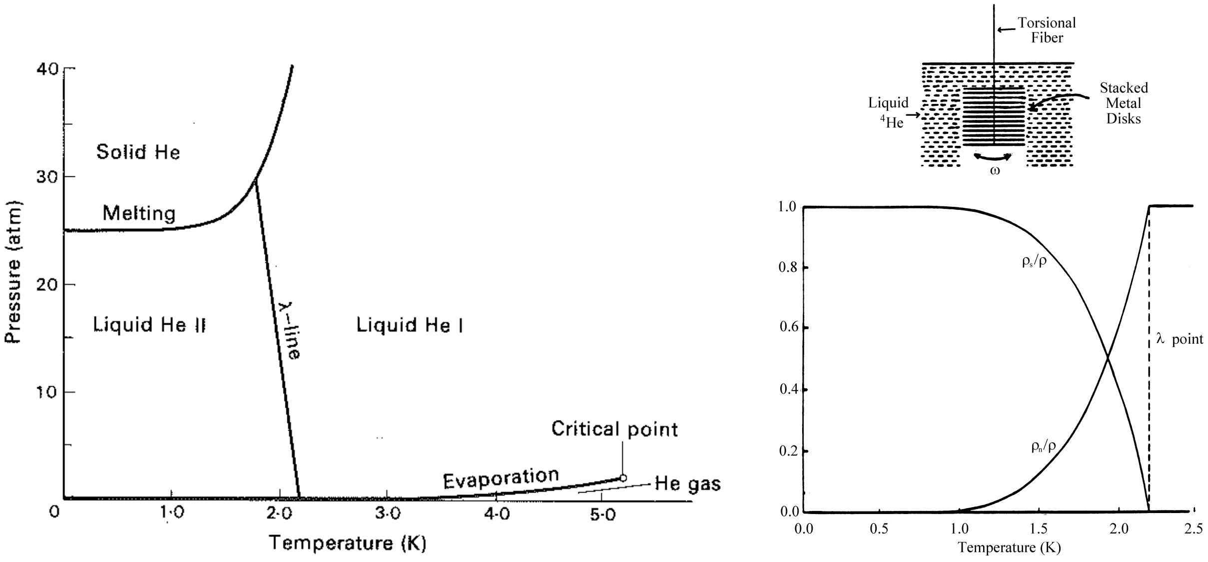

(a) (b)

Figure 1.1: The phase diagram of ^4He shown in figure 1.1(a). The Andronikashvili experiment set up and the plot of superfluid component density as a function of temperature is shown in figure 1.1(b).

1.1 Quantum fluids

Helium is an interesting chemical element. It remains in a liquid phase at absolute zero temperature. Helium can transform into a solid phase if we pressurize it to about 25 atmospheres or more as shown in figure 1.1(a). This behaviour results from a low mass and weak attraction between helium atoms along with quantum mechanics. We will see why quantum mechanics is important for understanding Helium at low temperature.

A helium particle momentum (p) can be calculated from Maxwell-Boltzmann distribution [2]

$$p = (2mk_BT)^{1/2} \tag{1.1}$$

which m, k_B and T are helium mass, Boltzmann constant and temperature, respectively. In quantum mechanics, momentum can be expressed as $p = h/\lambda$, which h and λ are Planck constant and de Broglie wavelength, respectively. Hence, we can write the thermal de Broglie wavelength as

$$\lambda_{dB} = \left(\frac{2\pi\hbar^2}{mk_BT}\right)^{1/2} \tag{1.2}$$

We have to consider that quantum effects will be dominant when the thermal de Broglie wavelength is comparable with other typical length scales in the liquid. For the case of ^{4}He, it is in its liquid phase below 4 K with a particle density of $1.881.10^{23} particles/m^3$. Hence, the λ_{dB} is about 0.4 nm which is larger than the typical interatomic distances (0.27 nm) [2].

Like other substances, ^{4}He has three different phases: gas, liquid and solid. ^{4}He's liquid phase is a unique phase. It can be divided into liquid I and liquid II. Liquid I behaves like a classical fluid. It flows with resistance. On the other hand, liquid II flows with no resistance. We called this phase the superfluid phase. The transition point from liquid I to liquid II is known as λ line. This lambda-like shape appears as singularity in the specific heat graph as a function of temperature. The lambda temperature at saturated vapor pressure is 2.17 K.

London recognized this lambda transition is related to the transition in the liquid which occurs in an ideal Bose Einstein gas at low temperatures [3]. As a quantum liquid, the liquid helium lambda point transition characteristics are not exactly the same as the transition in ideal Bose Einstein gas [4]. The specific heat of helium at low temperature is proprotional to T^3. On the other hand, the specific heat of the Bose-Einstein Condensation (BEC) is proportional to $T^{\frac{3}{2}}$. This is due to interparticle interaction in superfluid Helium that has a tendencey to lock the condensate particles instead of allowing the process of excitation. There is a simple change of slope of the specific heat versus temperature in the BEC case. The specific heat graph of helium has a much sharper feature [2].

1.1.1 Two fluid model

Liquid II, as a superfluid phase, can exhibit non-viscous properties. However, certain experiments showed that the superfluid can also have some fraction of viscous effect. One of the experiments was performed by Andronikashvili in 1946 [5]. He built an apparatus out of a pile of circular disks as shown in figure 1.1(b). It can rotate on its axis. He submerged it in liquid Helium and changed the temperature. Viscous fluid will increase the inertia and damp the disk oscillation. His results indicated that there was drop in the oscillation period at temperature below the T_λ. It means that there was some fraction of the superfluid that has viscosity and another fraction does not.

To explain the phenomenon, Tisza postulated in 1938 [6] (and Landau in 1941 [7]) that there are two types of components existing in the superfluid phase. They are superfluid component and normal component. This postulate is known as the two-fluid model. The superfluid component has no viscosity and is made up of the ground state of the system. Thermal excitations make up the normal component and give it viscous properties. Each component has an independent density and velocity. However, the two components are impossible to physically separate. The total density (ρ) is composed of the sum of the normal (ρ_n) and superfluid (ρ_s) density. The total current density ($\vec{j}$) obeys,

$$\vec{j} = \vec{j_s} + \vec{j_n} \tag{1.3}$$

which $\vec{j_s}$ and $\vec{j_n}$ are superfluid and normal current density, respectively. Since current density is a product of density and velocity, we can write the superfluid and normal current density as

$$\vec{j_s} = \rho_s \vec{v_s} \tag{1.4a}$$

$$\vec{j_n} = \rho_n \vec{v_n} \tag{1.4b}$$

which $\vec{v_s}$ and $\vec{v_n}$ are superfluid and normal component velocities, respectively. The normal component made up of excitations carries mass and entropy. The superfluid component only transports mass. At very low temperatures, the system is dominated by superfluid components as shown in figure 1.1(b).

The wavefunction of the system can be written as

$$\Psi_{total} = \Psi GS + \sum \Psi_{excitations} \tag{1.5}$$

which Ψ_{GS} is the ground state wavefunction. The expression of Ψ_{GS} is

$$\Psi_{GS} = \sqrt{\rho} e^{i\Phi(\vec{r})} \tag{1.6}$$

which $\Phi(\vec{r})$ is the phase of the ground state wavefunction. The superfluid component velocity can be calculated from the phase by this relation

$$\vec{v_s} = \frac{\hbar}{m_4} \vec{\nabla} \Phi(\vec{r}) \tag{1.7}$$

1.1.2 Third sound modes

The third sound mode was explained by K.R Atkins in 1959 [8] and observed by C.W.F Everitt, K.R. Atkins and A. Denenstein in 1964 [9]. It is similar to the shallow water mode. It has a very long wavelength compared to the film thickness as shown in figure 1.2. In shallow water, the restoring force is gravity force. However, the restoring force in the third sound mode is the van der Waals force. This force is the attractive force between helium atoms and the substrate. For very

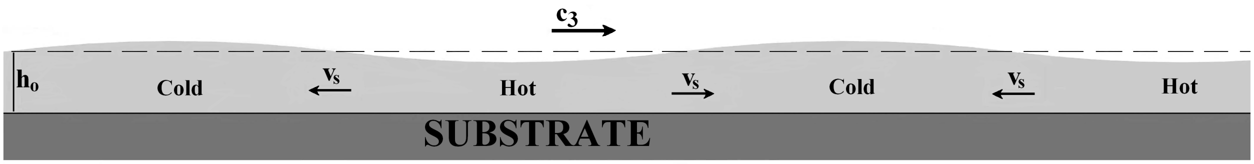

Figure 1.2: The third sound mode's wavelength is much bigger than the film thickness and film thickness oscillation amplitude. Temperature at the peaks is colder than the temperature at the troughs.

thin films, the van der Waals force is orders of magnitude bigger than the gravity force ($\approx 10^5$ for 3 nm film thickness). The shallow water wave speed c_{sw} is

$$c_{sw} = \sqrt{gh_0} \tag{1.8}$$

Due to viscosity, the normal component does not move if the superfluid helium film thickness (h_0) is much less than viscous penetration depth (δ). The viscous penetration depth can be expressed as

$$\delta = \sqrt{\frac{2\eta_n}{\omega\rho_n}} \tag{1.9}$$

which η_n are ω are normal component viscosity and film thickness oscillation frequency, respectively. The viscous penetration depth is about $2\mu m$. Hence, at the thickness of $3nm$, only the superfluid component can oscillate parallel to the substrate at velocity c_3.

Since only the superfluid component can oscillate and carry no entropy, there is thermal gradient induced between troughs and peaks. At the peaks, more superfluid component piles up relative to the normal component. It means the temperature at the peaks is colder than the temperature at the troughs. Third sound is also useful for several experiments that concern the probing of the superfluid component. That is the reason why our group focuses on the third sound mode in order to observe the amplification by stimulated condensation. This is done in a circular geometry.

The third sound mode on the circular disk that used in the experiment has a shape that can be derived from simplified hydrodynamic equations. Figure 1.2 shows the length scale of the third sound mode's wavelength and thickness oscillation amplitude that permits us to neglect the nonlinear component of velocity in the euler equation [10]. The continuity equation in the superfluid helium film is

$$\rho\frac{\partial h}{\partial t} = -h_0\left(\vec{\nabla}.\vec{v_s}\right)\rho_s \tag{1.10}$$

It means that the rate of thickness oscillation $\left(\frac{\partial h}{\partial t}\right)$ increase is proportional to the rate of superfluid component entering a region. We also use the force equation for the superfluid component. It is

$$\frac{\partial \vec{v_s}}{\partial t} = -\vec{\nabla}\mu = -g_v \vec{\nabla} h \tag{1.11}$$

where μ is chemical potential and g_v is the van der Waals force per unit mass, respectively. We differentiate equation 1.10 wih respect to t and find the gradient of equation 1.11. Hence, we have these equations

$$\rho \frac{\partial^2 h}{\partial t^2} = -h_0 \frac{\partial}{\partial t}\left(\vec{\nabla}.\vec{v_s}\right)\rho_s \tag{1.12a}$$

$$\frac{\partial \vec{\nabla}.\vec{v_s}}{\partial t} = -g_v \vec{\nabla}^2 h \tag{1.12b}$$

Eliminating the divergence, we can construct the following equation

$$\vec{\nabla}^2 h - \frac{\rho}{\rho_s}\frac{1}{g_v h_0}\frac{\partial^2 h}{\partial t^2} = 0 \tag{1.13}$$

Equation 1.13 is the wave equation with the third sound speed (c_3)

$$c_3 = \sqrt{\frac{\rho_s}{\rho} g_v h_0} \tag{1.14}$$

Hence, the equation 1.13 becomes

$$\nabla^2 h - \frac{1}{c_3^2}\frac{\partial^2 h}{\partial t^2} = 0 \tag{1.15}$$

We look for solution of equation 1.15 with harmonic time dependence. Assuming the thickness oscillation is

$$h(x,t) = h(x)e^{-i\omega t} \tag{1.16}$$

we insert the thickness oscillation solution to equation 1.15 and divide by $e^{-i\omega t}$ to get

$$\nabla^2 h(x) + k^2 h(x) = 0 \tag{1.17}$$

with k is equal to $\frac{\omega}{c_3}$. In the cylindrical coordinates, the solution is

$$h = h_m J_m(kr) e^{im\phi} \tag{1.18}$$

with integer m, J_m are Bessel function of first kind.

We look for solutions on a free disk. Since the film coats the top and bottom surfaces of the disk, there are two modes due to the boundary condition between the top and bottom surfaces. They are symmetric and antisymmetric modes. For the symmetric mode, the thickness oscillation

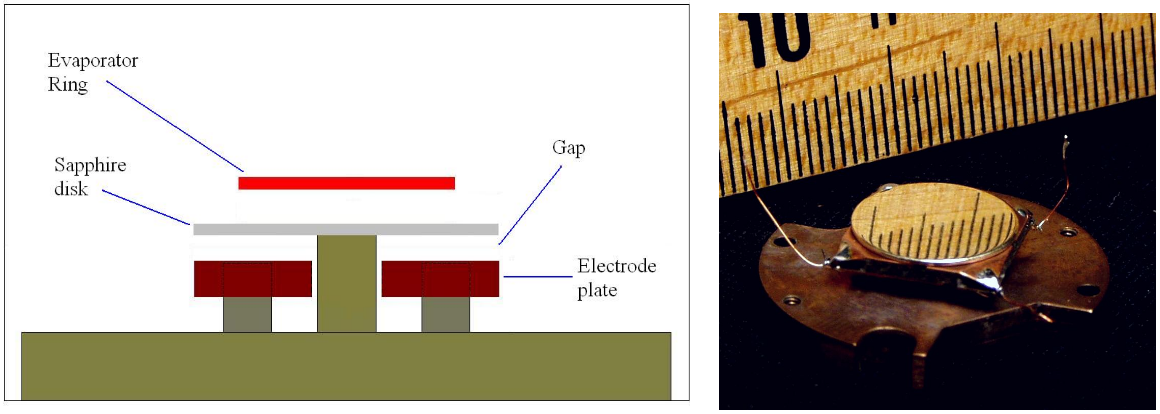

(a)

(b)

Figure 1.3: The schematic of the cell is shown in figure 1.3(a). Figure 1.3(b) shows the actual picture of resonator.

for the top and bottom surface has to be the same. It can be achieved if and only if the derivative of thickness oscillation with respect to r has to be zero at $r = a$. It means that $\frac{\partial J_m}{\partial r}|_{r=a} = 0$. The boundary condition for antisymmetric mode is $h_{top} = -h_{bottom}$. Hence, the solution for the boundary condition is $h = 0$ or $J_m(kr) = 0$ at $r = a$.

The full solution for the thickness oscillation is then

$$h_{m,n,s}(r,\phi,t) = \eta_{m,n,s}\, J_m(k_{mns}r)\, e^{im\phi}\, e^{-i\omega_{mns}t} \tag{1.19}$$

which $\omega_{mns} = c_3 k_{mns} = c_3 \frac{x_{mns}}{a}$ and a is the disk radius. The values of $x_{mns}$are the n-th zero of $J'_m(x_{mn})$ or $J_m(x_{mn} - 1)$, where s is +1 and -1 for symmteric and antisymmetric mode, respectively. η_{mns} is the mode amplitude.

The superfluid component velocity ($\vec{v_s}$) for the m, n, s mode can be calculated from the equation 1.11 and 1.14 and assume that $\vec{v_s}$ in the form of $v_s exp(-i\omega t)$. It is

$$\vec{v_s} = \frac{\rho}{\rho_s}\, c_3\, \frac{\vec{\nabla}.h}{i\, k_{mns}\, h_0} \tag{1.20}$$

These are modes of a free disk. The supported disk has a post at $r = 0$ on the lower surface as shown in figure 1.3(a). Previous work has shown that the modes are slightly different from the free disk [1]. But it showed that there is inherent dissipation.

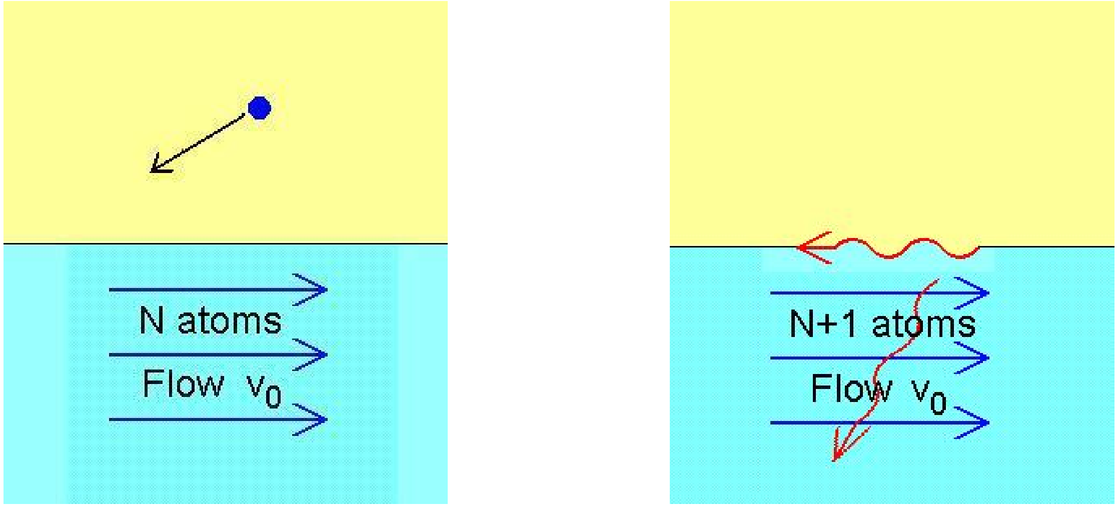

Figure 1.4: The initial condition in which there are N atoms moving in the same speed. The helium vapor atom condensed into N atom helium film and joined with them with the same speed. The excitation energy and momentum are carried by phonon, ripplon and roton.

1.2 Third sound amplification

The amplification of a persistent current of superfluid helium has been demonstrated by the group of Henkel et al [11]. By adding more helium atoms to a moving superfluid helium film, they showed that the angular momentum of a rotating persistent current was increased. This result motivated us to do similar experiments to continuously amplify the third sound mode by condensing helium atoms to the moving superfluid of the helium film acoustic mode.

1.2.1 Helium atom condensation

The superfluid component wavefunction can be written in term of condensate wavefunction. It is a condensate of helium atoms in the ground state that coherently move together with speed $\vec{v_s}$. The wavefunction of N helium atoms in the superfluid helium is Ψ_{GS}. A helium vapor atom condensing into the superfluid helium film has to join the local flow of N helium atoms in the film. Hence, the wavefunction becomes $\Psi_{GS} + \psi_{excitations}$. The excitation needs to be included in the wavefunction since the condensation process has to obey energy and momentum conservation. The excitation wavefunction is composed of phonons, ripplons, or rotons. A phonon is the elementary excitation of a compressional vibrations, the ripplon is the excitation of surface ripples of the film, and the roton

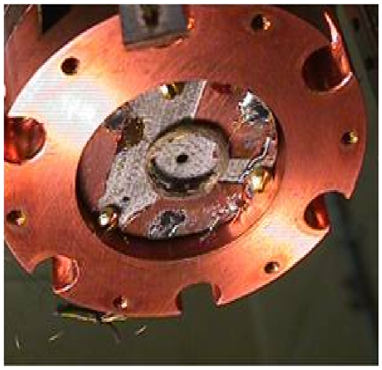

Figure 1.5: The evaporator ring to produce helium vapor atom.

is an excitation due to relative motion between neighboring helium atoms, similar to the rotation of a small ring of atoms [12]. Looking back to the equation 1.6, the condensation will not change the phase of the ground state wavefunction since the ground state wavefunction is a macroscopic wavefunction. It only changes the excitations, preserving the local $\vec{v_s}$.

Figure 1.5 shows the an evaporator ring placed above the disk to produce helium vapor atom. The evaporator ring power controls the condensation rate. The third sound amplification is proportional to the power since the additional helium atoms will add energy to the system.

1.2.2 Gain and quality factor

The third sound mode amplification comes from energy gained by condensing helium atoms coherently into the moving superfluid helium film. The effect of energy gain is to cancel the inherent dissipation of the third sound mode. Eventually, we will reach the self-oscillation condition if the energy gain is larger than energy loss. The dissipation is an inverse of quality factor of the third sound resonance. Hence, the goal for the stimulated condensation experiment is to observe significant quality factor (Q) changes as we condense more helium atoms. The negative dissipation (gain) by atom condensation is proportional to the ratio between the average of kinetic energy amplification rate and the average of kinetic energy. The total dissipation is the sum of all dissipations and gain. It is

$$\frac{1}{Q} = \frac{1}{Q_0} - \frac{m_4 \int_{top} \Phi v^2 dA}{\omega\rho\, h \int_{top} v^2 dA} \tag{1.21}$$

which Φ,v,ω are vapor flux on top of the disk, third sound speed and third sound frequency. It also can be expressed as a function of heater power [1]. It is

$$\frac{1}{Q} = \frac{1}{Q_0} - \frac{P}{0.07W} \tag{1.22}$$

The energy loss contributions come from thermal and non-thermal contribution. The thermal dissipation is the dissipation that depends on the temperature. We also call it as a normal component dissipation since the normal component carries entropy. The thermal dissipation is composed by substrate, vapor and lateral dissipation. The substrate dissipation Q_{st} comes from the temperature gradient between film and substrate. Its expression as a function of temperature is obtained by fitting the quality factor as a function of temperature from vast c_3 data set collected by Fred Ellis. It is

$$\frac{1}{Q_{st}} = \frac{T}{43000} \tag{1.23}$$

The thermal gradient between film and vapor contributes to the vapor dissipation (Q_{vt}). The vapor quality factor expression is [1]

$$\frac{1}{Q_{vt}} = \frac{1}{Q_{vq}} \left(\frac{\omega_{mn}}{\gamma(T)} + \frac{\gamma(T)}{\omega_{mn}} \right)^{-1} \tag{1.24}$$

Q_{vq} reflects a ratio between mechanical energy to thermal energy in the film. ω_{mn} is the frequency of the $(m, n)^{th}$ mode of third sound and $\gamma(T)$ is the thermal relaxation rate due to vapor coupling. The film temperature changes due to evaporator power can be calculated as

$$T_f = T_0 + R\frac{1}{2\pi a^2}P \tag{1.25}$$

which T_0 and T_f are the unheated and heated film temperatures and R is the Kapitza resistance between helium film and substrate [13], respectively. The effective heating power on the film temperature change is about one third of the evaporator loop power since only a part of the flux from the evaporator ring hits the disk.The last part of the thermal disspiation is the lateral dissipation (Q_{lat}). It comes from the lateral motion of the superfluid component while the normal component is clamped to substrate. This lateral motion induces the thermal gradient between the trough and the peak of the wave. We exclude the lateral disspiation in the total dissipation.

The non-thermal contribution to the total dissipation is composed by post radiation, vortex drag and gap bridge dissipation. The inherent dissipation comes from the post that support the disk on the lower surface. We could reduce it by reducing the diameter of the post. But, the consequence is the disk become less stable. The defects on the disk surface create vortex drag dissipation (Q_{vor}). We expect that this dissipation is very small ($Q_{vor} = \infty$). The dirt that can bridging the capacitor gap also contributes to the non-thermal dissipation. The liquid can wick into the gap assisted by the dirt that makes the gap bridge dissipation (Q_{gap}) bigger.

We need to have small inherent energy dissipation to get self-oscillation. It means that we have to have high quality factor contribution from the vortex. We are unable to control the thermal (Q_{st}) and (Q_{vt}) since they are thermal interaction characteristic of the film and substrate and vapor. The post dissipation also have limitation since there is competition between the stability and the loss reduction. However, we could improve Q_{gap}. Figure 1.6(a) shows the dissipation ($\frac{1}{Q}$) as a function of evaporator power for low and high dissipation with temperature dependence. The temperature dependent quality factor will bring the loss back up again at high evaporator power since the film temperature is increasing.

With the same amount of other quality factor contribution, the smaller non-thermal dissipation (the bigger non-thermal quality factor) shows a more obvious quality factor change due to gain. If it is large enough, we could easily see the self-oscillation. The self-oscillation regime or negative energy loss can be easily achieved with large non-thermal quality factor as shown in figure 1.6(a). Figure 1.6(a) also gives us a picture of how difficult the experiment to achieve self oscillation. Figure 1.6(b) shows that we only see small fraction of quality factor changes as we turn heating power on when we have large non-thermal dissipation.

We have to reduce the noise by making the resonator and electronic detection system mechanically more stable. We have improved Q_{gap} but Q_{vor} still give us problem. The vortex damping still high. The superfluid also has small critical velocity. We need to have good thermal contact between film and the substrate to improve quality factor from thermal contribution.

1.3 Electronic detection

A second major project that I have completed during my doctoral research is the analysis of the electronic detection sensitivity. We need to achieved a high signal to noise ratio and also need to understand the behavior of each piece of electronics chain as they are connected together in a more complicated circuit. In the end, the experimental signal is compared with the theoretical prediction and expressed as the sensitivity ratio of the detection system. The ratio differing from unity in

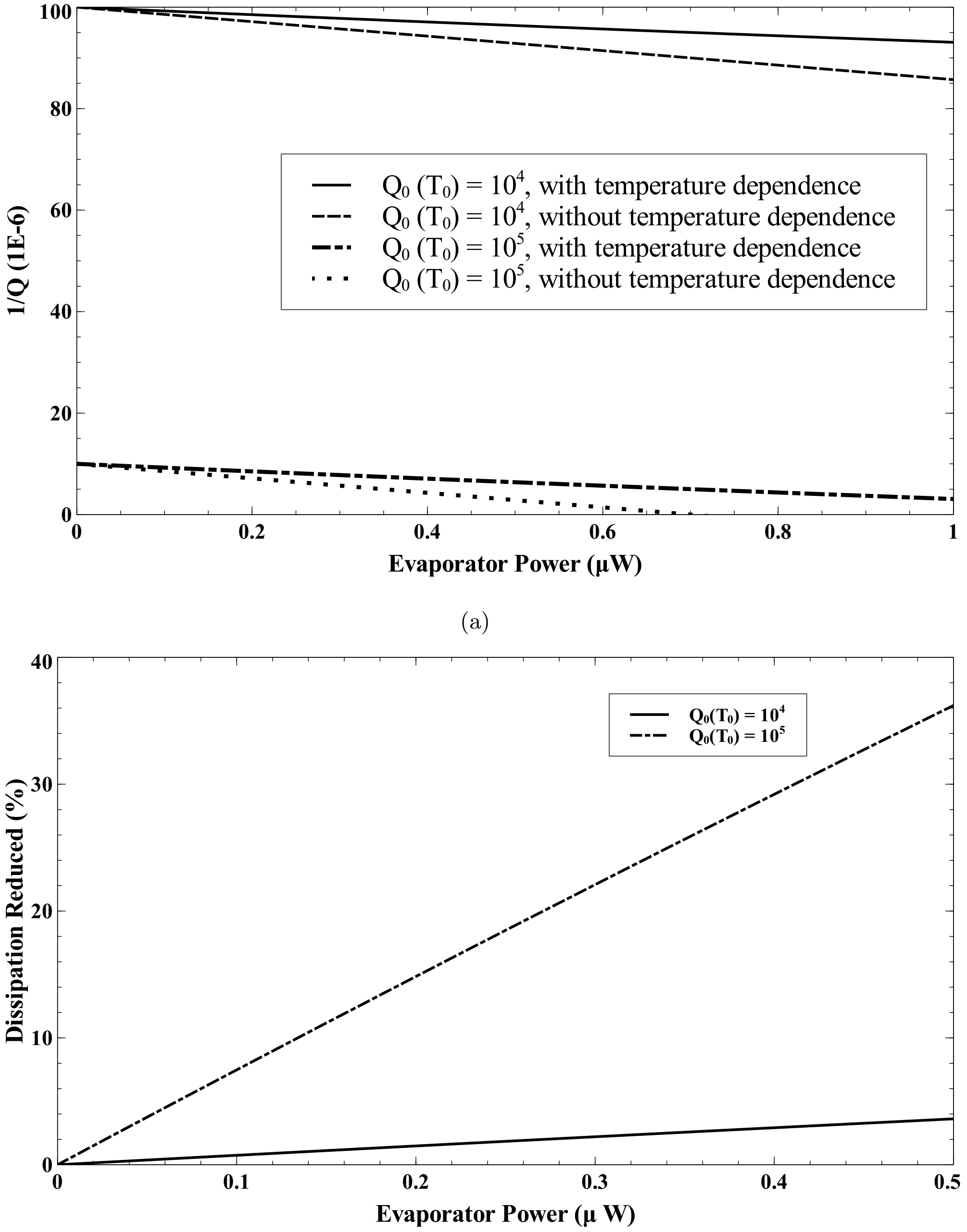

(a)

(b)

Figure 1.6: The graph of energy dissipation ($\frac{1}{Q}$) as a function of evaporator power for small quality factor (10^4) is shown in figure 1.6(a). The graph of energy dissipation as a function heating power for large quality factor (10^5) is shown in figure 1.6(a). As the heater power increasing, the film temperature is increasing. (c) The graph of loss reduced percentage as a function of evaporator power for low and high quality factor. The typical evaporator power of the stimulated experiment is about 0.5 μW.

magnitude or phase can be caused by several problems, but falling into two major areas. First, the theoretical model is not the same as the actual condition of the resonator/electrode geometry. Second, the model is not exactly the same as the actual electronic detection gain.

1.3.1 Capacitive detection

The third sound mode can be excited by applying an electric field to the film. The two drive capacitors are responsible for this work. The gradient of the electric field at the capacitor edges will produce the force to the helium film. The electrostatic force make the film thickness oscillation happen.

The film thickness oscillation is measured by monitoring the pick-up capacitor capacitance changes. We connect the capacitor to an inductor and is driven by tunnel diode to make an Tunnel Diode Oscillator (TDO) that can transmit carrier frequency around 74 MHz. The carrier frequency could have interference interaction with an external frequency. It becomes a serious issue if the amplitude of the external frequency is large. It would affect to lock-in the signal to the local frequency. Hence, the third sound signal that we detect is inaccurate. The accuracy of the signal is also influenced by how we know the drive voltage that we apply to the drive capacitor. The drive signal comes from voltage generator. It is connected to the transfomer. The transformer has 1:3 turns ratio. Later, we call this transformer the "3X-Box". Another function of the 3X-Box is to isolate the signal generator to the electronic circuit inside the cryostat.

Calculation of film thickness oscillation also depends on the theoretical model of resonator geometry. We can identify several sources of discrepancy between the model and the actual resonator geometry. There is no precise measurement of the disk curvature. We only assume that the edge of the disk is not sharp and has a smooth curvature. The exact value of the actual radius will improve the model. During the assembly process, there is a possibility that the post of the disk is in improper condition. It can be off-center. That would make the symmetrical model irrelevant. The capacitor gap size need to be uniform for four sides of the resonator. If the disk and electrode are in the tilted position, we will have different gap sizes for four sides of the resonator.

We need to construct the resonator in a proper electrical contact to achieve high sensitivity. The electrical connection between different parts in the resonator must be in good condition during the experiment. We cooled the resonator from room temperature to temperature less than 1K.

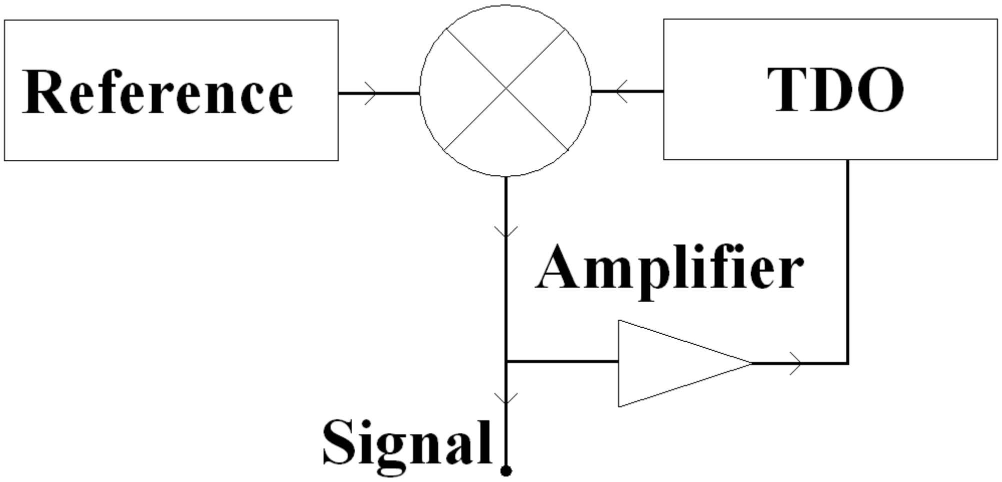

Figure 1.7: The block diagram of phase-lock loop.

Each part of resonator has a different thermal expansion coefficient that could apply more stress to the electrical connection. It would make several cracks in several places in the cell and eventually will add more to the stray capacitance.

1.3.2 Demodulation TDO frequency

The thickness oscillation signal is a frequency modulation coming from a changing of capacitance. Phase-locked loop (PLL) is a standard procedure to change frequency modulations by comparing modulated parameter with reference parameter. In other words, comparing the TDO frequency and known local frequency. Any phase difference between TDO and local frequency will be used to correct the modulation frequency. This correction is known as feedback loop. This is the way to make the TDO locked to the local/reference oscillator. This correction is also the thickness oscillation signal. Another path from mixer that carry this information goes to The Digital Signal Processing (DSP) lock-in. It shows the magnitude and phase of modulation signal.

The PLL can accept and lock a range of signal frequencies. This range is the lock-in range. In the experiment, we set our carrier frequency right in the center of lock-in range. This is to make sure that during the measurement, we will not reach the out of lock-in range. We do not want to have small lock-in range. That is the reason why we also need good electronic stability for doing measurement.

Chapter 2

Third Sound Resonator

This chapter outlines the theoretical calculation of film oscillation amplitudes and disk vibration amplitudes. The film oscillation is in the third sound mode. The amplitude of film oscillation can be measured using the fitted experimental value of the resonance profile and this calculation. The calculation is based on the Bessel function solutions of film oscillations on the circular plate driven electrostatically. The experimental value of film oscillation amplitude compared with the theoretical value is what we call the sensitivity ratio. It gives information to how well the experimental results matches the theoretical value. The mechanical resonance analysis of the disk is based on a similar calculation of the circular disk vibration [14], and used as a confirmation of the mechanical integrity of the apparatus.

2.1 Sensitivity ratio of third sound

2.1.1 The disk geometry

The third sound mode signal is driven and detected capacitively. The capacitor is composed of a sapphire disk supporting the third sound and an electrode. The electrode is made of a 12.7 mm circuit board that was divided into four areas (the dark areas in figure 2.1(a)). Those four segments are 2 drive areas (D) and 2 pickup areas (P). They are contructed by removing thin layer of copper in such away that the side of D is coincide with the center line (C/L). The 2 pickup segments are connected together via lower side of the circuit board. The hole in the center of electrode is created for the disk post so the electrode can be placed under the disk. The distance between the

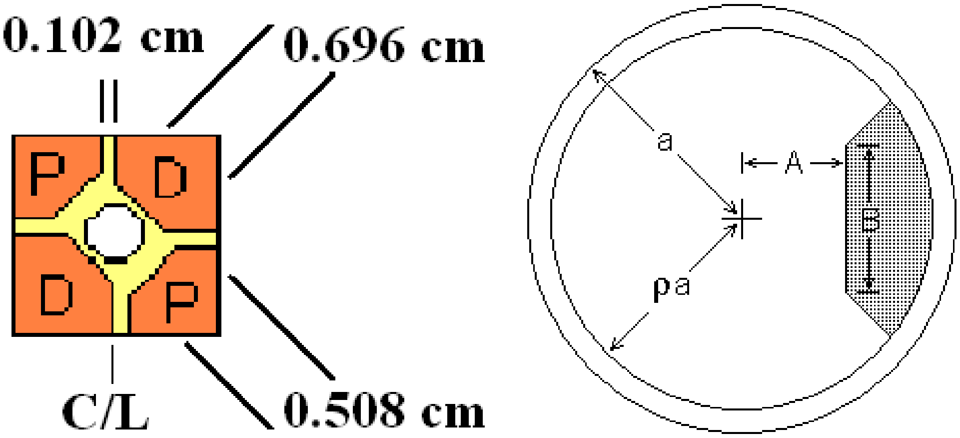

(a) disk

(b) electrode

Figure 2.1: a. The electrode geometry shows the four areas that consists of two drive and two pickup areas. b. The disk geometry with the effective radius due to edge curvature correction.

lower surface of the disk and the electrode is about $30\mu m$ as confirmed in the chapter 5. The figure 1.3(a) shows the schematic of the disk that is supported by the post and the base. It also shows the arrangement of the disk and the electrode.

The disk picture can be seen in figure 2.1(b). The disk has an outer radius of 6.5 mm and a thickness of 0.5 mm. It is coated with silver and electrically grounded. To simplify calculation of the wave function in the boundary, we treat half of the disk thickness as an additional radius. This is checked by comparing the exact wave solutions for the thin cylindrical disk to a perfectly flat disk. The wave solutions of the thin cylindrical disk with thickness w is match with the wave solution of the flat disk with additional radius of $0.5w$. The effective radius of the disk (a) is 6.75 mm. All dimensions are scaled to this radius. Since the edge of the disk is not sharp, we need to make a correction to the capacitance due to curved shape as shown in figure 2.2. The correction is a fraction of the actual radius forming the small gap of the electrode. Its value is 0.92, determined optically. The correction of the disk edge also defines the capacitor outer radius. Hence, the effective capacitor radius (ρ) is 0.88 times effective radius of the disk. The shaded area of the disk figure is overlap with the dark segment in the electrode. The distant A on the disk is a half of the distant between two drive segments.

The disk capacitance geometry can be defined by two additional dimensions determined by the electrode dimensions: the inner edge distance from the center (A) and the length of this inner edge

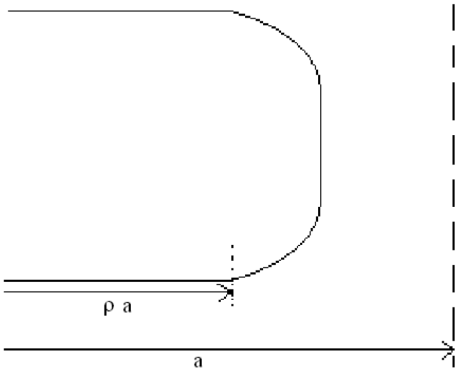

Figure 2.2: The effective radius (a) and the curvature shape of the disk edge.

(B). The outer edge is at the effective capacitor radius (ρ) and the sides extend at 45° between the inner edge and outer radius. For the drive electrode,

$$A = \frac{5.08\,mm}{2a}$$
$$B = \frac{5.08\,mm}{a}$$

For the pickup electrode,

$$A = \frac{6.96\,mm}{2\,a}$$
$$B = \left(\frac{6.96\,mm}{a} - \frac{2\sqrt{2}\,1.016\,mm}{a}\right)$$

The electrode is centered on the lines bounding the drive electrode as shown in figure 2.1(a). We also calculate the value, C, at the intersections of the 45° line and the circle at ρ. We find

$$C = \frac{(2A - B) + \sqrt{8\rho^2 - (2A - B)^2}}{4} \tag{2.1}$$

The scaled area of pickup electrode can be calculated as sum of the trapezoid area and the segment area shown in figure 2.3. The area of the pickup electrode in each quadrant is the sum of those two pieces.

$$A_{trapezoid} = \frac{1}{2}(C - A)\left(\frac{B}{2} + C - A + \frac{B}{2}\right) \tag{2.2}$$

$$A_{segment} = \frac{\rho^2}{2}\,acos\left(\frac{C}{\rho}\right) - \frac{1}{2}C\sqrt{\rho^2 - C^2} \tag{2.3}$$

The total area of the pickup electrode, consisting of both sides "P" in figure 2.1(a) is then

$$A_p = 2a^2\left((C - A)(B + C - A) + \rho^2\left(acos\left(\frac{C}{\rho}\right) - \frac{C}{\rho}\sqrt{1 - \frac{C^2}{\rho^2}}\right)\right) \tag{2.4}$$

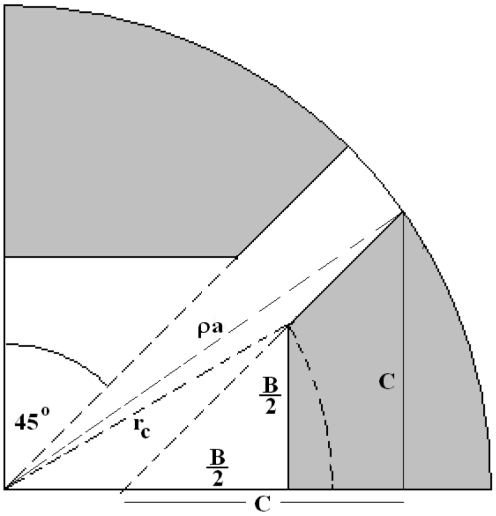

Figure 2.3: The area of trapezoid and segment of pickup area on the disk. The side line of the trapezoid is line up with the off-center 45° line.

2.1.2 Drive and pick-up integral

Based on the wave mode calculation in chapter 1, we can write the geometrical overlaps of the third sound mode with the electrodes. That is an integration over region exposed to the uniform gap of the parallel plate weighted by the wave amplitude function, for either the drive or pickup electrodes.

$$D, P = \frac{1}{\pi a^2} \int_{electrode} J_m(kr) e^{im\phi} dA \tag{2.5}$$

The D and P are normalized to the disk area (πa^2), making them a unitless measures of the mode overlay with the electrodes. The integration of D and P can be split into two parts. For the first part, we integrate the function from $r = A$ into $r = r_c$, where r_c is the hypotenuse of the triangle $OA\frac{B}{2}$ as shown in figure 2.3. The second part is integration from $r = r_c$ into $r = \rho$. The total value of D and P is the the sum of two parts. They are

$$p_1 = \int_A^{rc} J(m, x_m r)\, sin \left(m\, acos \left(\frac{A}{r} \right) \right) rdr \tag{2.6a}$$

$$p_2 = \int_{rc}^{\rho} J(m, x_m r)\, sin \left(m \left(\frac{\pi}{4} - asin \left(\frac{A - \frac{B}{2}}{\sqrt{2} r} \right) \right) \right) rdr \tag{2.6b}$$

We can write the integrand for three different values of m

For m > 0 and odd, P is zero since the thickness oscillation is antisymmertrical and the two sides of the pickup electrode are symmetric with respect to inversion of r.

For m > 0 and even:

$$rc = \sqrt{A^2 + \left(\frac{B}{2}\right)^2} \tag{2.7}$$

$$p_1 = \int_A^{rc} J(m, x_m r)\, sin\left(m\, acos\left(\frac{A}{r}\right)\right) rdr \tag{2.8}$$

$$p_2 = \int_{rc}^{R} J(m, x_m r)\, sin\left(m\left(\frac{\pi}{4} - asin\left(\frac{A - \frac{B}{2}}{\sqrt{2}r}\right)\right)\right) rdr \tag{2.9}$$

Which x_m is the zero of the first derivative of the Bessel function for symmetric modes and the zero of the Bessel function for antisymmetric modes. Hence, P is $\frac{4}{m\,\pi}(p1 + p2)$.

For m = 0

$$p_1 = \int_{A_p}^{rc} J(m, x_m r)\, acos\left(\frac{A}{r}\right) rdr \tag{2.10}$$

$$p_2 = \int_{rc}^{R} J(m, x_m r)\, \left(\frac{\pi}{4} - asin\left(\frac{A - \frac{B}{2}}{\sqrt{2}r}\right)\right) rdr \tag{2.11}$$

So, P is $\frac{4}{\pi}(p1 + p2)$.

For the D, we use the A and B parameters for the drive electrode. D has three different values that depend on m. They are

For m > 0 and odd, D is zero

For m > 0 and even: $D = \dfrac{2\, exp\left(im\left(\frac{\pi}{2}\right)\right)}{m\pi}(p_1 + p_2)$

For m = 0, $D = \dfrac{2}{\pi}(p_1 + p_2)$

2.1.3 Gap calibration

The capacitor gap could expand or shrink as we change temperature. It impossible to measure the gap size once we put the resonator into the cell. Hence, we need calculation of the gap size based on TDO frequency changes. The inductor, capacitor and equivalent resistor of tunnel diode will oscillate at the TDO frequency. The frequency will change if capacitance changes. Hence, as we fill the capacitor gap with liquid helium or nitrogen, the TDO frequency will shift down. The shift of the frequency can be used to calibrate the gap size of capacitor. The total capacitor is composed of the pick-up capacitor (C_p) and additional stray (C_s) capacitance as shown in figure 2.4. The stray capacitance is any capacitance except C_p. It is the capacitance of any small separations between different metal surfaces, for example the capacitance between the resonator base and the electrode.

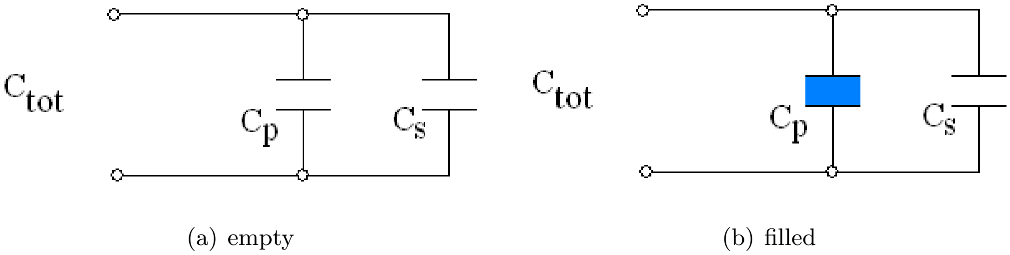

(a) empty (b) filled

Figure 2.4: The C_p and C_s when the gap is empty and filled with liquid.

The empty tunnel diode ferquency and filled tunnel diode frequency are

$$f_{empty} = \frac{1}{\sqrt{L\left(C_p + C_s\right)}} \tag{2.12a}$$

$$f_{filled} = \frac{1}{\sqrt{L\left(\epsilon_{He}\, C_p + C_s\right)}} \tag{2.12b}$$

which L is the TDO inductor. We assume that only capacitor that changes its capacitance as we fill the gap with liquid is the pickup capacitor. Since the smallest gap ($30\mu m$) is the pickup capacitor gap. As the gap filled with liquid, the TDO frequency changes significantly with small amount of liquid addition. It only can be achieved by filling a small gap. From equation 2.12a and 2.12b, we can find

$$cpr = \frac{C_p}{C_p + C_s} = \frac{\left(\dfrac{f_{empty}}{f_{filled}}\right)^2 - 1}{\epsilon_{He} - 1} \tag{2.13}$$

which *cpr* is the ratio between the pickup capacitance and the total capacitance. Hence, the pickup and the total capacitances are

$$C_p = cpr\, C_{tot} \tag{2.14}$$

$$C_{tot} = C_p + C_s = \frac{1}{\left(2\pi f_{empty}\right)^2 L} \tag{2.15}$$

From the value of pickup capacitance, we can calculate the capacitor gap, d, between electrode and the disk.

$$d = \frac{\epsilon_0 A_p}{C_p} \tag{2.16}$$

2.1.4 Mode details

From experiment, we can extract information about the drive frequency, quality factor, amplitude, and phase of a driven third sound signal. Based on the frequency and mode, we can calculate theoretical value of mode sensitivity, in Hz/nm, of the TDO. We start from the capacitance changes as the film thickness changes. The capacitance change of each plate element is found from the series combination of the vacuum and film sections of the electrode element. This value is integrated for the parallel capacitance of all the elements. This will be valid if the wavelength of the film shape mode is much greater than the gap.

The thickness shape at the peak of an oscillatory cycle is

$$\eta(r,\phi) = \eta_{m,n}\Psi_{m,n}(r,\phi) \tag{2.17}$$

where η is the oscillatory amplitude. The change of each capacitance element with area dA is

$$dC = \frac{1}{\dfrac{1}{\dfrac{\epsilon_0\, dA}{d-\eta_{m,n}(r,\phi)}} + \dfrac{1}{\dfrac{\epsilon_{He}\, dA}{\eta_{m,n}(r,\phi)}}} - \frac{\epsilon_0\, dA}{d} \tag{2.18}$$

We can simplify the above equation by taylor expanding for small η into

$$dC = \frac{\epsilon_0}{d^2}\left(1-\epsilon_{He}^{-1}\right)\eta_{m,n}(r,\phi)dA \tag{2.19}$$

So, integrating over all parallel elements, the total change is the integral over drive or pickup.

$$dC = \frac{\epsilon_0}{d^2}\left(1-\epsilon_{He}^{-1}\right)\eta\int\Psi_{m,n}(r,\phi)dA \tag{2.20}$$

The integration in equation 2.20 for drive and pick-up capacitor are the quantities D and P of equation 2.5.

$$dC_D = \frac{\epsilon_0\pi a^2}{d^2}\left(1-\epsilon_{He}^{-1}\right)\eta D \tag{2.21a}$$

$$dC_P = \frac{\epsilon_0\pi a^2}{d^2}\left(1-\epsilon_{He}^{-1}\right)\eta P \tag{2.21b}$$

As the mode is driven, the applied voltage interacts with each oscillators mode. We are interested in only motion of one mode, the m,n^{th} assuming this mode rigidly interacts with its electrostatic energy. We calculate the electrostatics energy change of the drive plate including the work done by the voltage source at V_D.

$$dU_{elect} = \frac{1}{2}dC_D V_D^2 - V_D dQ \tag{2.22}$$

We substitute dQ with $dC_D V_D$. So, the equation 2.22 becomes

$$dU_{elect} = -\frac{1}{2}dC_D V_D^2 \tag{2.23}$$

We plug equation 2.21a into equation 2.23

$$dU_{elect} = -\frac{\epsilon_0 \pi a^2 V_D^2}{2d^2} \left(1 - \epsilon_{He}^{-1}\right) \eta D \tag{2.24}$$

For the next calculation, we calculate the Van der Waals energy of the film. We integrate the energy over both the top and bottom of the disk. This is the rigid mode assumption allowing the DC and AC response to be connected by simple harmonic motion.

$$dU_{VdW} = \int \frac{1}{2} \rho_{He}\, g\, \eta(r, \phi)^2 dA \tag{2.25}$$

where g is Van der Waals force per unit mass. We calculate the energy over the whole disk as

$$U_{VdW} = \rho_{He}\, g\, \eta^2\, \pi a^2\, \Psi_{rms}(r, \phi)^2 \tag{2.26}$$

where $\Psi_{rms} = \frac{1}{\pi a^2} \int \psi^2 dA$.

The equilibrium condition in a DC field is achieved by setting the derivative of the sum of electrostatic and van der Waals energies with respect to the displacement η equal to zero. The displacement obtained in this calculation is the hypothetical rigid mode displacement in the static field, η_{DC}

$$\eta_{DC} = \frac{1}{4} \frac{\epsilon_0 V_D^2 \left(1 - \epsilon_{He}^{-1}\right) D}{\rho_{He}\, g\, d^2\, \Psi_{rms}(r, \phi)^2} \tag{2.27}$$

The third sound speed as function of film thickness is

$$c_3^2 = \frac{\rho_s}{\rho_{He}} g h \tag{2.28}$$

which ρ_s is the superfluid component density. It is

$$\rho_s = \rho_{He} \left(1 - \frac{hs}{h}\right) \tag{2.29}$$

where h_s is known as the "solid layer" of liquid helium. It is dominated by a layer that is solid under high pressure due to the van der Waals force, but also includes a non-superfluid contribution from the surface healing length. It's experimentally determined thickness is 0.52 nm [15]. Equation 2.27, 2.28 and 2.29 yield

$$\eta_{DC} = \frac{1}{4} \frac{\epsilon_0\, V_D^2\, h\, \left(1 - \frac{h_s}{h}\right) \left(1 - \epsilon_{He}^{-1}\right) D}{\rho_{He}\, c_3^2\, d^2\, \Psi_{rms}(r, \phi)^2} \tag{2.30}$$

The AC drive force has half the DC amplitude at twice the drive frequency. It is derived from $cos(\omega_r t)^2 = \frac{1 + cos(2\omega_r t)}{2}$.

We calculate the displacement based on the assumption of simple harmonic oscillator motion of the rigid mode. Using the $exp(-i\omega t)$ convention, the AC response is then

$$\eta = \frac{\frac{1}{2}\eta_{DC}}{1 - \left(\frac{\omega}{\omega_0}\right)^2 - \frac{i}{Q}\frac{\omega}{\omega_0}} \tag{2.31}$$

Further discussion considers the amplitude on resonance, which is $\omega = \omega_0$, where ω_0 is the mode resonance frequency and Q is the quality factor.

$$\eta_{mn} = \frac{i}{2}\eta_{DC} Q \tag{2.32}$$

Hence, the thickness oscillation on resonance for the m, n^{th} mode is

$$\eta_{mn} = \frac{i}{8} Q \frac{\epsilon_0\, V_D^2\, h\, \left(1 - \frac{h_s}{h}\right)\left(1 - \epsilon_{He}^{-1}\right) D}{\rho_{He}\, c_3^2\, d^2\, \Psi_{rms}(r, \phi)^2} \tag{2.33}$$

Differentiation of equation 2.12a respect to C_p give us

$$df_{mn} = -\frac{1}{2} L \left(L(C_p + C_s)\right)^{-3/2} dC_p \tag{2.34}$$

The ratio between equation 2.34 and 2.12a is

$$\frac{df_{mn}}{f_{TDO}} = -\frac{1}{2}\frac{dC_p}{(C_p + C_s)} \tag{2.35}$$

where f_{TDO} is equal to f_{empty}. Using 4.4, we have the changes of the TDO frequency due to changes of capacitance. It is

$$\frac{df_{mn}}{f_{TDO}} = -\frac{1}{2}\frac{dC_P}{C_{tot}} \tag{2.36}$$

Then, we can insert the capacitance changes equation 2.21b into equation 2.36 to calculate mode sensitivity of the TDO. It is

$$\frac{df_{mn}}{\eta_{mn}} = -\frac{1}{2}\frac{f_{TDO}}{d^2}\frac{\pi a^2 \epsilon_0 \left(1 - \epsilon_{He}^{-1}\right) P}{C_{tot}} \tag{2.37}$$

Using equation 2.13 and 2.16, we can rewrite equation 2.37 in terms of measuring quantities

$$\frac{df_{mn}}{\eta_{mn}} = -\frac{1}{2}\frac{f_{TDO}}{d}\frac{\pi a^2 \left(1 - \epsilon_{He}^{-1}\right) cprP}{A_p} \tag{2.38}$$

The theoretical frequency modulation of tunnel diode frequency due to thickness oscillation is

$$f_{mn} = \eta_{mn}\frac{df_{mn}}{\eta_{mn}} \tag{2.39}$$

The complete expression of the above equation is

$$f_{mn} = -\frac{i}{16} Q f_{TDO}\frac{h}{d}\left(1 - \frac{1}{\epsilon_{He}}\right)^2 cpr\frac{\pi a^2}{A_p}\frac{DP}{\Psi_{rms}^2}\left(1 - \frac{h_s}{h}\right)\frac{\epsilon V_d^2}{d^2 \rho c_3^2} \tag{2.40}$$

2.1.5 Experimental sensitivity

The actual comparison to experimentally measured voltage amplitudes requires a calibration of the complete Frequency Modulation (FM) detection system. This is the phase-locked loop calibration (PLLCAL). It is the response of the voltage measuring device to a known frequency modulation imposed in the detector electronics. The PLLCAL is measured in Volt/Hz.

We drive the third sound mode wiith V_d drive voltage swept over a range of drive frequencies. The third sound signal is detected by the detection system and fit to a Lorentzian 2.31 to extract the information of third sound frequency, quality factor, amplitude and phase. We calculated the experimental frequency modulation (f_{mn}^{exp}) using the measured third sound voltage amplitude and the PLLCAL.

The theoretical value of thickness oscillation needs the information of the measured third sound frequency and quality factor. We used the third sound frequency to calculate the third sound speed. It is

$$c_3 = \frac{\omega_0)a}{x_{mn}} = \frac{4\pi f_{res} a}{x_{mn}} \tag{2.41}$$

which f_{res} is the resonance frequency. The 4π frequency doubling associated with the AC response of pickup capacitance. Then, we used the third sound speed to calculate the film thickness using equation 2.28. Finally, we calculate the theoretical frequency modulation using equation 2.40.

The component f_{mn}^{exp} Sensitivity ratio has several experimental corrections due to the lock-in instrument DSP lock-in phase and definitions used in the fitting between amplitude on resonance and relative to Simple Harmonic Oscillator. After these adjusments, the sensitivity ratio is

$$SR = \frac{i f_{mn}^{exp}}{i f_{mn}^{c}} \tag{2.42}$$

Factor of i in the numerator is a phase difference between the 1f and 2f responses at DSP lock-in. Factor of i in the denominator is phase different between amplitude on resonance and relative to Simple Harmonic Oscillator. The conjugate of f_{mod} responsible for transformation from $exp(-i\omega T)$ for f_{mod} derivation and $exp(i\omega t)$ for experimental result fitting program.

2.2 Sensitivity ratio of mechanical resonance

We also checked the disk mechanical resonance signal to get more information of electronic problems that could make the sensitivity ratio of third sound signal deviated significantly from 1. The mechanical distortion of sapphire disk is also driven by the electrostatics field of the drive capacitor. In a similar way, we also find the vibrational mode of the disk. The disk is supported by a central on the base. The mode and its frequency for this geometry can be calculated based on the vibration of a clamped circular plate from a paper by Leissa [14].

2.2.1 Theory of plate vibration

The transverse wave of a plate distortion η is

$$\nabla^4\eta - k^4\eta = 0 \tag{2.43}$$

k is a parameter related to the vibration frequency by

$$\omega^2 = \frac{Yh^2k^4}{12\rho(1-\nu^2)} \tag{2.44}$$

which Y is modulus Young, h is plate thickness, ρ is density of the plate, and ν is Poisson ratio.

The general solution for the differential equation 2.43 is

$$\eta = (AJ_m(kr) + BI_m(kr) + CY_m(kr) + DK_m(kr))cos(m\phi)e^{-i\omega t} \tag{2.45}$$

where J is Bessel function of the first kind, Y is Bessel function of the second kind, I is modified Bessel function of the first kind, and K is modified Bessel function of the second kind.

For our derivation, we use the specific solution for the case where the annular plate is clamped at the inner radius and free at the outer radius. This system is similar to the base supported plate as used in our experiment. The bending moment of the plate is

$$M_r = -D\left[\frac{\partial^2\eta}{\partial r^2} + \nu\left(\frac{1}{r}\frac{\partial\eta}{\partial r} + \frac{1}{r^2}\frac{\partial^2\eta}{\partial\theta^2}\right)\right] = 0 \tag{2.46}$$

and the Kelvin-Kirchhoff edge reaction is

$$V_r = -D\frac{\partial}{\partial r}(\nabla^2\eta) + \frac{1}{r}\frac{\partial}{\partial\theta}\left(-D(1-\nu)\frac{\partial}{\partial r}\left(\frac{1}{r}\frac{\partial\eta}{\partial\theta}\right)\right) \tag{2.47}$$

which D is flexural rigidity, defined as

$$D = \frac{\rho\omega^2}{k^4h} \tag{2.48}$$

Hence, the bending moment at outer edge is

$$M_r = U = \frac{\partial^2}{\partial x^2}\eta + \nu\left(\frac{1}{x}\frac{\partial}{\partial x}\eta - \frac{m^2}{x}\eta\right) = 0 \tag{2.49}$$

and

$$V_r = \frac{\partial}{\partial x}(\nabla^2 \eta) - \frac{m^2(1-\nu)}{x}\frac{\partial}{\partial x}(\frac{\eta}{x}) = 0 \tag{2.50}$$

The inner clamped condition :

$$\eta = 0, \frac{\partial}{\partial x}\eta = 0 \tag{2.51}$$

where $x = kr$. We insert 2.45 to the boundary conditions of free outer edge and clamped inside to construct a matrix representing the boundary conditions. It is

$$M(x) = \begin{pmatrix} UJn(m,x) & UIn(m,x) & UYn(m,x) & UKn(m,x) \\ VJn(m,x) & VIn(m,x) & VYn(m,x) & VKn(m,x) \\ Jn(m,\epsilon x) & In(m,\epsilon x) & Yn(m,\epsilon x) & Kn(m,\epsilon x) \\ \frac{\partial}{\partial x}Jn(m,\epsilon x) & \frac{\partial}{\partial x}In(m,\epsilon x) & \frac{\partial}{\partial x}Yn(m,\epsilon x) & \frac{\partial}{\partial x}Kn(m,\epsilon x) \end{pmatrix}$$

where $\epsilon = b/a$ which is the ratio of inner and outer diameter. We can find the frequencies and coefficients of each term by solving these equations :

$$\left| M(x) \right| = 0 \tag{2.52a}$$

$$M(x)\begin{pmatrix} A \\ B \\ C \\ D \end{pmatrix} = 0 \tag{2.52b}$$

There are two modes that most likely can be measured. They are (0,0) and (2,0) mode. But, when we did the measurement, the (0,0) mode is very difficult to detect due to its coupling to other parts of apparatus.

2.2.2 Disk geometry

Most of the response follows that of the third sound mode. In the previous section, we already explained the disk geometry. There is slight different parameter in the mechanical resonance analysis. The radius of the disk (a) excludes half of the disk thickness correction since the analysis is for transverse distortions of the disk, not the film on it's surface.

2.2.3 Drive and pick-up Integrals

Based on the wave mode calculation, we can write the geometrical overlaps of the wave mode with the electrodes.

$$D, P = \frac{1}{\pi a^2} \int \left(A J_m\left(x_m r\right) + B I_m\left(x_m r\right) + C Y_m\left(x_m r\right) + D K_m\left(x_m r\right) \right) cos(m\Phi) dA \tag{2.53}$$

For (2,0) mode, equation 2.52 gives

$$\Phi(2, x_m r) = \frac{1}{\sqrt{0.0723}} \left((-0.979) J_2\left(x_m r\right) + (-0.185) I_2\left(x_m r\right) + (-0.069) Y_2\left(x_m r\right) + (-0.046) K_2\left(x_m r\right) \right) \tag{2.54}$$

Now, we calculate P(2,0) mode which is wave mode overlapping with pickup electrode.

$$rc = \sqrt{A_p^2 + \left(\frac{B_p}{2}\right)^2}$$

$$p1 = \int_{A_p}^{rc} \Phi(2, x_m r) acos\left(\frac{A_p}{r}\right) r dr \tag{2.55}$$

$$p2 = \int_{rc}^{R} \Phi(2, x_m r) \left(\frac{\pi}{4} - asin\left(\frac{A_p - \frac{B_p}{2}}{\sqrt{2} r} \right) \right) r dr \tag{2.56}$$

hence, P(2,0) is $\frac{4}{\pi}(p1 + p2)$ with x_m is 2.465. D(2,0) is $\frac{2}{\pi}(p1 + p2)$

2.2.4 Mode Details

The detail of the mode is (2,0) mechanical mode. here, the changing of capacitance due to transverse oscillation of the silver-coated sapphire disk. Hence, we calculate the displacement by equating the elastic energy and the electrostatic energy. First, we started from the mode shape

$$\eta(r, \phi) = \eta \ \Psi(r, \phi) \tag{2.57}$$

The changing of capacitance because of changing the gap due to disk oscillation can be calcutaed using equation 2.18 with $\epsilon_{He} = \infty$.

$$dC = \frac{\epsilon_0 \, dA}{d - \eta(r, \phi)} - \frac{\epsilon_0 \, dA}{d} \tag{2.58}$$

The equation of drive and pickup capacitor and electrostatic energy for the disk are similar for third sound. The only different is the restoring force. It is elastic energy of the disk. The elastic energy is the same as kinetic energy of the disk for simple harmonic oscillator.

$$\Delta U_{elast} = \int \frac{1}{2} |v_p|^2 \, dM \tag{2.59}$$

which $v_p = i\omega\eta$. v_p is peak velocity of the disk displacement. Hence, the elastic energy is

$$\Delta U_{elast} = \frac{1}{2}\omega^2\eta^2 \int \rho h \, dA \tag{2.60}$$

$$\Delta U_{elast} = \frac{1}{2}\, \rho\, \pi\, a^2\, h\, (\omega\eta)^2 \tag{2.61}$$

which is $\omega = 2\pi(2f)$. The equilibirum mode displacement in the static field (DC) is
$\frac{d}{d\eta}\,(\Delta U_{elect} + \Delta U_{elast}) = 0$ and
$\rho\pi a^2 h\omega^2\eta = \frac{\pi a^2 \epsilon_0\, V_d^2}{2d^2} D$
Hence,

$$\eta_{DC} = \frac{1}{2}\frac{\epsilon_0\, V_d^2\, D}{\rho\, h\, d^2\, \omega^2} \tag{2.62}$$

As before, the gap size oscillation on resonance is

$$\eta_{20} = \frac{i}{4}\, Q\, \frac{\epsilon_0\, V_d^2\, D}{\rho\, h\, d^2\, \omega^2} \tag{2.63}$$

This is called the mode sensitivity of the LC oscillator for disk mechanical resonance is

$$\frac{\Delta f_{tdo}}{\eta} = -\frac{1}{2}\frac{f_{tdo}}{d}\frac{C_p}{C_{tot}}\frac{\pi a^2}{A_p} P \tag{2.64}$$

Finally, the frequency modulation of TDO for mechanical resonance is

$$f_{20} = -\frac{i}{8}\, Q \frac{f_{TDO}}{d}\, cpr\, \frac{\pi a^2}{A_p}\, \frac{DP}{\omega^2}\, \frac{\epsilon_0 V_d^2 D}{\rho h d^2} \tag{2.65}$$

From this equation, a similar sensitivity ratio can be measured for comparison to the third sound case. These results are discussed in the chapter 5.

Chapter 3

Capacitor Gap Integrity

The capacitor gap has a major role in the detection system. It needs to be clean and not have any dirt that can bridge the electrode plate and the disk. The disk itself also needed to be in a good condition. We expected that there is smooth surface of the silver coated sapphire (Al_2O_3) disk. Otherwise, it would amplify the dissipation of the third sound signal. We also improve the assembling process of the plate. We invented the way we can place the plate support in the center of the plate.

3.1 The disk and the electrode plate

The disk plate is supported by the puck. We attached the disk puck right in the center of disk bottom surface. It needed to be placed with high precision since the off-center position would change the quality of the third sound mode signal. The attaching process was performed in the Leitz Jig Borer machine as shown in figure 3.1(a). We used the X and Y scale on that machine to center the puck. We also focused on the disk surface smoothness. Since the superfluid helium film coated the top and bottom surface of the disk, we needed to have a smooth surface on the disk edge. We polished the disk edge using a lathe machine at about 650 Rotations Per Minute (RPM). We used the diamond slurry to grind the rough surface of the disk edge.

The sapphire disk needed to be clean in order to let the silver coated stick well on it. In the polishing process, there were a lot of sapphire chips that was ground by the diamond slurry. Hence, we needed to clean the disk with methanol and wiped it with kimwipe. The disk was dried with

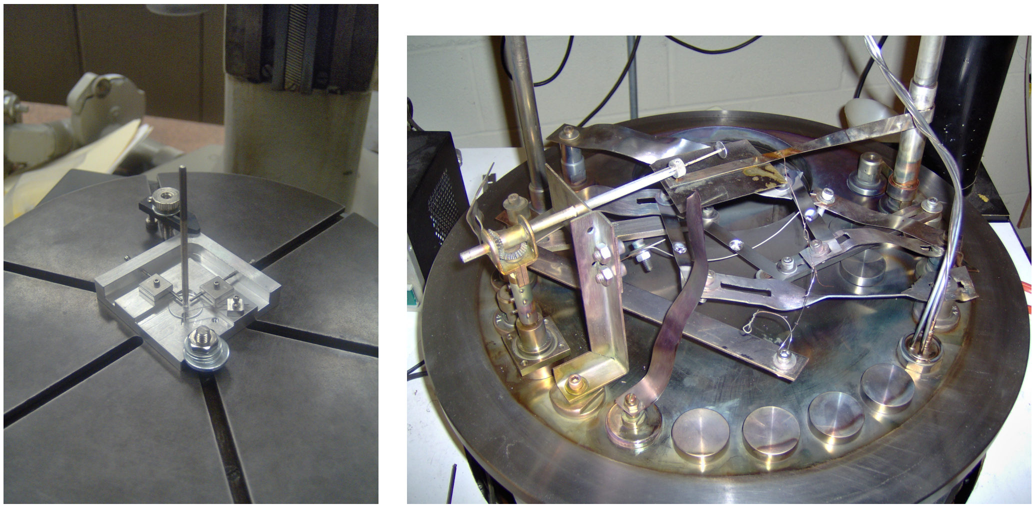
(a) (b)

Figure 3.1: The centering process and the coating chamber.

the air blower.

The coating process was performed using a Veeco evaporator to create the thin film coating of the sapphire disk as shown in figure 3.1(b). To enhance the stickness of the thin film, the Titanium filament need to be added to the coating process. We tried the coating process without titanium addition to examine the stickiness. The silver coating was easily taken off by rubbing it with a finger. The thickness of the silver thin film was monitored by the Quartz crystal resonance frequency. The frequency changes (Δf) correspond to thickness changes (Δd in $\mathring{A}$). It is

$$\Delta f = K_M \Delta d \left(1 - \frac{\Delta f_0}{f_q}\right)^2 \left(\frac{h_T}{h_M}\right)^2 \tag{3.1}$$

K_M is the rate of frequency changes per changes of film thickness. It is 10.3 Hz/m for silver coating on sapphire substrate. h_T and h_M are the height of the disk and the quartz crystal monitor from the silver boat. In our evaporator, the h_M is twice the h_T.Δf_0 and f_q are crystal health reading and uncoated quartz crystal frequency (6 MHz). Crystal health reading is initial crustal frequency reading before the coating process. For 1000 $\mathring{A}$ film thickness at 632 Hz crystal health reading, the frequency change was about 2574 Hz. The rate of deposition corresponds to the rate of the frequency change. We adjust the rate of frequency changes to be 20 - 24 Hz per second to get uniform film thickness.

The electrode plate also needed to have a smooth surface. We also wanted the plate as flat

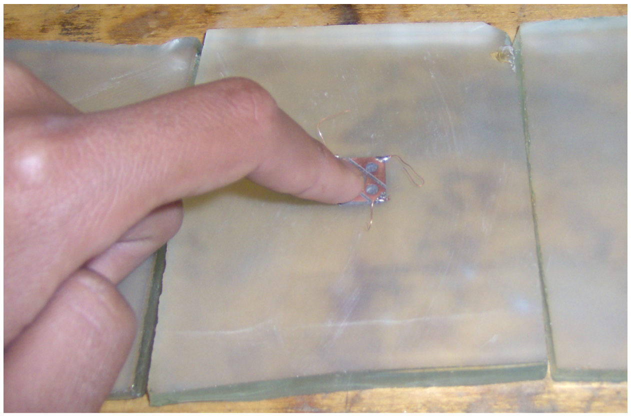

Figure 3.2: The SiC coated glass plates to make the electrode plate smooth and flat.

as possible since we would expect that we have uniform capacitor gap size. Before we did the smoothing process, we needed to solder the wire to the four corners of the electrode plate. It only needed a small amount of solder but a well wetted bead. If necessary, we could sand the solder bump in such a way that no solder protruded above the plane of the electrode plate. Then, we prepared for the smoothing process. We used 3 glass plates that was coated by Silicon Carbide (SiC). To coat the plate with the SiC, we wetted the glass plates with SiC slurry and pressed and rubbed 2 plates together at a time. After we had very thin layer of the SiC coating the glass plate, we were ready to sand the electrode by gently pressing and rubbing the electrode plate with a finger to the glass plates. We repeated the process until we had a smooth and flat surface on the electrode plate. Figure 3.2 shows the smoothing process of the electrode plate. The final step was assembling the disk with the puck and the electrode plates which were supported by the post on the resonator base.

3.2 Cleaning the capacitor gap

We assembled the resonator in a clean room. The clean room that we used is different from the clean room used for semiconductor fabrication. The clean room has an air blower that blow any dirt down away to the floor. We made measurements of the dirt collection in the clean room to know the quality of the clean room. Since the capacitor gap size is in the range of 20-30 μm, we are interested in dirt that has a size of 10 - 20 μm. We made 70 squares with the area of 0.09 cm^2 on a glass microscope slide. We counted the number of the dirt on each square under the microscope. We let the glass microscope slide stay in the clean room for 9374 minutes. We got the reading of number of the dirt difference before and after we took the measurement. The result of the collection rate was 0.018 ± 0.043 particles per cm^2 per hour. This collection rate was below the threshold of the dirty limit which is 0.1 particle per 1 cm^2 area per hour. A typical time to assembly the resonator is 2.5 hours.

We swept 12 μm thick kapton sheet through the gap to make sure that there was no dirt inside the capacitor gap. Hence, any dirt that was trapped inside the gap would be swept away by the kapton sheet. It also gave us an approximation of the capacitor gap size. The capacitor gap size was not less than the size of the kapton sheet thickness.

3.3 The quality of capacitor gap

We tested the cleanliness of the capacitor gap by filling the cell with the liquid Nitrogen. By measuring the dimension of the cell and all the components of the resonator, we can calculate the volume at the bottom of the electrode plate (V_{bp}). The volume of the liquid that is transferred to the cell is less than V_{bp}. In other words, the liquid level is below the height of the bottom of the electrode plate. Any dirt that is inside the capacitor gap will pull the liquid into the capacitor gap. Hence, the capacitor gap will be filled with liquid even while the liquid level is well below the height of the electrode plate.

We do not have volume gauges to measure the volume of the liquid in the cell. Hence, we are unable to do measurements in such away that we fill the cell below the V_{bp}. However, we can use another level, which is the position of filling tube. The height of the filling tube is well below the V_{bp}. We can calculate the height of the filling tube based on the cell dimension. We also can get the height by monitoring pressure changes as we pump the cell.

First, the cell was being filled with liquid Nitrogen at 75 Torr above atmospheric pressure (760 Torr) for about 6 hours. Then, the cell was pumped. We took measurement of pressure as a function of time. The starting pressure was about 7.2 Torr. After we pumped for about 20 minutes, the pressure dropped to 3.8 Torr. The pressure stayed almost constant for about 10400 seconds. Those 2 pressure values gave us information the position of the filling tube. The 3.8 Torr pressure corresponds to the moment when the liquid Nitrogen level at the height of the filling tube.

The way we calculated the height of the filling tube was to start from calculating the volume

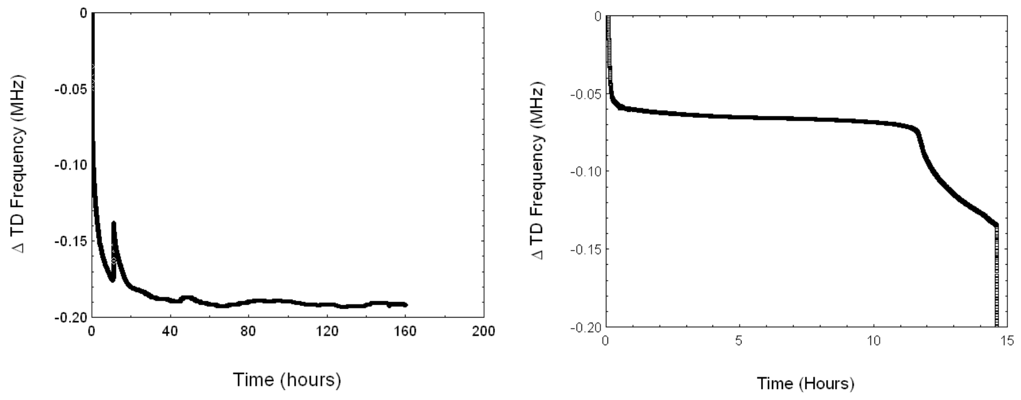

(a) (b)

Figure 3.3: The graph of the TD frequency changes as a function of time for clean and dirty capacitor gap

of liquid Nitrogen at a particular pump rate.

$$V_0 = \dot{V_0}\left(\frac{3.8\,Torr}{P_{ref}}\right)^2\ 10400s \tag{3.2a}$$

$$\Delta V_f = \dot{V_0}\left(\frac{7.2\,Torr}{P_{ref}}\right)^2\ 1080s \tag{3.2b}$$

which V_0, ΔV_f, $\dot{V_0}$ and P_{ref} are liquid Nitrogen volume at the height of filling tube, the volume of the liquid Nitrogen above the height of filling tube, the pump rate and reference pressure, respectively. Hence, the ratio of time to fill the cell with liquid Nitrogen at particular filling rate between V_0 and $V_0 + \Delta V_f$ is 0.72. Based on this ratio, we had to fill the cell up to V_0 for 4.32 hours at 75 Torr above atmospheric pressure. That was equivalent to 1.439 cc of liquid Nitrogen. Once the liquid level reach the height of the filling tube, we stopped filling.

During the filling and pumping process, the TDO frequency changes as the dielectric of capacitor changes from vacuum to liquid Nitrogen. We compared the behavior of the TDO frequency as a function of time for the clean and dirty capacitor gap. Figure 3.3(a) shows that we stop filling after 4.32 hours and waited for about 6 days. The TD frequency remained constant for a very long time. There was insignificant jump that indicated filled capacitor gap. If the capacitor gap was filled by liquid Nitrogen, there would be a TDO frequency jump that was about 3 MHz for the first jump and another 6 MHz for the second jump. Hence, we can conclude that the capacitor gap was clean since there was no indication of a frequency jump when the cell was filled below the bottom of electrode plate. Figure 3.3(b) shows the dirty capacitor gap case. In that case, the cell

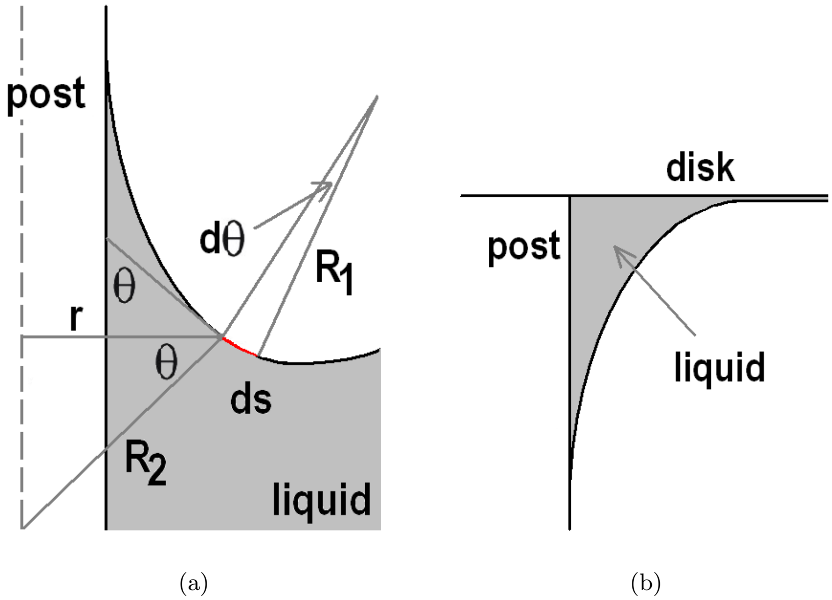

(a) (b)

Figure 3.4: (a) Meniscus profile of liquid wetting the space between electrode and disk post. (b) Meniscus profile of liquid at the bottom surface of the disk.

was filled at 20 Torr above atmospheric pressure for about 14.733 hours. The total liquid Nitrogen was 1.311 cc which is below the bottom of electrode plate. We can see that the TDO frequency jumped significantly. That indicates that there was dirt inside the capacitor gap that attract the liquid Nitrogen.

Figure 3.3 also tell us the dynamic of the filling process. In the beginning, the frequency dropped rapidly. This is the saturation process. Once the Nitrogen is saturated, it fills the reservoir underneath the cell. The volume of this reservoir is about 1.36 cc.

3.4 Capillary

We need to investigate the dynamics of liquid Helium and liquid Nitrogen inside the cell. The liquid will coats all surfaces in the cell including the surfaces of the disk and electrode. We are focusing our investigation on the case when the liquid level is approaching the gap between the electrode and the disk. At that position, the liquids is not only rising outside of the electrode hole but also rising in the region between the electrode and the disk post. The situation is interesting because the liquid level inside could be higher than liquid level outside of the electrode hole.

The liquid has surface tension along the film surfaces. The pressure different accross an interface between liquid and gaseous phase can be expressed by Young-Laplace equation. It is

$$\Delta P = \gamma \left(\frac{1}{R_1} + \frac{1}{R_2} \right) \tag{3.3}$$

which γ is the surface tension, and R_1 and R_2 are the principal radii of curvature of the liquid surface. For surface rising in gravity, the pressure difference is essentially the pressure difference of gas pressure and hydrostatic pressure of liquid at the depth z. The curvature radius of the liquid can be calculated by a small curved sector. This curved sector has small angle $d\theta$, radius R_1 and arc ds along the surface of the liquid. R_2 is the hypotenuse of a triangle with the adjacent side r and angle θ. r is measured from the center of the disk post. The center of curvature is in the liquid phase, hence the R_1 must have negative sign. The liquid is on the positive side of θ so we have negative minus sign on Young-Laplace equation. We can rewrite equation 3.3 as

$$P - \rho g z = -\gamma \left(\frac{cos(\theta)}{r} - \frac{d\theta}{ds} \right) \tag{3.4}$$

where P is the pressure of the gas and z is the vertical distance of element ds measured from liquid level of liquid outside of the electrode. Figure 3.4(a) shows the geometry of liquid meniscus. The Young-Laplace equation tells us the equilibrium shape of curved interface between liquid and gaseous phase in gravitational field.

We re-scale the Young-Laplace equation in the units of capillary length. Hence, we have

$$\lambda_c = \sqrt{\frac{2\gamma}{\rho g}} \tag{3.5}$$

Hence, we can write equation 3.4 in term of λ_c as

$$\frac{P\lambda_c}{\gamma} - 2\frac{z}{\lambda_c} = \lambda_c \left(\frac{d\theta}{ds} - \frac{cos(\theta)}{r} \right) \tag{3.6}$$

We can calculate the height of liquid level inside of the columns of electrode and get the picture what is the shape of the liquid surface. We start calculation at the contact point between liquid and post wall ($z = 0$) and stop at the contact point between liquid and electrode post wall. The pressure value is obtained from the meniscus profile calculation using equation 3.6. We use it to calculate the vertical distance between the flat surface and $z = 0$ point using hydrostatic pressure equation. We also calculate the liquid meniscus at the bottom surface of the disk using similar calculation procedure. The meniscus liquid at the bottom surface of the disk is shown in figure

Properties	Helium	Nitrogen
$\gamma\ (N/m)$	0.00028835	0.008956
$\rho\ \left(kg/m^3\right)$	146.24	808
$\lambda_c\ (m)$	0.000634	0.001504

Table 3.1: Table of the capillary parameter of liquid Helium-4 and Nitrogen.

3.4(b). There are 2 types of liquid that we use in the calculation. They are liquid Helium at 2.176 K and liquid Nitrogen at 77 K. Table 3.1 shows the properties of both liquids.

The gap will be filled with liquid in three different situations as shown in figure 3.5. They are

1. Electrode wick. This is an instability situation of liquid. It is happen when the liquid meniscus from the bottom surface of the disk meet the liquid meniscus at the space between electrode and the disk post.

2. Extend gap. The capacitor gap also can be filled with liquid when the horizontal end of liquid meniscus at the bottom surface of the disk (r_h) reach the space inside the gap. This is happened when r_h equal to electrode center hole radius. It is $1.875.10^{-3}m$.

3. Disk fill. This is also instability situation of liquid. It is happen when the vertical end of liquid meniscus from the bottom surface of the disk (z_h) meet the liquid level below the electrode (z_l). The z_h and z_l are equal since the geometry of boundary is similar which is flat surface and circular surface. It means that the disk fill situation is possible when the liquid level is equal to twice z_h.

We calculate the liquid level when the three situations occur for liquid Nitrogen and liquid Helium-4. That is the critical liquid level (h_c). We measure the critical liquid level in term of vertical distance between the liquid flat surface and the bottom surface of the disk. Table **??** shows the critical liquid level at the three situations for both liquids. The thickness of electrode and the capacitor gap size are $1.5.10^{-3}m$ and $30.10^{-6}m$, respectively. Hence, the combined thickness of electrode and capacitor gap is $1.53.10^{-3}$. This is also the vertical distance between the bottom surface of the disk and the bottom surface of the electrode (h_{el}). The wicking situation only applied if the liquid level lower than that distance (measured from the bottom surface of the disk).

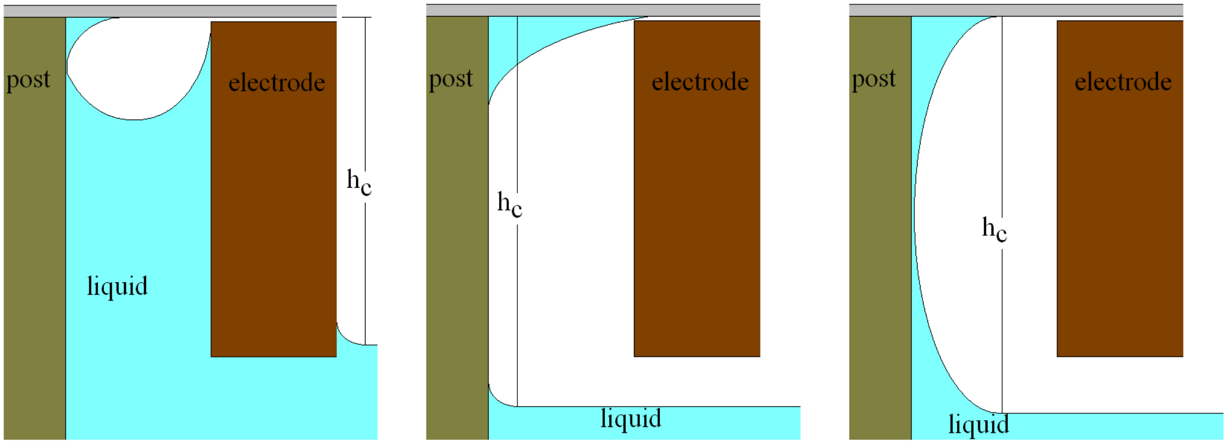

(a) Electrode wick (b) Extend gap (c) Disk fill

Figure 3.5: Three different situations of capacitor gap filled by liquid.

The critical liquid level for liquid Helium and Nitrogen are $1.224.10^{-3}m$ and $4.023.10^{-3}m$, respectively. The critical liquid level of Helium is lower than h_{el}. It means that the liquid Helium is already inside the space between the electrode and the disk post. The critical liquid level of Nitrogen is bigger than h_{el}. It means, the gap will be filled wih liquid Nitrogen when the liquid level at $3.663.10^{-3}m$ below the bottom surface of the electrode. This electrode wick situation for liquid Nitrogen is less likely happen since the liquid is not in the space between electrode and disk post yet.

When the liquid level of Helium reach the bottom surface of the disk, r_h is $1.405.10^{-3}m$. It is smaller than electrode center hole radius. The r_h will go even smaller when the liquid level below the bottom surface of the disk since the hydrostatics pressure is increasing. Hence, the extend gap and disk fill situation are less likely happen in liquid Helium. For the liquid Nitrogen case, the extend gap and disk fill situation are the possible situation for filling the capacitor gap. The liquid meniscus at the bottom surface of the disk reach the space inside the gap when the liquid level is $2.378.10^{-3}m$. The vertical end of the liquid meniscus is $0.982.10^{-3}m$. It is less than half of the liquid level. Hence, the extend gap situation is occured sooner than disk fill situation.

The position of liquid level corresponds to the liquid volume that has been transferred into the cell. We have the record of filling process than contain information of the filling rate and filling time. Hence, we can verify the liquid level calculation with the liquid volume that has been transferred.

3.5 Gap size expansion

The capacitor gap is changing as cell temperature changes. Different parts of the resonator will expand their length in many differrent ways depending on their thermal properties. The gap size expansion is determined by the expansion of the disk post and the electrode plate. The sapphire disk with sapphire disk puck is supported by a Berrylium Copper (BeCu) post. The disk and Copper (Cu) electrode plate create capacitor. We calculated the thermal expansion of BeCu and Cu from room temperature to liquid Helium and liquid Nitrogen temperature to know the capacitor changes as a function of temperature. We verify the calculation by calculating the TDO frequency changes as a function of temperature.

3.5.1 The thermal expansion

We used 3 equations of thermal expansion since the cell material are consist of sapphire, Copper, and Berrylium Copper. The linear thermal expansion of BeCu as a function of temperature t can be expressed as

$$\alpha_{BeCu}(t) = \begin{cases} -316.68.10^{-5} & \text{if } t < 24K, \\ \left(-3.115.10^{2} - 0.44498\,t + 1.0133.10^{-2}\,t^{2} - 2.4718.10^{-5}\,t^{3} + 2.6277.10^{-8}\,t^{4}\right).10^{-5} & \text{otherwise.} \end{cases} \tag{3.7}$$

Hence, the final length of BeCu as a function of temperature is

$$L_{BeCu}(t) = Lb_{293} + \alpha_{BeCu}(t)\, Lb_{293} \tag{3.8}$$

where Lb_{RT} is the length of the disk post at room temperature (293 K).

The linear thermal expansion of sapphire as a function of temperature t can be expressed as

$$\alpha_{s}(t) = \begin{cases} \left(-78.85 - 2.2346.10^{-2}\,t + 1.0185.10^{-4}\,t^{2} + 5.5594.10^{-6}\,t^{3} - 8.5422.10^{-9}\,t^{4}\right).10^{-5} & \text{if } t > 15K, \\ (5.3 \pm 1.2)\,.10^{-13} t^{2.9\pm 0.15} & \text{otherwise.} \end{cases} \tag{3.9}$$

Hence, the final length of sapphire disk as a function of temperature is

$$L_{sapphire}(t) = Ls_{293} + \alpha_{s}(t)\, L_{293} \tag{3.10}$$

where Ls_{RT} is the thickness of the disk and the disk puck height at room temperature.

The linear thermal expansion of Copper as a function of temperature t can be expressed as

$$Log\left(\alpha_{Cu}(t)\right) = \left(a + b\,Log(t) + c\,Log(t)^2 + d\,Log(t)^3 + e\,Log(t)^4 + f\,Log(t)^5 + g\,Log(t)^6 + h\,Log(t)^7\right).10^{-6} \tag{3.11}$$

where $a = -0.606339$, $b = 276.779$, $c = -546.197$, $d = 580.1$, $e = -355.82$, $f = 126.778$, $g = -24.4575$ and $h = 1.98124$. Hence, the final length of Cu electrode as a function temperature is

$$L_{Cu}(t) = Lc_{293} + \alpha_{Cu}(t)\,Lc_{293}\,\Delta t \tag{3.12}$$

where Lc_{293} is the length of the electrode room temperature. and Δt is the temperature different between room temperature and t.

The linear thermal expansion of Epoxy as a function of temperature t can be expressed as

$$\alpha_{Ep}(t) = \begin{cases} 700.10^{-5} & \text{if } t < 5K, \\ \left(-4.392.10^{2} + 1.525.10^{-2}\,t - 2.384.10^{-3}\,t^2 + 8.665.10^{-6}\,t^3 - 2.857.10^{-9}\,t^4\right).10^{-5} & \text{if } 77 \leq t \leq 5K. \end{cases} \tag{3.13}$$

Hence, the final length of Epoxy as a function of temperature is

$$L_{Ep}(t) = Le_{293} + \alpha_{Ep}(t)\,Le_{293} \tag{3.14}$$

where Le_{RT} is the length of Epoxy at room temperature.

3.5.2 The possible case of gap size changing

We calculated the capacitor gap changes (Δg) as we cooling temperature down from room temperature to 4 K. All three materials thicknesses will be slightly shrinked. The capacitor gap would expand ($\Delta g > 0$) if the upper plate (the sapphire disk) shifting down less than the lower plate (the electrode plate). The shifted upper plate is caused by thermal contraction of the disk post, the disk puck and the disk. The shifted lower plate is caused by thermal contraction of the electrode and the electrode post.

We calculated the thermal expansion the disk post, the disk puck, the electrode and the electrode post to get the Δg at liquid Helium and Nitrogen temperature. The disk is connected to the disk post by the disk puck. Part of the disk puck is inside of the hole at the upper end of the disk pot. We assumed that this section is either dominated by thermal expansion of disk puck or disk post. The electrode plate material is a mixture of copper and epoxy. We calculated Δg using assumption

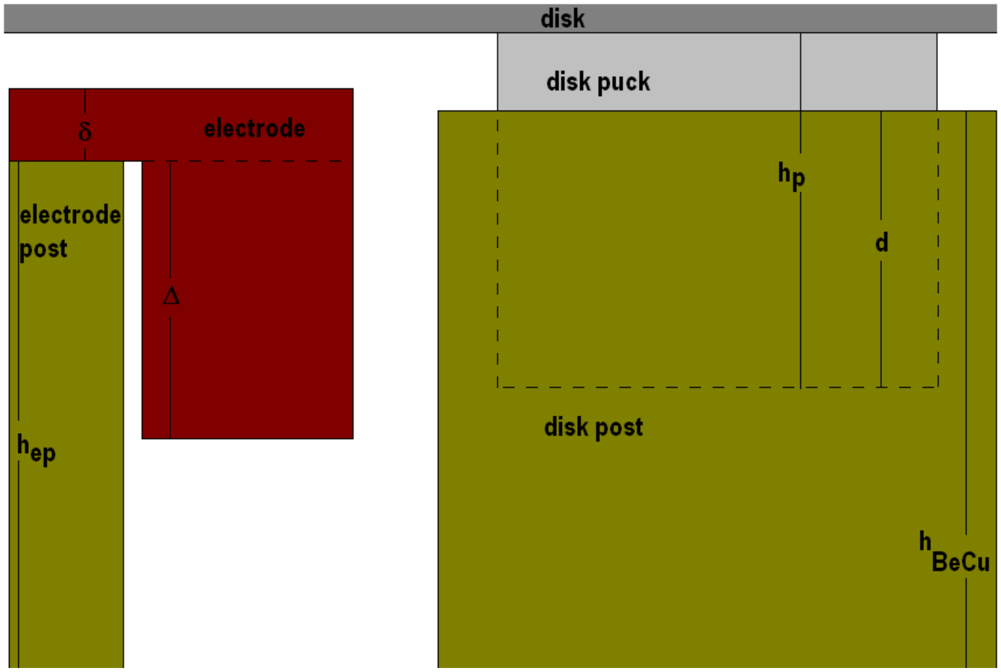

that the electrode material is dominated either by copper or epoxy. Hence, we have 4 possible situations of Δg. They are

1. The disk post is more dominant than the disk puck. Copper is dominant electrode material.
2. The disk post is less dominant than the disk puck. Copper is dominant electrode material.
3. The disk post is more dominant than the disk puck. Epoxy is dominant electrode material.
4. The disk post is less dominant than the disk puck. Epoxy is dominant electrode material.

For situation 1 and 3, we focused on the full height of the post (h_{BeCu}) substracted by the disk post hole depth (d). For situation 2 and 4, we focused on the height of the disk puck (h_p) substracted by the disk post hole depth (d).

We calculated thermal expansion for each part of resonator. The thermal expansion of electrode as a function of temperature ($d_{el}(t)$) is

$$d_{el}(t) = \begin{cases} \dfrac{\alpha_{Cu}(t) + \alpha_{Cu}(293)}{2} \; (h_{el} - \Delta)\, \Delta t & \text{for situation 1 and 2 (copper electrode),} \\ \alpha_{Ep}(t) \;\; (h_{el} - \Delta) & \text{for situation 3 and 4 (epoxy electrode).} \end{cases} \tag{3.15}$$

which h_{el} is the thickness of electrode $1.5.10^{-3}$ m. We took average value of two values of thermal expansion coefficient of copper at room temperature (293 K) and temperature t. The electrode

Temperature	Δg_1 (μm)	Δg_2 (μm)	Δg_3 (μm)	Δg_4 (μm)	Δg_f (μm)
4 K	0.594	-1.546	0.047	-2.093	3.558
77 K	1.668	-0.296	1.057	-0.908	3.216

Table 3.2: Table of capacitor gap changes for 4 possible situations and capacitor gap changes based on TDO frequency changes at liquid Helium and Nitrogen temperature.

post upper end is inside the electrode hole. The height of the electrode post (h_{ep}) is

$$h_{ep} = (h_p + h_{BeCu} - d) - (gap + \delta) \tag{3.16}$$

which gap and δ are the capacitor gap size and the thickness of electrode substracted by electrode hole depth. Hence, the thermal expansion of electrode post as a function of temperature $d_{ep}(t)$ is

$$d_{ep}(t) = \frac{\alpha_{Cu}(t) + \alpha_{Cu}(293)}{2}\, h_{ep}\, \Delta t \tag{3.17}$$

The thermal expansion of the disk puck height as a function of temperature ($d_{dk}(t)$) is

$$d_{dk}(t) = \begin{cases} \alpha_s(t)\, h_p & \text{for case 1 and 3,} \\ \alpha_s(t)\, \eta & \text{for case 2 and 4.} \end{cases} \tag{3.18}$$

which η is a section of the disk puck that is outside the disk post. The thermal expansion of the disk post height ($d_{dp}(t)$) is

$$d_{dp}(t) = \begin{cases} \alpha_{BeCu}(t)\ (h_{BeCu} - d) & \text{for case 1 and 3,} \\ \alpha_{BeCu}(t)\, h_{BeCu} & \text{for case 2 and 4.} \end{cases} \tag{3.19}$$

Hence, we can calculate the gap size changes with this expression

$$\Delta g(t) = (d_{dk}(t) + d_{dp}(t)) - (d_{el}(t) + d_{ep}(t)) \tag{3.20}$$

The TDO frequency at room temperature, 77 K and 4 K are 70.1 MHz, 74.8 MHz and 75.3 MHz respectively. Those frequency changing correspond to the gap expansion at 77 K and 4 K by 3.216 μm and 3.558 μm, respectively. Hence, the situation 1 is likely match with the experimental situation.

Chapter 4

Electronic Detection Analysis

The analysis of experimental resonances, both third sound and mechanical, are described in chapter 5. Sensitivity ratio differing primarily in phase by π and amplitude. Here, we present the calculation and experiments for various tests to investigate potential problems. The problems are related to the electrical connection and noise. The first problem is the TDO ciruicit especially for capacitor geometry is not what we think.We need to have good knowledge of electrical connection as we changes temperature, especially at the pickup capacitance. PLL detection is also defective since we observe the unintentional PLL coupling to external frequency. We also found that the noise level is higher than threshold to observe good resonance signal. Lastly, the poblem is related to the drive signal. It is not appropriately applied to the film. There could be lack of understanding about the frequency dependence of the drive voltage.

4.1 Poor electrical connection to pickup capacitor

The experimental signal and theoretical calculation is differ by factor of π. This could be caused by changes in the electrical connection at pickup capacitance at low temperature. Since the most critical electrcal connection is based on disk thermal expansion. We have explained in the chapter 3 that the disk is connected to the disk post by the disk puck. The disk puck is clamped to the upper end of the disk post. This spot is less likely contribute to the poor connection since at lower temperature the clamped force tend to be stronger because of length contraction. However, the glue joint between the disk and the disk puck could break due to length contraction and expansion.

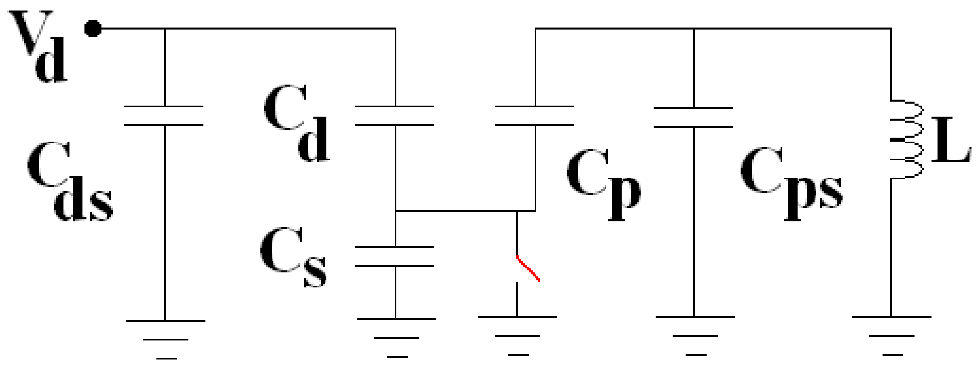

Figure 4.1: The scheme of the drive, pick-up, and stray capacitors. The switch represent the connection to the ground. The switch is open if there is open connection, otherwise it is close.

Another problem is an inability to monitor The TDO frequency when cooling cell temperature down. We can only read TDO frequency at room temperature and 77 K as described in the section 4.1.3. We need to get the measurement of TDO frequency and quality factor at temperature between room temperature and 77 K while the cryostat is in place. This measurement also will give us the information about the quality of electrical connection.

Figure 4.1 shows a likely situation consistent with the smaller sensitivity and phase shift. The switch connects or disconnects the disk to ground. If this switch was openning somewhere between room temperature and 77 K as we cool down, we will see a jump on the TDO frequency and its quality factor. We will also see low temperature capacitances consistent with the model. When switch is closed, the C_p dominates the calculation of TDO frequency. The film response has already presented in the chapter 2. The phase shift could be explained by switch open. At this case, the drive voltage split between drive and pickup capacitor. Since the area of the drive capacitor is bigger than pick-up capacitor, the drive capacitance is bigger than pick-up capacitance.

4.1.1 Capacitance consistency

The open electrical connection will change the electronic circuit. The small opening will act like a capacitor. We investigated the expected capacitance value of several capacitors in the case of open electrical connection. In the chapter 2, we have calculated the geometry of the drive and pick-up capacitor. The goal in this calculation is to calculate the pickup capacitance (C_p), the stray capacitances, and the gap size of the drive and pickup capacitor. The stray capacitors are

1. C_{ps} is the stray capacitance of pick-up capacitor.

   This capacitor is the capacitor between the pick-up electrode and the base and coil inductor.

2. C_{ds} is the stray capacitance of drive capacitor.

   This capacitor is the capacitor between the drive electrode and the base. Since the drive voltage is sent via coaxial cable from room temperature section, this capacitor also include the capacitance of the coaxial cable.

3. C_s is the stray capacitance in the disk-post connection.

   This capacitor is the capacitor that only present when switch open. It represent the gap between the disk puck and the disk post.

All the stray capacitance is unchanged as we fill and empty the resonator gap cell but the drive and pick-up capacitance change. We can observe the changing of the film thickness as we observe the drive and pick-up capacitance changing. The drive capacitance give negative response for the film oscillation while the pick-up capacitor responding in the different sign. C_d gives no effect to the C_p. In the chapter 2, we know that the response of drive and pick-up is in the opposite phase for (2,1) third sound mode.

The total capacitance is the combination circuit of several capacitors. We start the calculation for switch open situation from a series configuration of C_d and C_{ds}.

$$C_1 = \frac{C_{ds}C_d}{C_d + C_{ds}} \tag{4.1}$$

which C_1 is the capacitance of the series configuration. The parallel configuration between C_1 and C_s is

$$C_2 = \frac{C_{ds}C_d}{C_d + C_{ds}} + C_s = \frac{C_{ds}C_d + C_sC_d + C_sC_{ds}}{C_d + C_{ds}} \tag{4.2}$$

which C_2 is the capacitance of the parallel configuration. The C_2 is series with pick-up capacitor. Hence, the series capacitance C_3 is

$$C_3 = \frac{C_2C_p}{C_2 + C_p} \tag{4.3}$$

The total capacitance is the parallel configuration of C_3 and C_{ps}. It is

$$C_{tot} = C_3 + C_{ps} \tag{4.4}$$

This value is also the same as

$$C_{tot} = \frac{1}{(2\pi f_{tdo})^2 L} \tag{4.5}$$

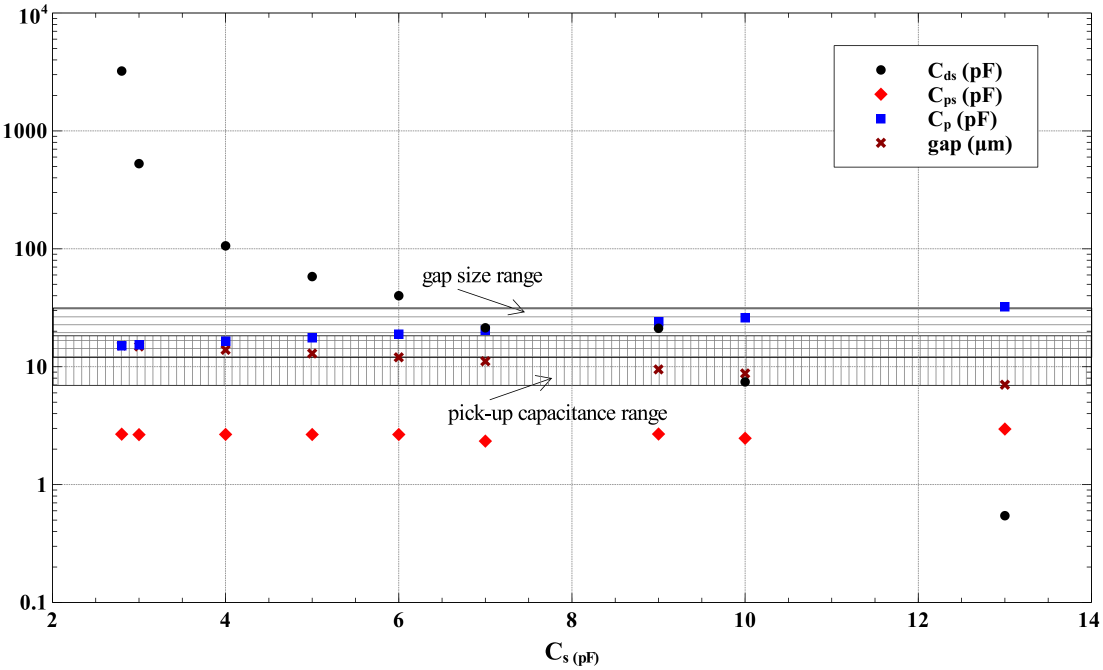

Figure 4.2: The graph of the pick-up, pick-up stray, drive stray capacitance and capacitor gap size as a function of the post-stray capacitor. The area with the horizontal line is the gap size range. The area with the vertical line is pick-up capacitance range. The intersection area is the the possible value of gap size and the pick-up capacitance.

which L is the inductance. When the cell is filled with fluid with dielectric ϵ, the drive and the pick-up capacitor change its capacitance by factor of ϵ. Hence, the total capacitance is

$$C_{totf} = \frac{1}{\left(2\pi\left(f_{tdo} - \Delta f\right)\right)^2 L} \tag{4.6}$$

which C_{totf} is the fluid filled total capacitance.

Using equation 4.4, scaling C_{tot}, equation 4.5 and 4.6, we calculated C_{ps}. It is

$$C_{ps} = \frac{1}{2}\left(C_{tot} + C_{totf} - \frac{\left(\left(C_{ds}+C_s\right)C_p\frac{A_d}{A_p} + C_sC_{ds}\right)C_p}{\left(C_{ds}+C_s\right)C_p\frac{A_d}{A_p} + \left(C_s+C_p\right)C_{ds}} - \frac{\left(\left(C_{ds}+C_s\right)\epsilon C_p\frac{A_d}{A_p} + C_sC_{ds}\right)\epsilon C_p}{\left(C_{ds}+C_s\right)\epsilon C_p\frac{A_d}{A_p} + \left(C_s+\epsilon C_p\right)C_{ds}}\right) \tag{4.7}$$

since we can replace C_d with $C_p\frac{A_d}{A_p}$, which A_d and A_p are the drive and pick-up capacitor area, respectively. We calculated the pick-up capacitance by finding the root of the equation below

$$\frac{1}{2}\left(C_{totf} - C_{tot} - \frac{\left(\left(C_{ds}+C_s\right)\epsilon C_p\frac{A_d}{A_p} + C_sC_{ds}\right)\epsilon C_p}{\left(C_{ds}+C_s\right)\epsilon C_p\frac{A_d}{A_p} + \left(C_s+\epsilon C_p\right)C_{ds}} + \frac{\left(\left(C_{ds}+C_s\right)C_p\frac{A_d}{A_p} + C_sC_{ds}\right)C_p}{\left(C_{ds}+C_s\right)C_p\frac{A_d}{A_p} + \left(C_s+C_p\right)C_{ds}}\right) = 0 \tag{4.8}$$

Hence, we can calculate the pick-up capacitance and the pick-up stray capacitance using input parameters of the post stray capacitance, the drive stray capacitance, the drive and pick-up capacitor area, the empty and filled TDO frequency. The input parameters and the calculation outputs have to be consistent with a small open electrical connection. The gap size of the drive and pick-up capacitor have to be close to the calculation result of chapter 5 ($30\mu m$) and must be larger than the thickness of kapton paper (12 μm) that we used to clean the gap. It turns out that only the first five points in the figure 4.2 have the gap size in the range specified above. Those points correspond to pick-up capacitance between $15pF$ to $19pF$. Hence, only the fifth point has match value of gap size and pick-up capacitance. However, the C_s is much bigger than capacitance calculation from appendix (1.4 fF). Hence, this test indicates the electrical connection is in good condition at low temperature. We know also that the electrical connection is in the good condition at the room temperature.

4.1.2 The TDO frequency and quality factor as a function of temperature

The open electrical connection can also be tested by measuring the tunnel diode frequency and its quality factor as a function of temperature. Since there are many places in the cryostat that can contract and expand when the temperature is rising and lowering, there is possibility that at some places inside the cryostat the electrical connection may change. The post-disk contact is the most suspicious place. We should see smooth changes of the frequency and quality factor if there is no sudden open electrical connection while cooling or warming. Otherwise, we would see a jump in frequency or a quality factor having a large dip as the connection opens up.

Tunnel diode (TD) BD-7 is a special diode that becomes more powerful in low temperature. The LC oscillator at room temperature has a large dissipation. It only turns on at about 77 K. The quality factor of TDO resonance is better at low temperature than room temperature. We will see this fact later in the experimental section of this method. The I-V curve of the tunnel diode BD-7 as shown in figure 4.3 depends on temperature. The peak current in the I-V curve is bigger at low temperature than room temperature.

From the slope of the negative resistance region in the I-V curve, we can calculate the conductance of the tunnel diode. The conductance of the tunnel diode determines the quality factor of

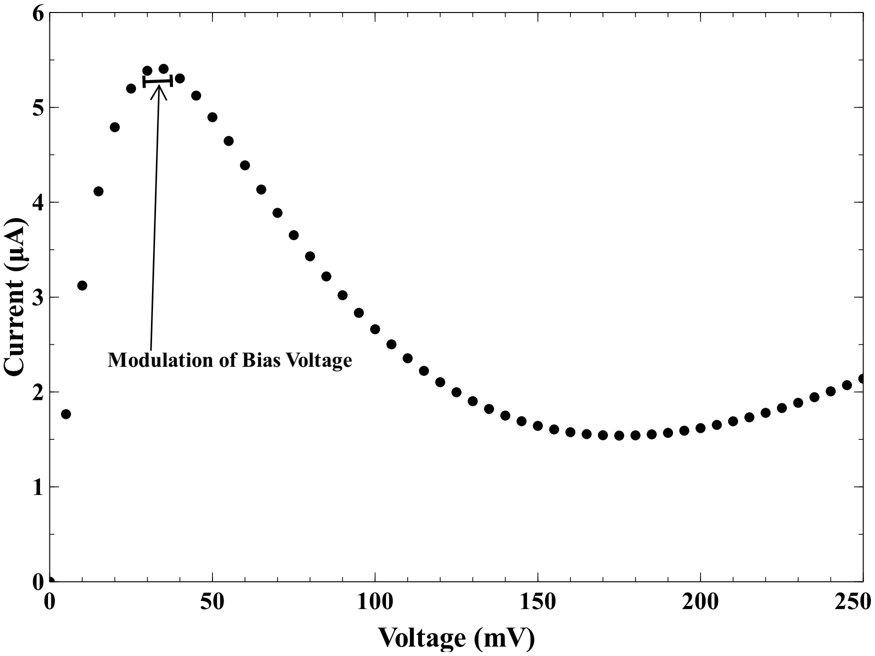

Figure 4.3: I-V Curve of Tunnel Diode BD-7 at liquid nitrogen temperature. The bar on the graph represent the range of bias voltage modulation.

TDO frequency. The relation is

$$Q(V) = \frac{1}{\frac{1}{Q_0} + z_0\, G(V)} \tag{4.9}$$

which Q_0, V, z_0 are the quality factor of TDO, the bias voltage and LC oscillator impedance. The LC oscillator impedance can be calculated using equation 4.10.

$$z_0 = 2\,\pi f_{LC}\; L\, \zeta \tag{4.10}$$

with ζ is the ratio between number of inductor coils that connected to the tunnel diode and total number of coils. f_{LC} is LC oscillator characteristic frequency which is about 72 Mhz. It has a small shift due to the diode junction capacitance since the capacitance is proportional to (V - 0.6 Volt)^n, where n is between -1/2 and -1/3. The shift can be written as

$$f_0(V) = f_{TDO} - \left(0.0003\,\frac{Hz}{V}\right)\, V \tag{4.11}$$

The transmission response signal is a simple Lorentzian. It is

$$resp(V,f) = \frac{A\, e^{(i\,\theta)}}{i\left(\frac{f}{f_0(V)} - \frac{f_0(V)}{f}\right) + \frac{1}{Q(V)}} \tag{4.12}$$

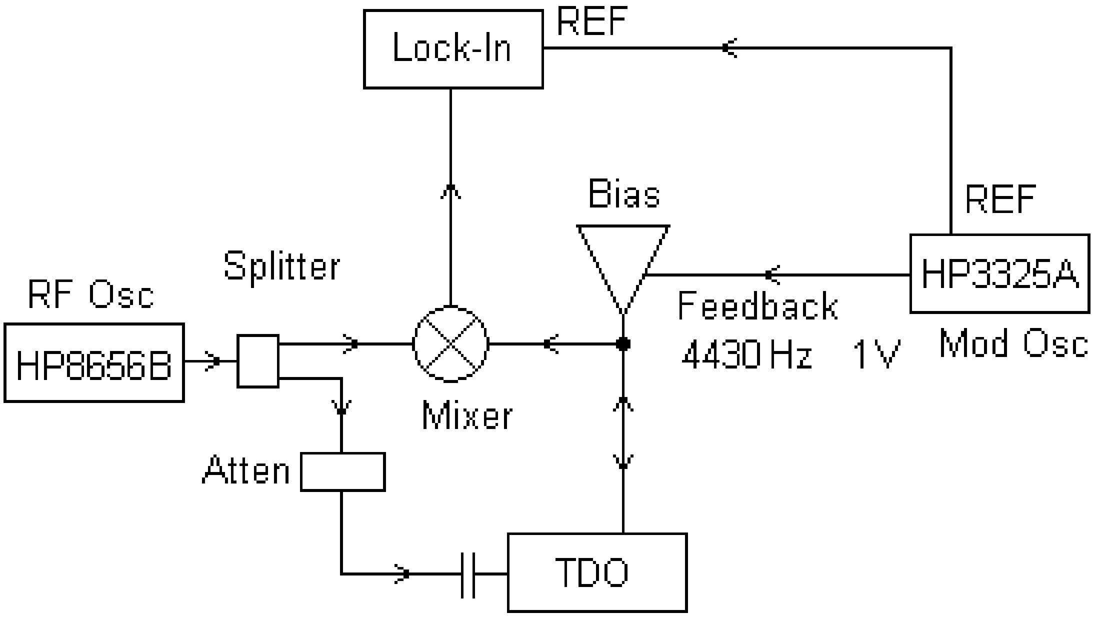

Figure 4.4: the scheme of non-oscillation TDO measurement

If we modulate the bias current of the tunnel diode, in figure 4.3, we can see that we also modulate the negative resistance. The loss of LC resonance is bigger at positive resistance region (positive slope in the I-V curve) than negative resistance region. Equation 4.9 and 4.12 show that by modulating the negative resistance, we modulate the amplitude and phase of the response.

The lock-in output is the synchronous average of the detected (mixed) transmission response signal. The real part acknowledges that the mixer only picks out one component of the Radio Frequency transmission.

$$signal = \frac{1}{2\pi}\int_0^{2\pi} Re\left(resp(V_b + V_o sin(\phi))\right) sin(\phi) d\phi \tag{4.13}$$

which V_b is bias voltage and V_o is the amplitude of voltage modulation.

4.1.3 Measurement of the TDO frequency and quality factor

The block diagram of the measurement can be seen in figure 4.4. The RF signal is produced by an oscillator HP 8656B. This signal is split into two paths. One path is coupling into the tunnel diode LC circuit via the third sound drive. There is an attenuator along this path to adjust the amplitude of this RF signal. The other path is the normal reference path into the mixer. This direct RF signal is mixed with the RF signal that is sent through the tunnel diode LC circuit. The amplitude and phase of signal passing through TDO turn into a DC output of the mixer. The mixed signal goes into the lock-in that detects changes of TDO transmission signal. The phase difference between two paths is modified by LC resonance. These changes are measured versus the RF frequency using equation 4.13. The modulation is produced by resistively coupling an AC voltage into the bias supply for the TDO. The bar in the figure 4.3 shows the range of bias current modulation. This changes the bias voltage applied to the tunnel diode by approximately 2mV/V.

4.1.4 Temperature measurement

Between room temperature and 77 K, we cool the cryostat by momentarily adding liquid nitrogen. We warm the cryostat by room temperature heat conduction back in. We need to have good temperature measurement sensitivity in the range between room temperature to liquid nitrogen temperature. The thermometer should be placed close to the cell to obtain best accuracy. The Bath thermometer is too far from TDO. The cell thermometer is insensitive for the temperature range around 77 K. Hence, we used the still thermometer to measure the cell temperature. The still thermometer measures temperature of a warmer stage of the refrigerator. It is connected to a thermal shield surrounding the cell and has more sensitivity to temperature around 77 K to 300 K. We calibrate the still thermometer to know precisely what the conversion resistance to temperature is. We need to get the resistance values of room temperature and liquid nitrogen temperature to start the conversion. The resistance values for 77 K and 297 K are 468.613 Ω and 379.5 Ω, respectively. These are measured by the cryostat wheatstone bridge.

We measured the resistance of an identical sensor as temperature changes. We used the same resistor as was used in SR510. We put the resistor down on a heat sink then put them inside a container. We connected the resistor to the digital multimeter to measure its resistance. We put the liquid nitrogen slowly to the container. We measured temperature using a mercury thermometer. The linear fitting curve have agreement with previous measurement done by Fred Ellis $\left(\frac{dR}{dT} \approx -0.100\Omega/K\right)$. The figure 4.5 shows that the still thermistor resistance changes as a function of temperature is $-0.113\Omega/K$. In the thermistor theory, this temperature dependence can be model as disordered semiconductor. The model tells us to calculate resistance as function temperature including a defect factor γ using

$$R(T,\gamma) = R_0(\gamma)\, exp\left(\frac{T_0(\gamma)}{T}\right)^{\gamma} - 91.5\,\Omega \tag{4.14}$$

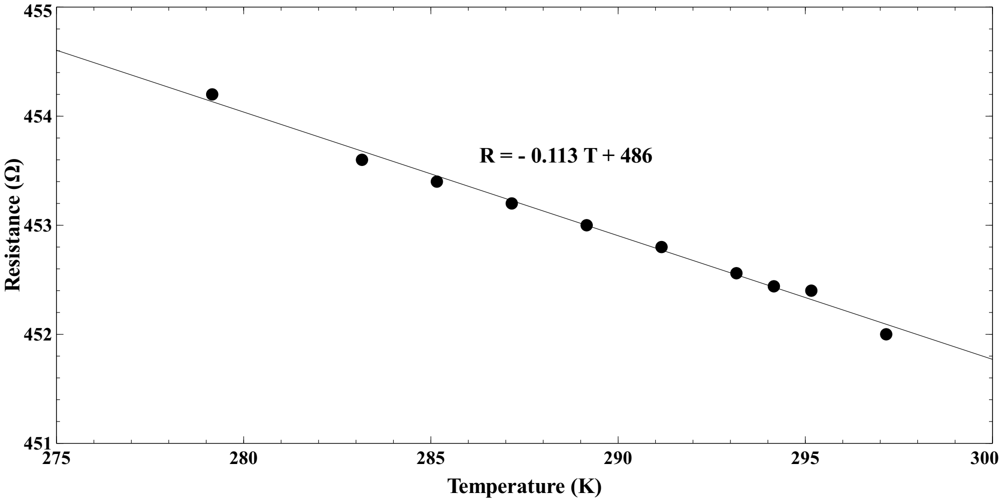

Figure 4.5: Graph of still thermistor resistance as a function of temperature. The line is curve fitting of the experimental data.

The 91.5 Ω is needed since there is discrepancy between the cryostat wheatstone bridge measurement and the color code of resistance.

Based on room temperature and liquid nitrogen resistance and $\frac{dR}{dT}$, we calculated the value of $R_0(\gamma)$, $T_0(\gamma)$ and γ. The value of γ is chosen in such way that derivative of equation 4.14 respect to T match the slope of fitted line in figure 4.5. Once we found γ, we calculate the value of $R_0(\gamma)$ and $T_0(\gamma)$. Hence, the conversion temperature to resistance is

$$R = 435.707\, exp \left(\frac{15.646}{T}\right)^{0.867} - 91.5\,\Omega \tag{4.15}$$

We can reverse equation 4.15 to obtain conversion resistance to temperature.

4.1.5 Resonance Analysis

We modified a least-squares fitting program for third sound and mechanical resonances to analyze the modulations of the TDO transmission. The response signal is measured by calculating the difference between two responses of drive signal. For each response, signal we first need to measure the differential conductance (G). We measure two values of G that correspond to two values of the tunnel conductance at the upper and lower limit of the bias voltage modulation.

We read voltage bias using a digital multimeter as connected to the HP 3325 signal generator and the tunnel diode. We modify the bias voltage with low frequency (0.07 Hz) to capture the

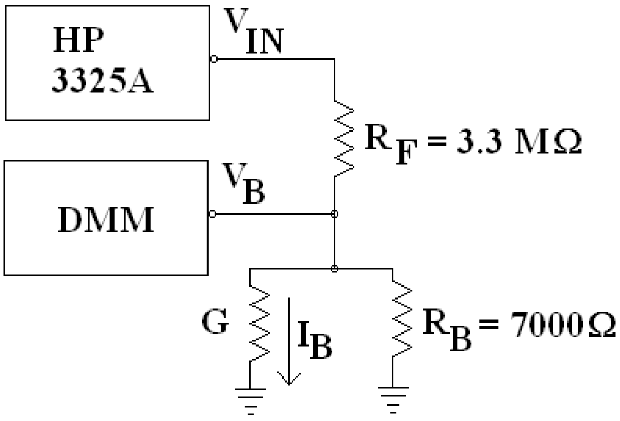

Figure 4.6: The HP3325A is employed to modulate the bias voltage. The bias voltage is read by Dgital Multimeter (DMM).

sinusoidal changes of the bias voltage. We took average value of it for 10 cycles of modulation to get good statistic value of G. We used the average bias voltage to calculate G. Since it depends on the value of bias current, we calculated it using the value of bias voltage, bias resistance (R_B) and feedback resistance (R_F).

$$I_B = \frac{V_{in} - V_B}{R_F} - \frac{V_B}{R_B} \tag{4.16}$$

which V_{in} is the input voltage from the HP 3325 signal generator.

$$V_{in} = V_o\, cos\Phi \tag{4.17}$$

The oscillatory input voltage near the peak can be expressed as

$$V_{in} = V_o \left(1 - \frac{1}{2}\Phi^2\right) \tag{4.18}$$

The bias voltage also follows the dynamic of V_{in}, so we can write it as

$$V_B = V_o - \alpha\Phi^2 \tag{4.19}$$

which α is the curvature of cycle peak versus phase. Hence, the G is

$$G = \frac{\frac{\partial I_B}{\partial \Phi}}{\frac{\partial V_B}{\partial \Phi}} \tag{4.20}$$

$$G(V_0) = \frac{\frac{1}{R_F}\left(-V_o\Phi\right) - \left(\frac{1}{R_F} + \frac{1}{R_B}\right)\left(-2\alpha\Phi\right)}{-2\alpha\Phi} \tag{4.21}$$

So, we can simplify the equation above as

$$G(V_0) = \frac{1}{R_F}\frac{V_o}{2\alpha} - \left(\frac{1}{R_B} + \frac{1}{R_F}\right) \tag{4.22}$$

Now, we use the G value of two different the bias voltages in equation 4.12. The equation 4.13 can be approximate to the more simple form for small bias voltage oscillation.

$$resp(V_b + \epsilon, f) \approx resp(V_b, f) + \epsilon\frac{\partial\left(resp(V_b, f)\right)}{\partial V_b} + ... \tag{4.23}$$

which ϵ is equal to $V_o sin(\phi)$. The derivative of the respond function with respect to the bias voltage can be expressed with difference quotient.

$$\frac{\partial\left(resp(V_b, f)\right)}{\partial V_b} = \frac{resp(V_b + V_o, f) - resp(V_b - V_o, f)}{2V_o} \tag{4.24}$$

The equation 4.13 can be written as

$$signal = \frac{1}{2\pi}\int_0^{2\pi} sin(\phi)\left[resp(V_b, f) + \epsilon\frac{\partial\left(resp(V_b, f)\right)}{\partial V_b} + ...\right] d\phi \tag{4.25}$$

The first term is the integration of sine function from 0 to 2π that give us a zero. The second term is the integration of squared of sine function from 0 to 2π that give us factor of one-half. Hence, the signal is

$$signal = \frac{1}{4}\,\left[Re(resp(V_b + V_o, f) - Re(resp(V_b - V_o, f)\right] \tag{4.26}$$

This is not an exact calculation since we are using $G(V_o)$ instead of $\langle G\rangle_{V_o sin\theta}$. The other reason is the Taylor expansion. We only used the second order of expansion to approximate an equation 4.25. Those approachs are primarily afffect the amplitude of the response signal. The value of TDO frequency is unchanged since it is where the response occur. The quality factor is also unchanged since it is quantify how wide the response is.

4.1.6 Results

We measured the frequency and quality factor as a function of temperature as we cooled temperature down from room temperature to liquid nitrogen temperature. We also took similar measurement as we raised temperature up, from liquid nitrogen temperature to room temperature. We put nitrogen slowly to the bath in such way that the temperature will be cooled down slowly. We stopped putting nitrogen when we reached temperature that we want to be measured. Since this

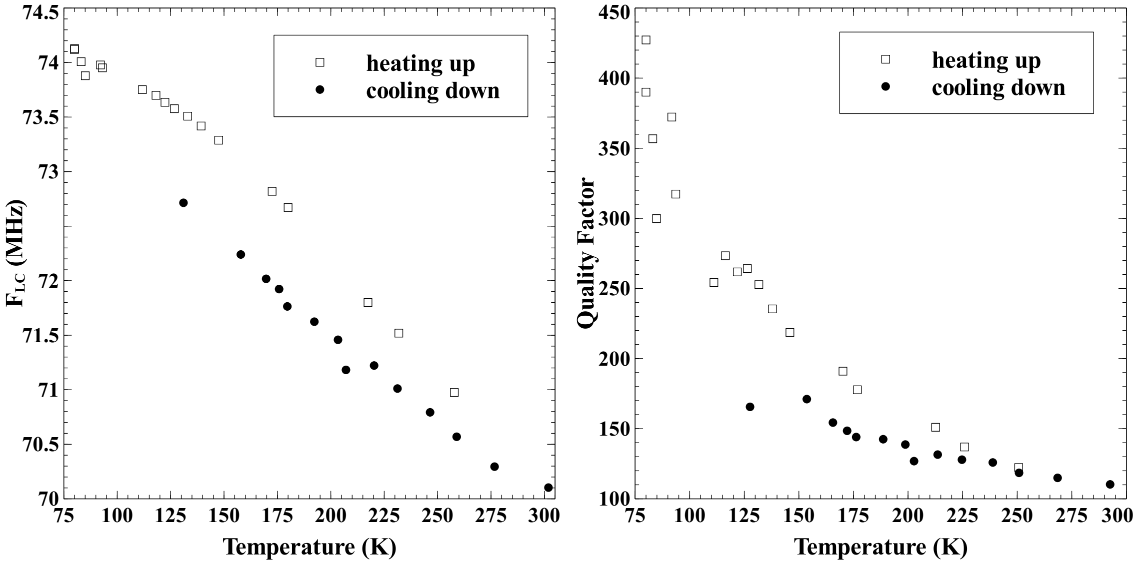

Figure 4.7: The graph of frequency of TDO and quality factor versus temperature as the bath temperature raising up and lowering down.

is not an equilibrium, the temperature will be changing as we do the measurement. Hence, we decided to take measurement when the temperature has flattened out, before it rises up again. For measurements in the other direction, we just let the bath temperature rise up since the temperature changing is slow enough to do the measurement.

We analyzed the signal from bias voltage modulation by fitting it to the theoretical model. We applied the AC voltage at 1 Volt and 4430 Hz to modulate the bias voltage. There is insignificant jump of the frequency and quality factor as in figure 4.7. The only issue is a hysterisis in the frequency graph. But, we think this issue is not due to poor electrical connection where we expect either a rapid change or a dip in the quality factor graph. The hysterisis is due to poor thermal contact. The cell temperature response lags behind the still and bath temperature. Hence, we can conclude that there is no loose connection in the circuit. It agrees with the conclusion of section 4.1.2.

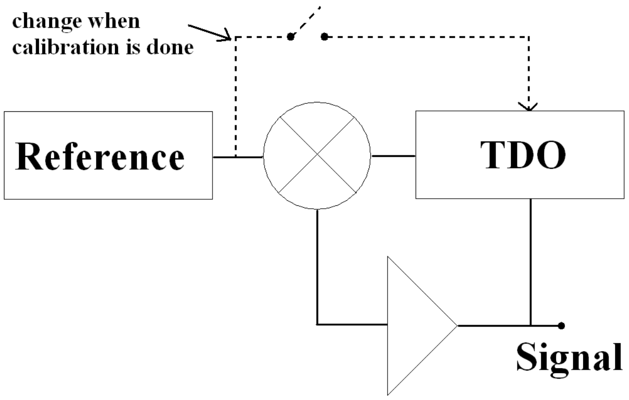

Figure 4.8: The experimental setup for investigating the influence of external signal to the lockin range of Phase Locked Loop system.

4.2 The Filter Capacitor

4.2.1 Introduction

The sensitivity ratio problem might also be explained by an external signal interfering with the operation of the Phase Locked Loop (PLL). The external signal coming from the reference could get into the PLL through several paths. In this section, we identify those paths that are most likely alternative paths to the intended feedback loop.

4.2.2 Experiment

The external signal that potentially interferes with the tunnel diode frequency is the signal that has frequency close to the TDO frequency (74 MHz). The cryostat is completely shielded by thick metal walls of the dewar, so feedback paths must be through electrical connections that go from inside to outside. Hence, we test several paths by intentionally applying 74 MHz signal. Those paths are the drive, the drive with and without the 3X-Box, the bath level detector circuit, the mixing chamber thermometer circuit and many other sensors from the electronic rack to inside the cryostat. We applied 74 MHz to these paths and varied the signal amplitude and measured the lock-in range of the PLL system.

The signal generator used for the PLL is split and is connected to an attenuator. The attenuation magnitude can be varied from 0 dB to 120 dB. The attenuation at 0 dB corresponds to 224 mV signal amplitude. Each path will respond differently. The signal is then connected to each path.

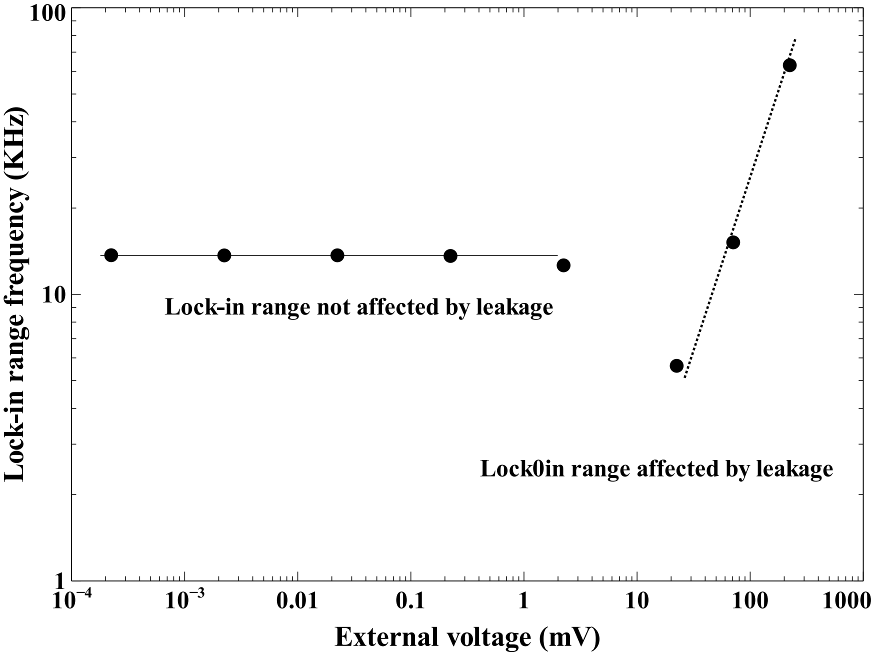

Figure 4.9: The lock-in range frequency as a function of external amplitude of input signal for the drive with the 3X-Box path and PLL feedback on.

Then, we set the amplitude of the signal. For each amplitude, we vary the frequency on the Lock-in SR 530 through the TDO frequency to observe the lock-in range. It is the DC output of mixer signal. We repeat the experiment with no PLL feedback.

We can see the changes of lock-in range as a function of the external signal amplitude as shown in figure 4.9 for the drive capacitor with the 3X-Box path. There is a region where the lock in range stays almost constant as the external signal amplitude changes. It means that the TDO lock-in range frequency is not affected by the external signal. That region is region A. There is also range where the lock-in range changes as external signal amplitude changes. We call this range as region B. Hence, we can find the minimum of external signal amplitude that can modify the TDO lock-in range frequency. It is the value of external signal amplitude in the region B that has lock-in range frequency equal to the lock-in range frequency in the region A. It can be calculated by power law fitting to the data points in the region B. The transition region between region A and B may be the region where the actual path is more dominant than the tested path.

The table 4.1 shows the minimum of external signal amplitude that can alter the lockin range of PLL for the different paths. The Feedback Off setup is the setup by excluding the intentional

Path	Amplitude (V)		Filter
	Feedback On	Feedback Off	
Drive capacitor	$1.86.10^{-4}$	$6.96.10^{-6}$	Without
	$5.80.10^{-3}$	$< 2.24.10^{-7}$	With
Drive capacitor with the 3X-Box	$4.94.10^{-3}$	$3.94.10^{-4}$	Without
	$6.82.10^{-2}$	$1.51.10^{-4}$	With
Bath level detector	$> 2.24.10^{-1}$	$3.68.10^{-2}$	Without
	$> 2.24.10^{-1}$	$8.59.10^{-4}$	With
MC thermometer	$4.26.10^{-2}$	$7.26.10^{-3}$	Without
	$> 2.24.10^{-1}$	$1.13.10^{-3}$	With
Electronic rack	$> 2.24.10^{-1}$	$1.46.10^{-2}$	Without
	$> 2.24.10^{-1}$	$1.61.10^{-1}$	With

Table 4.1: Minimum of external signal amplitude that can alter the lockin range of Phase locked Loop for different paths. The normal setup for the experiment is sending the frequency through drive capacitor with the 3X-Box and using the feedback.

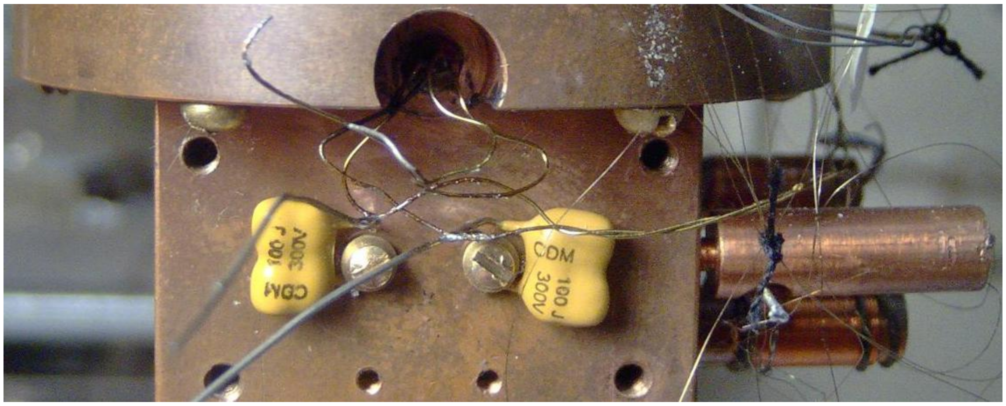

Figure 4.10: 100 pF filter capacitors are installed parallel to the drive capacitors.

PLL DC feedback loop. The less amplitude means the most sensitive path for unintended external feedback signals. The most sensitive path is the drive capacitor path. It is followed by drive capacitor with the 3X-Box path. In the third sound experiment, we usually use the drive capacitor with the 3X-Box path.

4.2.3 Filter considerations

We tried to improve the detection system by installing a filter for the unintended feedback signal. This filter is a capacitor placed in parallel to the path in question. Since we have more identified the drive path as the most sensitive path, we put the capacitor in parallel with that path. The capacitor has to have small size to be fit in the outside of the cell wall. It also has to work at low temperature. Its capacitance can not be too big that the drive signal ($<\approx 35$ KHz) is attenuated. Its capacitance also has the value that can avoid any resonances around 74 MHz.

We calculated the impedance as a function of filter capacitor. We call the impedance of LC circuit as z_1. The connection cable has an impedance of z_0 and electromagnetic velocity of v. We can write the voltage and current as a function of length that propagate along the cable as

$$V(x) = V_+ \, exp(-i\,kx) + V_- \, exp(i\,kx) \tag{4.27}$$

$$I(x) = \frac{V_+}{z_0} \, exp(-i\,kx) - \frac{V_-}{z_0} \, exp(i\,kx) \tag{4.28}$$

which V_+ and V_- are the amplitude of the wave propagating to the right and to the left, respectively. At x=0, the current equal to zero since the external impedance is infinity. Hence, we can have the

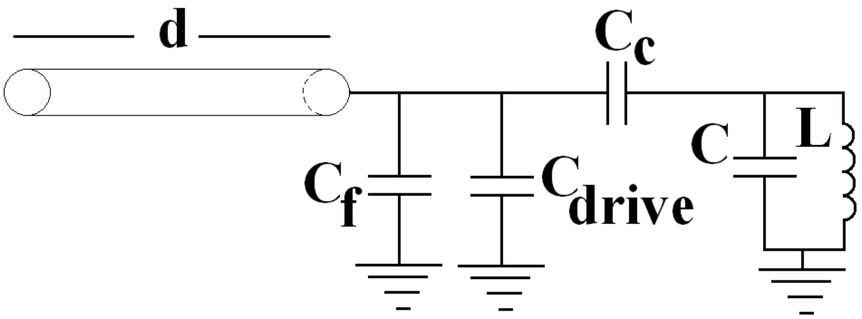

Figure 4.11: The electronic circuit of filter capacitor.

relation

$$V_+ = -\,V_- \tag{4.29}$$

We introduce x as $\frac{\omega}{\omega_0}$, λ as $\frac{\omega_0\,d}{v}$ and ς as $\frac{z_0}{\sqrt{\frac{L}{C+C_c}}}$ which ω_0 is equal to $\left(L\ (C+C_c)\right)^{-1}$. C is the total capacitance that includes the pick-up capacitance and stray capacitance. C_c is the coupling capacitance which is the capacitance of the electrode backside. We also add the 100 pF filter capacitor (C_f) in the equation to be

$$\frac{tan(x\lambda)}{\varsigma} = \frac{1}{\frac{1}{\frac{1}{x}-0.882\,x} - \frac{1}{x\frac{C_c}{C}}} - x\frac{C_f+C_d}{C} \tag{4.30}$$

The ratio between C_c and $C+C_c$ is 0.118 and the ratio between C_f+C_d and $C+C_c$ is 8.861. The RG 58 cable has z_0 equal 50 Ω and v equal to 0.67 c. Hence, the value of ς is 0.295. The equation 4.30 has multiple roots for a given λ. We plot two roots as a function λ. In the figure 4.12, we can see that the filter capacitance makes the two points closer each other especially when λ equal to 11.4 as shown in the shaded region in figure 4.12. The closer the distance is to the horizontal assymptote at $x = \frac{1}{1+\frac{C_c}{C}}$, the less influence the drive lead connection will have on the LC circuit. The crossings represent the lead resonances which would be the worst case, and should be avoided. Since the frequency might have two different values that is separated by difference between two roots. In the worst situation, we want to have the separation is close enough since we want to reduce the inaccuracy of TDO frequency. The experiment drive cable length corresponds to λ equal 12.7. Fortunately, it is not too close to the worst region. The situation becomes better with filter capacitor addition since the worst region is farther from experimental λ.

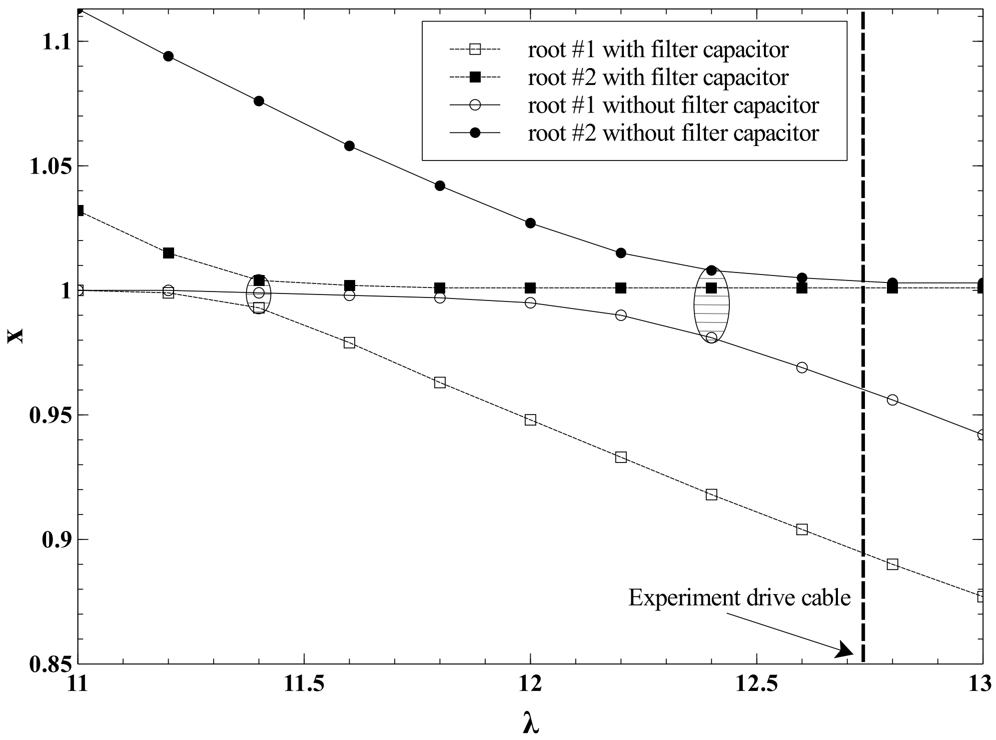

Figure 4.12: The root x is the solution of equation of motion of drive circuit. This is also the resonance frequency of the circuit. λ is scaling length of drive cable. The shaded area is the region where the worst case happen. It is the region where two roots of the equation of motions become very close to each other. The vertical dash line indicates λ corresponds to the length of experiment drive cable. Addition of filter capacitor bring the worst region farther from the experiment situation.

4.2.4 Experimental result

The filter capacitor was placed in the outside of the cell. It is attached to the side wall of cryostat with short lead. Since the wall size close to the drive lines has small size that is 0.5 inches wide and 0.8 inches long, the filter capacitor also has to have a small size. It also need to have low dielectric loss or dissipation factor (DF). Mica capacitors have a DF of 0.005 and 0.0003 when it operates at 60 Hz and 1 MHz, respectively. The power dissipated (P) by the capacitor (C) can be calculated as

$$P = V^2 \omega C(DF) \tag{4.31}$$

which V and ω are the operating voltage and frequency. For a maximum third sound drive, a 100 pF capacitor at 30 Volt drive voltage at 1 KHz, the power dissipated in the capacitor is estimated to be $1.696.10^{-7}$ Watt. This is about the same as the tunnel diode. The power is also expected to go down at low temperatures.

We use silver mica capacitors from Newark Electronics. Its length is 0.27 inches, width is 0.24 inches and thicknes is 0.18 inches. It has voltage rating of 300 DC Volt, operating temperature range between -55 C to 125 C and capacitance tolerance of 5%. We tested the capacitor changes as we cooled down from room temperature to liquid nitrogen temperature. The capacitance changes ratio per temperature changes ratio $\left(\frac{\frac{\Delta C}{C}}{\frac{\Delta T}{T}}\right) \approx -9.10.10^{-3}$.

We measured again the minimum of external signal amplitude for different feedback paths using the technique described in the previous section. By adding the filter capacitor, we have increased the minimum of external signal amplitude on the drive capacitor path. We found that the minimum of external signal for the drive path with the 3X-Box and feedback on with filter capacitor is bigger than without filter capacitor. Table 4.1 also shows how important is the 3X-Box to insulate the signal generator from the cryostat. We can see from the table that the minimum of external signal of drive capacitor with the 3X-Box is bigger than only drive capacitor.

4.3 Bias circuit plate

4.3.1 Introduction

The TDO circuit needs to have good thermal sink for diode. It also needs to be electrically insulated. The finger plate where the tunnel diode, resistor, and capacitor are located is not in the

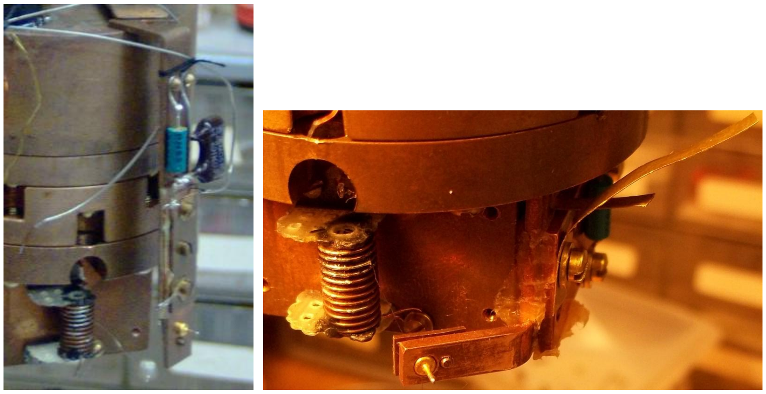

Figure 4.13: The left figure is old bias circuit plate. The right figure is new bias circuit plate.

stable position. The finger plate is clamped to the cryostat to make good thermal conductance. It consists of three plate that are clamped together. Insulating spacers between the plates prevent each plate from being electrically connected. The upper and lower part of the plate are ground, with the middle part connected to the bias side of the TDO circuit. The heat from the tunnel diode bias current needs to be conducted through this plate to ground. A large area of the insulating spacers is needed.

The coaxial wire coming from the top of the cryostat is connected to the parallel configuration of resistor (R_B) and capacitor (C_B). The body of the tunnel diode is connected to the middle plate. The outside of the coaxial wire also grounded to the upper (ground) plate. The TDO signal depends on the capacitance of bias capacitor. The larger the capacitance, the smaller the amplitude of bias signal. It needs to be large enough to provide an AC ground for the TDO but not so large that the TDO signal returned to room temperature is surprassed. We found that the TDO signal depends on the mechanical stability of the connection on the finger. We built a new set of plates to improve electrical connection and also preserve good thermal conduction. The new plate have larger area that makes the thermal conduction better than the old plate. It also provide shorter heat path from the tunnel diode to the cryostat body. The tunnel diode position in the new plate is shorter to the inductor. It improves the mechanical stability of the wire connection from the tunnel diode to the inductor.

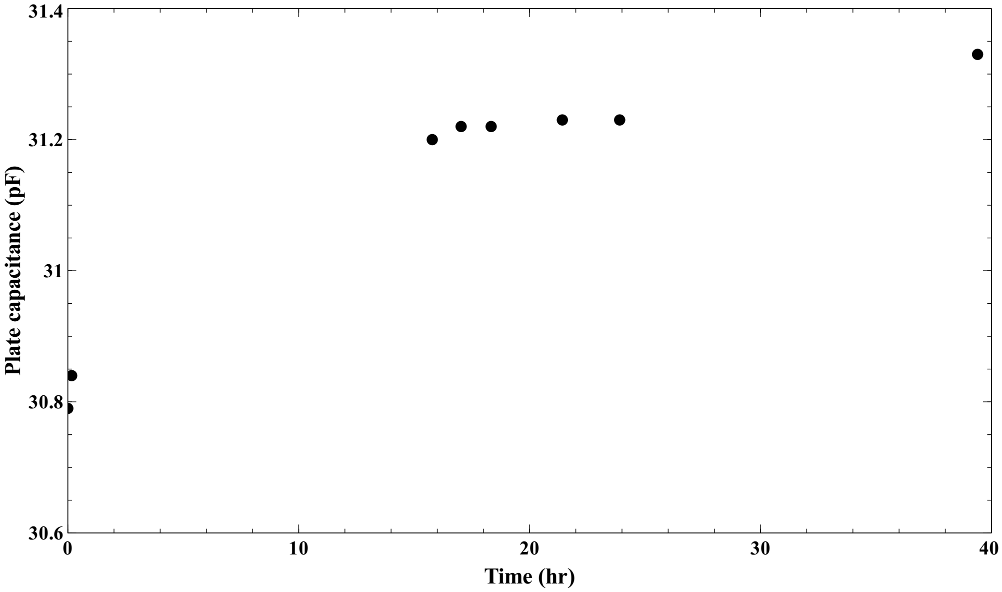

Figure 4.14: The graph of bias plate capacitance versus time

4.3.2 Plate fabrication

Instead of the three plates that are clamped together, we use three plates and the cryostat body as the third plate (lower plate). We also found from previous experiment that lower capacitance is, the bigger the bias signal. We assume that the arrangement of two plates and cryostat body with the spacer act like capacitor. We need to find the right thickness of dielectric to match with the optimum value of capacitance, which we determined to be 20 - 30 pF of capacitance. The dielectric material is glass microfiber filter that has thickness 0.65 mm. With the dielectric is 2.5 times bigger than vacuum dielectric, the capacitance is expected to be about 25 pF.

Heat transfer is an important thing to consider to build this capacitor. Heat from the TDO must be well transferred to the outer part of the cell which is the base of the refrigerator. This mechanism needs a medium that has good heat conductivity. The microfiberglass filter paper is soaked in a grease solution to make good heat conductor material. Grease act as a path for conducting heat. The grease need to be mixed with Trichloroethylene (TCE) to make the grease absorb well into the filter paper. TCE will then easily evaporate, leaving the grease behind. We made a measurement of the actual capacitance. Since there is changing pressure due to the grease and filter paper relaxation, the thickness of dielectric is changing. The changes of capacitor can be seen in figure 4.14. We can see that the final value of the capacitance is about 31 pF. Hence, the total capacitance including the 100 pF mica capacitor is 131 pF.

The 100 pF capacitor is connected to the upper plate and the center plate. The connection on the upper plate is grounded using screws that go through the center plate into the cryostat body. Connection to the center plate made by a small L-shaped brass tab soldered to the center plate. Another small plate is soldered to the center plate, close to the edge. This small plate is connected to the coaxial wire coming from the top of the cryostat.

The center plate has a small arm that bends in an angle in such way that the end of the arm is close the inductor. The tunnel diode is clamped at this end. The inductor shield had to be cut to make space for this arm. A fine wire connection from tunnel diode to the inductor is shorter than the previous set up. A second ground wire to the inductor shield since the plate was eliminated mounted much closer to the inductor.

4.4 Drive amplitude and phase

4.4.1 Introduction

The goal for this experiment is to properly calibrate the 3X-Box and determine its amplitude and phase for testing sensitivity ratio at mechanical resonance. There is a possibility that the phase and the amplitude of the drive voltage is different at the signal generator than at the drive electrode inside the cell. The difference comes coming from the length of wire taking the signal into the cryostat that has capacitance and resistance that could alter the phase and amplitude of the drive voltage. Another source of discrepancy is the 3X-Box. The output voltage is about three times the input voltage. We need to measure the output phase and amplitude as a function of drive frequency. This information can be collected from the DSP lock-in amplifier that connected to the 3X-Box output. There are two outputs on the 3X-Box that correspond to drive 1 and drive 2. Each of them is connected to a separate transformer. These two transformers may have different responses for the same input voltage.

4.4.2 Experiment

The output voltage of the 3X-Box is monitored by the DSP lock-in amplifier to measure phase and amplitude as shown in figure 4.16. The connection uses one meter cable R58. It has capacitance

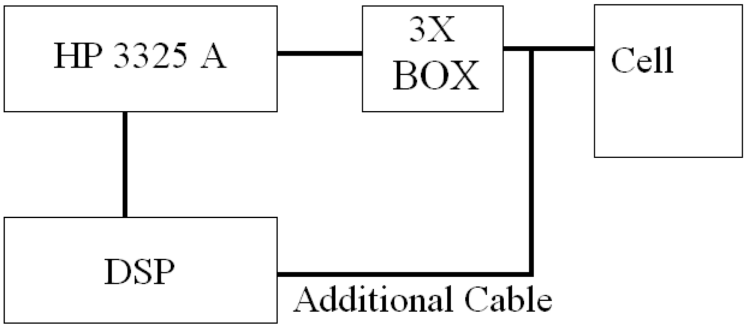

Figure 4.15: The experiment setup for investigating the amplitude and phase of the 3X-Box as a function of additional capacitor. Normally, the lock-in and additional cable are not in the drive circuit.

Length (meter)	Capacitance (pF)
0.33	34.419
1	106.812
1.89	194.430
2.39	224.510

Table 4.2: The capacitance of R58 cable for several lengths.

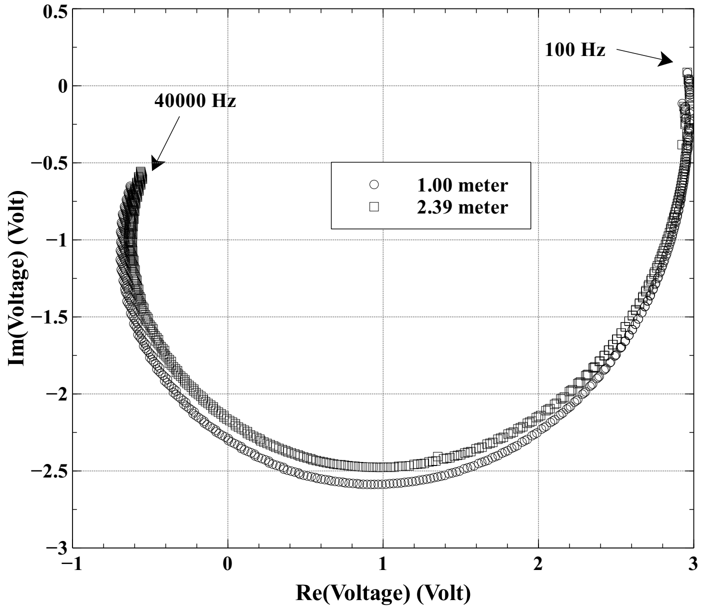

Figure 4.16: The experimental value of the 3X-Box output for two different length of cables in the frequency range between 100 Hz and 40 KHz.

per length 100 pF/meter and impedance of about 50 Ω. The experiment is repeated for different length of cables. Hence, we can get the profile of t he output voltage for different additional capacitance values as shown in figure 4.16. Then, we can find the function that fits the profile to make a correction of the additional load. To get a precise capacitance measurement of the cable, we measured the reactance of the cable using an impedance meter. Table 4.2 shows the capacitance for four different length of R58 cables.

4.4.3 Fitting the function

Using the Kirchoff law and voltage divider formula, we calculated the expected output voltage of the 3X box as a function frequency as modeled by the circuit in figure 4.17. The voltage equation of transformer as a function of input and output currents (I_1 and I_2) are

$$V_1 = L_1(\tfrac{dI_1}{dt}) + M(\tfrac{dI_2}{dt})$$
$$V_2 = L_2(\tfrac{dI_2}{dt}) + M(\tfrac{dI_1}{dt})$$

which V_1 and V_2 are input and output voltage of transformer, respectively. The L_1 and L_2 are input and output self inductance, respectively. M is mutual inductance that satisfy $M^2 = \mu^2 L_1 L_2$

ΔC (pF)	C (pF)	L_1 (H)	L_2 (H)	R_1 (ohm)	R_2 (ohm)	μ
64.419	579.386	1.30658	11.33611	1305.78	2280.67	0.9965
136.812	633.252	1.27162	11.06313	1301.29	2228.34	0.99648
224.43	658.388	1.26533	10.99798	1335.09	2539.58	0.99631
254.51	690.422	1.25592	10.93386	1321.5	2414.85	0.99636

Table 4.3: The fitting parameters for four different length of R58 cables. ΔC is the additional cable capacitance plus the capacitance of DSP lock-in amplifier.

and μ is coefficent of coupling between two inductor. It has value close to unity for the transformer.

The Kirchoff law for input voltage of the transformer is

$$V_{osc} = I_1 50 + I_1 R_1 + V_1 \tag{4.32}$$

V_{osc} is the AC voltage from the signal generator. The output of signal generator is also connected in series with an internal 50 Ω resistor. R_1 is resistance of the 3X-Box input coil windings.

$$V_{out} = I_2 \frac{1}{i\omega C} + I_2 R_2 + V_2 \tag{4.33}$$

V_{out} is the output voltage from the 3x box with extra capacitance C. I_2 is a current flowing on secondary part of the circuit. R_2 is resistance of the 3x box output coil windings. I_1 and I_2 satisfy the following relation

$$I_1 = \tfrac{V_{osc} - V_1}{50 + R1}$$
$$I_2 = \tfrac{-V_2}{R_2 + \frac{1}{i\omega C}}$$

Using the oscillatory solution of currents I_1, I_2 and voltage V_{osc}, we can construct a matrix. It is

$$\begin{bmatrix} V_{osc} \\ 0 \end{bmatrix} = \begin{bmatrix} i\omega L_1 + (50 + R_1) & i\omega\mu\sqrt{L_1 L_2} \\ i\omega\mu\sqrt{L_1 L_2} & i\omega L_2 + (R_2 + \frac{1}{i\omega C}) \end{bmatrix} \begin{bmatrix} I_1 \\ I_2 \end{bmatrix}$$

Hence, we can find I_2 and V_{out},

$$I_2 = \frac{V_{osc}(-i\omega\mu\sqrt{L_1 L_2})}{\left[(50 + R_1)(i\omega L_2) + i\omega L_1 \left(R_2 + \frac{1}{i\omega C}\right) + \omega^2 L_1 L_2(\mu^2 - 1)\right]} \tag{4.34}$$

$$V_{out} = \frac{V_{osc}(-i\omega\mu\sqrt{L_1 L_2}\frac{1}{i\omega C})}{\left[(50 + R_1)(i\omega L_2) + i\omega L_1 \left(R_2 + \frac{1}{i\omega C}\right) + \omega^2 L_1 L_2(\mu^2 - 1)\right]} \tag{4.35}$$

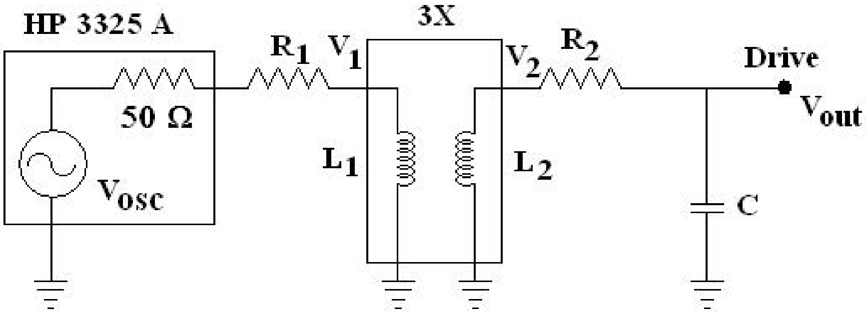

Figure 4.17: The signal generator and the transformer 3X-Box.

ΔC (pF)	C (pF)	L_1 (H)	L_2 (H)	R_1 (ohm)	R_2 (ohm)	μ
0	549.95	1.3156	11.412	1292.6	2159.3	0.9966

Table 4.4: The six parameters for zero additional capacitor.

There are six fitting parameters in the function to fit the experimental value of the 3x box output. They are C, L_1, L_2, R_1, R_2 and μ. The value of capacitance (C) is the sum of DSP capacitance (30 pF), cable down to cryostat capacitance, filter capacitance (200 pF), drive capacitance (24 pF) and the extra cable capacitance. We also know the ratio of the secondary and primary self inductance is about 9. We calculated the output voltage at any frequency. We are mostly interested in the higher frequencies around at 35 KHz, which is close to the mechanical resonance frequency. We also calculated the output voltage in the range of the third sound frequency, and confirm that it is not very frequency dependent.

4.4.4 The true output of the 3X-Box

Table 4.3 shows the fitting parameters for different test cable lengths. The next step is to extrapolate the six parameters to deltaC equal zero. This is the condition where the experiments are done. A linear extrapolation gives the result is shown in table 4.4.

We use these values to correct the output voltage of the 3X-Box using equation 4.35 for any frequency that we are interested in. The amplitude and phase of the output voltage corrects the sensitivity ratio of the mechanical and third sound resonance signal by more accuratley representing the drive amplitude and phase.

Chapter 5

Experimental Results

The mechanical resonance of the disk and third sound resonance are explained in this chapter. It is followed by an explanation of the third sound amplification by stimulated condensation results. We also discuss in more detail the capacitor gap size calibration which is accomplished by filling and pumping the cell with liquid helium and liquid nitrogen.

5.1 Gap Calibration Result

In chapter 2, we studied how to calculate the capacitor gap size by pumping and filling the cell. We took measurements of the TDO frequency changes as the cell was filled with liquid helium and liquid nitrogen. We needed to obtain a more precise capacitor gap size to calculate the theoretical value of the film thickness amplitude in the third sound mode, since the film thickness oscillations are monitored by changes in the capacitor dielectric value. This relation is the basis of the sensitivity ratio.

The figure 5.1(a) and 5.1(d) show the frequency changes as a function of time for liquid nitrogen and liquid helium filling process. We can see that there is a frequency jump. This jump comes from the narrow gap of the capacitor being suddenly filled by liquid. Hence, we can calculate the capacitor gap by analyzing the TDO frequency changes. This frequency jump needs to be corrected as the jump includes the TDO frequency changes by the capacitor edge wicking, as discussed in chapter 2.

The pumping process gives more precise details about the capacitor gap size. The frequency

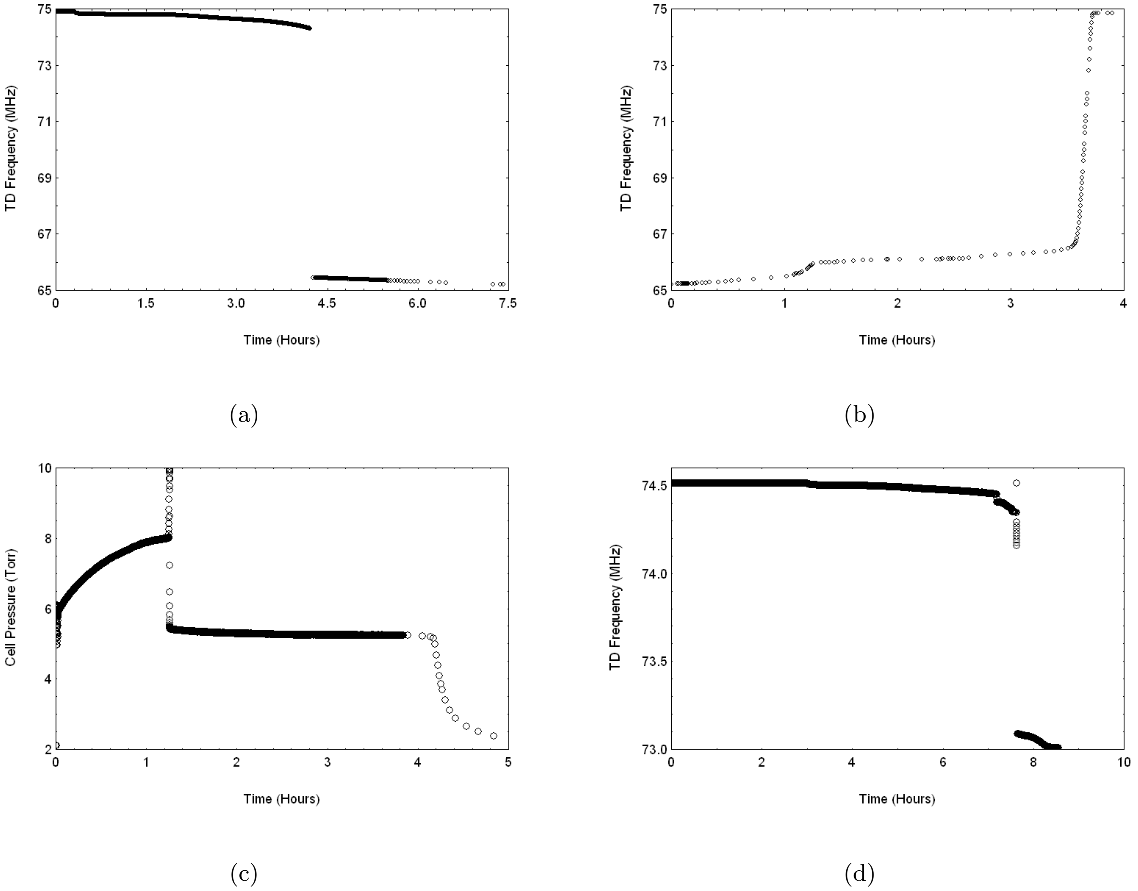

(a) (b)

(c) (d)

Figure 5.1: (a) The TDO frequency changes as a function of time for filling process with liquid nitrogen. (b) The TDO frequency changes as a function of time for pumping process with liquid nitrogen. (c) Cell pressure as a function of time for pumping process after the cell is filled with liquid nitrogen. (d) The TDO frequency changes as a function of time for filling process with liquid helium.

change as a function of time is shown in figure 5.1(b). There is a small of frequency jump in the beginning in the pumping process dug to the liquid level falling below the capillary entrance into the cell. We also verify this conclusion by looking at the cell pump line pressure as a function of time as shown in figure 5.1(c). With the liquid level above the capillary, the pressure starats at about 7 Torr. The liquid keeps being pumped turning into vapor in the fill tube until the liquid level falls below the filling tube. At this moment, pressure decreases to 3.8 Torr and is almost constant. The liquid level becomes lower and lower. However, the capacitor gap is still filled with liquid. Since the capacitor gap is small, it is hard to drain out the liquid from it. When the liquid becomes unsaturated, the pressure goes down to about zero, as seen in figure 5.1(c) after 4 hours. However, the frequency jump happened before the pressure went down to this level. This means that the liquid is drained out from the capacitor gap before it becomes unsaturated.

From the pumping process, we know that the frequency jump is only caused by draining the liquid out from the capacitor gap. Hence, we can use this frequency jump without any correction-unlike the filling process-to calculate the capacitor gap size. We use the value of the top of the frequency jump as f_{empty} and the value of the bottom of the frequency jump as f_{filled} to equation 2.13 to get the ratio of pick-up capacitor capacitance and the total capacitance (C_{pr}). The value of C_{pr} for liquid helium and liquid nitrogen are 0.758 and 0.588, respectively. Hence, we can obtain the capacitor gap size using equation 2.16. The capacitor gap size are 24 μm and 31.2 μm, respectively. However, they come from different run.

The gap size is strongly depends on the frequency jump determination. It require accurate analysis since the frequency jump occurs are caused by filling several space inside the cell. The actual frequency jump is the one that occur when the capacitor gap is filled with liquid. Any error in the size of frequency jump will lead to the error in the sensitivity ratio calculation. We used the gap size of $31.2\mu m$ in the analysis of disk mechanical resonance and third sound resonance.

5.2 Mechanical resonance result

To test the electrical connection and mechanical stability of the resonator, we took measurements of the mechanical resonance of disk vibration. The measurement had been done in liquid nitrogen and liquid helium temperature. We drive the disk with less than 1 V_{pp} X 3 drive voltage. We scanned the response in the frequency range from 5000 Hz to 18000 Hz. Besides driving both drives, we

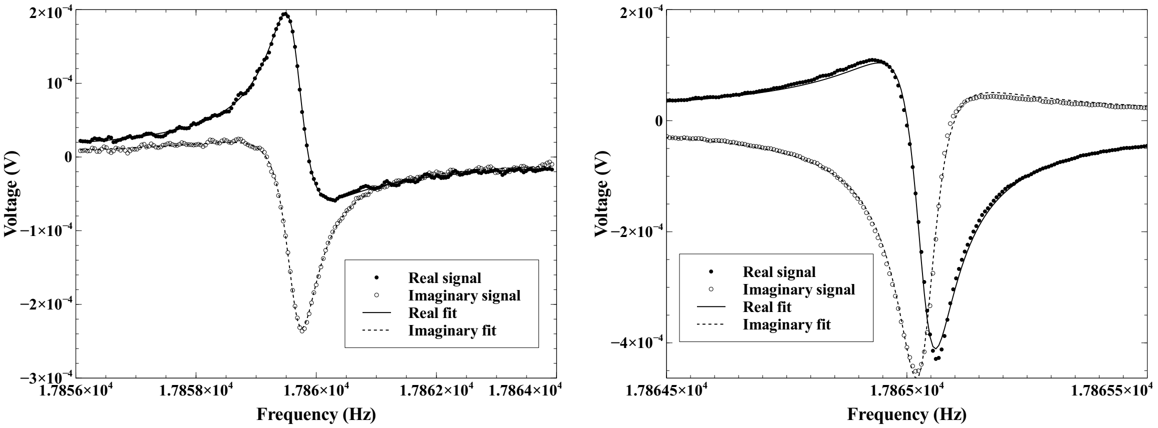

(a)

(b)

Figure 5.2: The real and imaginary parts of the mechanical resonance signal amplitude at liquid nitrogen with 0.3 V_{pp} X 3 drive voltage are shown in figure 5.2(a) and at liquid helium with 0.2 V_{pp} X 3 drive voltage are shown in figure 5.2(b).

also test the sensitivity of the drive capacitor by driving the disk with one drive.

In chapter 2, we have analyzed the possible modes of the disk that can be detected. In the experiment, we are more interested in (2,0) mode. We scan using a Visual Basic program, which is adjusted to cover an appropriate range for the scan with about 200 number of points. The figure 5.2(a) shows the mechanical resonance signal of the disk for 0.3 V_{pp} X 3 drive voltage at liquid nitrogen temperature. The frequency of the mechanical resonance is 17859.66 Hz and quality factor is 27700. The mechanical resonance signal at liquid helium temperature is shown in figure 5.2(b). The disk was driven by 0.2 V_{pp} X 3 drive voltage. The frequency of the same mechanical resonance is 17865.05 Hz and quality factor is 190000. The quality factor is increasing since the noise level is low at lower temperature. We also test the quality of drive 1 and drive 2. At a frequency of about 17865 Hz, the signal from the drive 1 and drive 2 look similar. It means that we have symmetric drive configuration, as expected from the drive electrode geometry of figure 2.1(a).

5.3 Third sound result

We took measurements of the third sound modes for different film thicknesses. We focused on the (2,1) symmetric and antisymmetric modes. The measurement had been done in the range between 0.15 K and 0.25 K film temperature. We excited the third sound mode with an electrostatic field

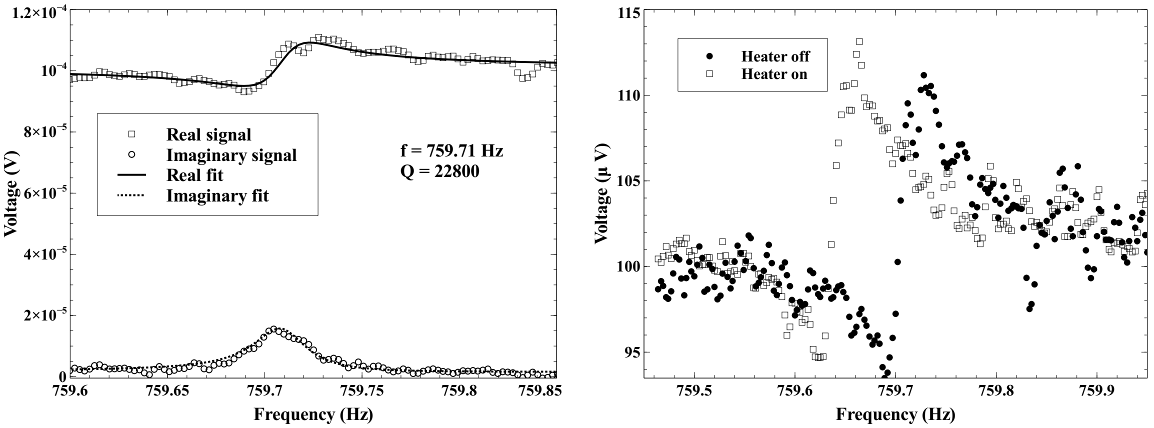

(a) (b)

Figure 5.3: (a) The third sound experimental real and imaginary signal and fitted line with heater off at 3.7 nm film thickness with 3 V_{pp} X 3 drive voltage. (b) The third sound signal with heater off and on at 3.7 nm film thickness with 3 V_{pp} X 3 drive voltage and 0.5 μW heater power. The film temperature is 0.25 K. The mode is (2,1) antisymmetric.

and scanned the possible range of third sound at a given film thickness.

5.4 Third sound amplification

The third sound amplification experiments mainly were performed on (2,1) antisymmetric mode since the mode has greater amplitude than the (2,1) symmetric mode. The figure 5.3(a) shows a third sound resonance results with the heater off with 3 V_{pp} X 3 drive voltage at 0.25 K film temperature. The film thickness is 3.7 nm. The figure 5.3(a) also shows the real parts of a resonance with the vapor source heater on and off. This shows how noisy the experimental data is. However, we are able to fit it to extract the frequency, quality factor, amplitude and phase of resonance.

Figure 5.3(b) shows the third sound signal with the vapor source heater off and on with 0.5 μ W. The heater power on corresponds to the helium atom condensation process with approximately 10^{15} atoms/second condensing into the resonating film on the disk. By condensing more helium atoms to helium film, the quality factor is increased by 9.2 %. The amplitude resonance also is increased by 1.8 %. The phase of resonance remains the same. The resonance frequency shifted to lower frequency by $9.0.10^{-3}$ %. Those numbers are coming from the averaged scan of 10 files.

5.4.1 Measurement uncertainty

The fitting program gives imperfectly fitted result to the noisy scan data. We would like to get a measurement uncertainty based on the noise level of scan data. It helps us to judge our confidence in any conclusion that there is third sound amplification by comparing the quality factor between heater off and on situations.

There are two ways to obtain the measurement uncertainty. First, we can get one by theoretical calculation that requires a complicated mathematical understanding of the fitting routine used to obtain the resonance parameters. We also can simulate the resonance signal based on the fitted paramaters. We chosed to employ the simulation method to obtain the measurement uncertainty. We generated a number of test files based on the fitted parameters from the fitting program including the noise level. The noise was generated with the random number generator in mathcad using rnorm function. We then fit the files to the resonance paramaters with the same least squares program. The number of files is 900. We got the distribution of those files parameters as well as the average value and standard deviation of the distribution.

The quality factor distribution for heater on and off for (2,1) antisymmetric at 0.25 K film temperature with 3 V_{pp} X 3 drive voltage are shown in figure 5.4(a). From this, we can include the error bar in the graph of third sound loss $\left(Q^{-1}\right)$ as a function of third sound amplitude for (2,1) symmetric and (2,1) antisymmetric mode as shown in figure 5.4(b). Third sound amplitude is proportional to the square of drive voltage. From figure 5.4(b), we can see that we should choose the drive voltage that corresponds to the 14 μW third sound amplitude. Since the data shows that the error bars of loss are lower than the other set-up. That set-up corresponds to driving the resonator with 3 V_{pp} X 3 drive voltage. This argument supports our decision to focus on 3 V_{pp} X 3 drive voltage as shown in figure 5.3(b) to observe the third sound amplification. The figure 5.4(b) also shows that the highest quality factor can be achieved by applying small drive voltage. This is an indication of low critical velocities in the third sound resonances.

Since we need to calculate the loss changes as we turn the heater power on, we need to compare the distribution of the quality factors with the heater power on and off. The distribution of the quality factors for simulated files of third sound mode on 3 nm film thickness with 3 V_{pp} X 3 drive voltage and heater power off and on is shown in figure 5.4(a). We see that the average quality factor for heater power on is bigger than heater power off. However, it is in the range of twice the standard

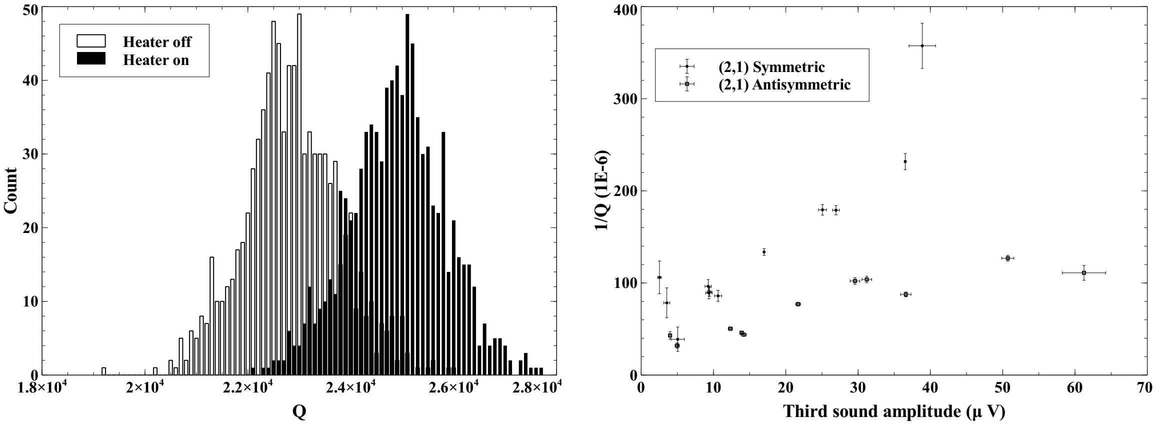

(a)

(b)

Figure 5.4: (a) The quality factor distribution of heater power off and on for the simulated files of third sound signal at 3.7 nm film thickness with 3 V_{pp} X 3 drive voltage at 0.25 K film temperature.(b) The graph of third sound loss (Q^{-1}) as a function of third sound signal amplitude.

deviation of the heater power off quality factor. The standard deviation of the heater power off quality factor is 857. We have to get the loss reduction at least twice the standard deviation of the quality factor to claim that we found the third sound amplification.

Figure 5.5(a) shows the loss as a function of heater power for experimental and theoretical third sound mode. It is a similar plot as shown in figure 1.6(a) that shows two values of theoretical quality factor at the unheated temperature ($Q_0(T_0)$). The experimental values show insignificant changes of loss as we turn the heater on. The frequency shift of figure 5.3(b) shows a film temperature rising more than predicted value from section 5.4.2. Figure 5.5(a) also shows that the (2,1) antisymmetric mode have smaller loss than (2,1) symmetric mode. Previous attempts to obtain the third sound amplification gave poor results. The quality factors are lower than current attempts. More uncertainty is observed by considering the error bar size of quality factor as shown in figure 5.5(b).

5.4.2 Frequency shift with temperature

We noticed that there is a third sound frequency shift as we turn the heater on. The shift is statistically to lower frequency. The frequency shift can be explained by assuming that temperature warming up as the heater turns on, even though we have designed and built the resonator with

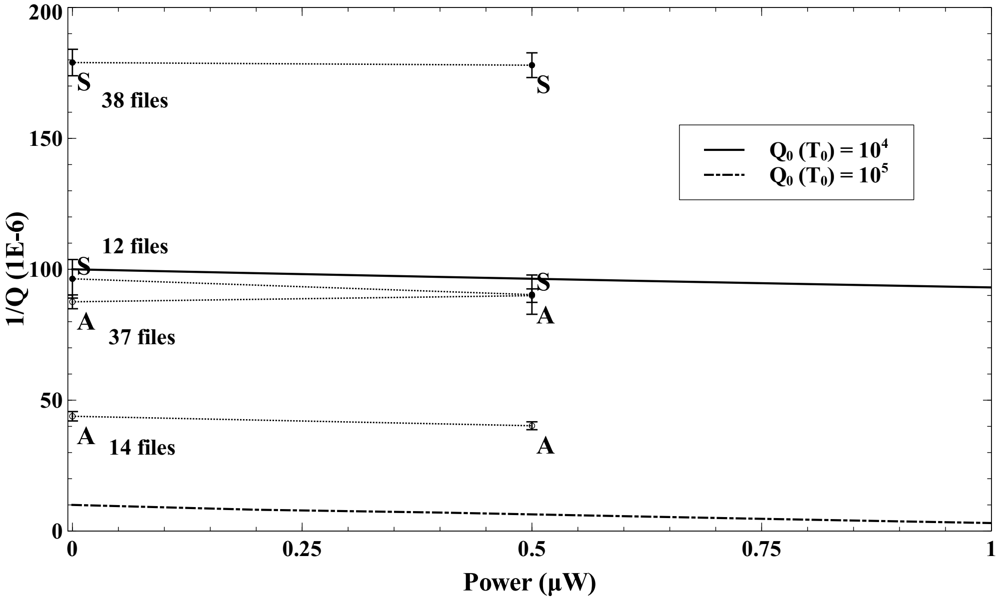

(a)

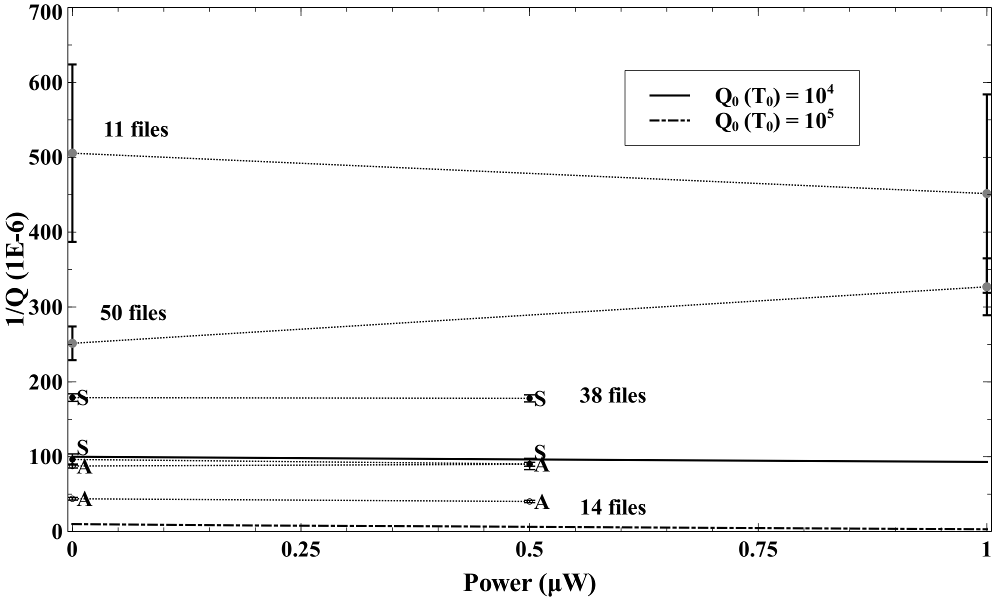

(b)

Figure 5.5: (a) The plot of experimental and theoretical prediction of third sound mode loss as a function of the heater power. The theoretical prediction using low (10^4) and high (10^5) non-thermal quality factor. The experimental third sound mode are the symmetric (S) and antisymmetric (A) mode. The error bar on the experimental results come from the simulated files of third sound signal. (b) Similar plot as figure 5.5(a) with additional two sets of third sound amplification data from Sergei Jerebets [1] and Joshua Eddinger. The quality factors of two sets additional data are lower than current attempts The error bar from those two sets of additional data comes from the quality factor distribution of the experimental data.

good thermal conductivity. The frequency shift normalized by the frequency can be expressed as

$$\frac{\Delta f}{f} = \frac{\Delta c_3}{c_3} \tag{5.1}$$

The third sound speed is proportional to the ratio between superfluid component density and total density. This ratio depends on the temperature. At 3.7 nm film thickness, the changing of that ratio is about 0.0017 per Kelvin. Another source of the temperature dependence comes from the thickening film with temperature differences due to the thermomechanical force. It can be expressed as

$$\frac{\Delta c_3}{c_3} = -3\frac{\bar{S}\Delta T}{c_3^2} \tag{5.2}$$

The result is 0.0007 per Kelvin. It is smaller than fraction changes by density calculation. It means that the temperature changes by condensation are mostly caused by changes of superfluid density ratio.

Using the superfluid density fraction function of temperature, we calculate the corresponding changes of temperature. From the third sound signal as shown in figure 5.3(b), we found that the phase shift is $6.8.10^{-2}$ Hz to the lower frequency. Hence, the temperature changes was $1.0.10^{-1}$ K. It is more than theoretical prediction value as was explained in chapter 1 which equal to $8.5.10^{-4}$ K. The theory uses the Kapitza resistance between ^{4}He and polished copper substrate. However, in the actual experiment, we used silver-coated sapphire disk. Because there is discrepancy between experimental and theoretical value of temperature changes, we can calculate the proper value of Kapitza resistance between ^{4}He and silver-coated sapphire disk. Using equation 1.25, the Kapitza resistance should be $7.0.10^7\ Km^2\,W^{-1}$ instead of $3.8.10^5\ Km^2\,W^{-1}$.

5.4.3 Scanning method to reduce the measurement bias

The frequency shifting to the low frequency might reduce the accuracy of the scanning data since the scanning process was performed from lower to higher frequency. This directional bias might shrink the peak width of the resonance. Therefore, the fitted quality factor is bigger than the unshifted scan data. To reduce the measurement bias, we scanned from higher to lower frequency and compare it with the regular scanning process. We did experiment at 3 nm film thickness with 3 V_{pp} X 3 drive voltage and 0.5 μW heater power. The fitted frequency, quality factor, amplitude and phase of the third sound signal are shown in the table 5.1.

Table 5.1: Table of frequency, quality factor, amplitude and phase of the third sound signal

	Off Low-High	On Low-High	Off High-Low	On High-Low
Frequency (Hz)	633.676	633.629	633.674	633.608
Quality factor	11512.125	9032.465	6956.6	10981.43
Amplitude (μV)	10.495	8.95	8.41	9.405
Phase	-2.47	-2.64	-2.41	-2.44

We also repeat the experiment at a thicker film. The results are

	Off Low-High	On Low-High	Off High-Low	On High-Low
Frequency (Hz)	533.756	533.687	533.745	533.678
Quality factor	9558.725	9738.426	9523.56	9535.56
Amplitude (μV)	19.82	19.3	20.18	19.58
Phase	-2.21	-2.23	-2.1	-2.20

We found the facts from two different film thicknesses that the quality factor increases and decreases in both scanning processes as we condensed the helium atoms. Hence, it is hard to conclude that frequency shifting contributes to the quality factor changes since there is inconsistency in the quality factor changes. This inconsistency is caused by a low signal to noise ratio.

5.4.4 Third Sound and disk mechanical sensitivity ratio

In chapter 2, the sensitivity ratio was calculated. Here, we find the experimental third sound sensitivity, calculated at different film thicknesses and drive voltages. As mentions there, this low sensitivity ratio comes from error propagation from the sensitivity ratio of mechanical resonance. Figure 5.6 shows the sensitivity ratio for third sound mode and disk mechanical signal. The disk mechanical experimental signal is about twice than theoretical prediction. However, the phase is off by factor of little bit bigger than π.

The third sound experimental phase of sensitivity ratio also off by factor π. The amplitude of sensitivity ratio for (2,1) antisymmetric mode is 0.5, which is better than the amplitude of sensitivity ratio for (2,1) symmetric mode. Hence, the (2,1) symmetric mode not only has bigger loss than

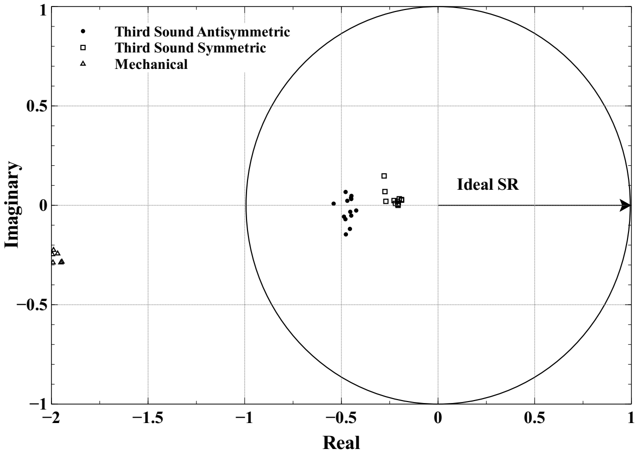

Figure 5.6: Sensitivity ratio of third sound mode and disk mechanical signal. The ideal SR is shown by arrows. The circle shows the SR with magnitude 1 for any phase.

(2,1) antisymmetric mode but also has a smaller sensitvity ratio. As discussed in chapter 5.1, the determination of which frequency we should take to calculate the capacitor gap will influence the amplitude of the sensitivity ratio. Using equation 2.42 with the information of frequency modulation of specific mode for third sound (equation 2.40) and mechanical resonance (equation 2.65), we found that the error in sensitivity ratio amplitude is proportional to the error in the capacitor gap size. The factor of π most likely comes from lack of understanding how the experimental signal and theoretical prediction match in term of the phase convention.

Chapter 6

Conclusion

Third sound amplification can be achieved by condensing helium atoms to macroscopic flow velocity state of the third sound mode. By having a high quality factor, the third sound amplification can be significantly observed. We have calculated all possible problems to get an estimation of the optimum condition that the self oscillation condition happen.

The high quality factor can be achieved by carefully assembling the resonator. We also developed the electronic detection system to reduce the mechanical vibration that could contribute to the noise by built the new bias plate. We had a clean capacitor gap, free of dust that could bridge the electrode plate and the disk. We also calculated the rising of liquid level in the capillary. It is important to predict the time when the capacitor gap began to be filled with the liquid.

There is a discrepancy between the experimental third sound signal amplitude and phase, and the theoretical prediction. It comes from a lack of understanding of the electronic system. We have compiled data of the drive voltage output from the 3X-Box. It helps us to get more accurate theoretical prediction of third sound and disk mechanical resonance. We had investigated the tunnel diode frequency and the quality factor as a function of temperature. This experiment supported the capacitor calculation for investigating the quality of electrical connection. We also reduced the external frequency interference to the tunnel diode frequency by adding filter capacitor parallel to the drive capacitor. The minimum of external signal in the path of drive capacitor with the 3X-Box and feedback on shows improvement compare to without filter capacitor set-up. The calculation of the stray capacitance has been done. The stray capacitance value is important for calculating the actual capacitor gap size. The gap size can be calculated by changing the tunnel diode frequency as we fill the capacitor gap with liquid nitrogen and liquid helium. The gap size strongly depends on the determination of which the actual the TDO frequency jump is.

The low signal to noise ratio increased the measurement uncertainty. We got the measurement uncertainty by calculating the standard deviation of simulated files based on the fitted parameter of the actual averaged third sound signal. The third sound quality factor amplification is greater than the measurement uncertainty. However, it is not big enough to be claimed as an amplification.

We found that as the heater power was turned on, the film temperature increased. The changes of temperature can be calculated from shifted the third sound signal frequency. This process is dominated by changes of the superfluid component density to the total density as a function of temperature. The temperature change is greater than theoretical prediction which used Kapitza resistance between ^{4}He and copper substrate.

Appendices

Appendix A

Partial Entropy

A.1 Third Sound Equation of Motion

Third sound has a mechanical component (kinetic energy and van der Waals potential energy) as well as a thermal component associated with the concentration and dilution of thermal excitations. Like second sound, the third sound also exhibits propagating thermal fluctuations, but the nature of thermal excitations [16] [17] and constraint on their mechanical coupling give the thermomechanical effects within the film some unexpected behavior.

We begin by describing the hydrodynamics equations of motion for third sound and illuminating the subtley of Bergman's "partial entropy" [18]. We then present results of a numerical computation of the partial entropy for a simplified set of excitations [16] for the purposes of illustrating its distinction from a generic "film entropy" which pervaded the subsequent third sound literature [19]. Variational approaches to third sound [20] [21] correctly include the physics, but as the understanding of film excitations improves [17], we re-emphasized the hydrodynamic consequence of partial entropy in the context of the two-fluid model.

We express Bergman's equation of motion in a form that more intuitively separates the various terms according to their function since our focus is on the concept of partial entropy [18]. The calculation has been done in one dimension with all variables approproately film-averaged. The equation of motions are :

$$\rho\frac{\partial \eta}{\partial t} = -\rho_s h\frac{\partial v}{\partial x} + J_m \tag{A.1}$$

$$\rho h C \frac{\partial \tau}{\partial t} = \rho_s h T \bar{S} \frac{\partial v}{\partial x} - L J_m - J_Q \tag{A.2}$$

$$\frac{\partial v}{\partial t} = -g \frac{\partial h}{\partial x} + \bar{S} \nabla \tau \tag{A.3}$$

which η, τ and v are the oscillating thickness and temperature, and superflow, respectively. We also take consideration that v_n =0.

Equation A.1 expresses conservation of mass in the incompressible of film thickness h including superflow, $\rho_s v$, and a mass flux from the film into the vapor, J_m. Equation A.2 expresses conservation of thermal energy derived from the consideration of entropy. Entropy is carried by the normal component. In the third sound mode, the entropy can be diluted by superflow, or otherwise changed by heat flux through evaporative latent heat, LJ_m, and heat conduction from the film to the substrate and the gas, J_Q. The equation A.3 expresses conservation of mechanical energy in the form of Newton's law. The van der Waals acceleration at the film surface is g. The last term in the right hand side of equation A.3 is the thermomechanical force due to thermal gradient.

In his works, Bergman include L in the several terms of equation of motion. It is not very transparent. It results from a careful derivation from the two fluid model including motion of the normal component. Since v_n is zero in the third sound mode, it is more transparanet to put the L into the single evaporative term in equation A.2. The partial entropy per mass denoted by S in both equations, comes about through consideration of a fixed areal patch looking down perpendicularly upon the film. In equation A.2, for example, the total entropy per area, assumed to be a state variable dependent only on thickness and temperature, $\Sigma(h,T)$, has two corresponding partial derivatives ress arising from its derivative: thermodynamics functions arising from its derivative:

$$\left(\frac{\partial \Sigma}{\partial T}\right)_h = \frac{\rho h C}{T} \tag{A.4a}$$

$$\left(\frac{\partial \Sigma}{\partial h}\right)_T = \rho \bar{S} \tag{A.4b}$$

which C is the film heat capacity per mass, but $\bar{S}$ rather than "film averaged entropy", is a new quantity combining all the effect of a changing film thickness into the dilution of entropy. A similar consideration produces the partial entropy in equation A.3. In terms of the more intuitive film entropy per mass, S, the partial entropy is

$$\bar{S} = \frac{\partial(hS)}{\partial h} \tag{A.5}$$

This form for the entropy is explicitly pointed out as separate from the other film averaged quantities in Bergman's derivation, but seems not to have been properly passed on by subsequent authors. At low temperatures, the difference between the film entropy and the partial entropy can be significant. The differences result from the nature of thermal excitations that dominate the normal fluid component, and depend strongly on both the film thickness and temperature.

The solutions to the equations of motion are rather involved with the detailed substrate and vapor interactions included for the geometry of interest. For the purpose of illustrating how the partial entropy comes in, it suffices to say that thermomechanical terms appear in two primary forms associated with the adiabatic limit. First, the temperature oscillations in the adiabatic film, and second, the magnitude of the thermomechanical restoring force. Those forms can be expressed as

$$\frac{\tau}{T} = -\frac{\bar{S}}{C}\frac{\eta}{h} \tag{A.6a}$$

$$c_h^2 = \frac{\rho_s}{\rho}\frac{T\bar{S}^2}{C} \tag{A.6b}$$

The equation A.6b also known as the fifth sound speed equation [19] [22] with the partial entropy substituted. The influence of each of these terms is reduced (and phase shifted) as a result of vapor and substrate coupling as the temperature rises, but the presence of the partial entropy remains linked to these terms.

A.2 Film Thermodynamics

There are 3 excitation spectrum exist in the film with low temperature (T<0.75 K) and not too thin film thicknesses (h>1 nm). They are

1. The surface wave mode (third sound/ripplon spectrum)
2. bulk-like film phonon branches
3. bulk rotons

The surface wave mode can be dominated by third sound mode or ripplon (quantized capillary) wave mode. The ripplon wave is the wave that exist in the free surface of superfluid Helium-4. The dispersion relation of the surface wave mode with surface tension γ is

$$\omega_{surf}^2 = tanh(qh)\left(gq + \frac{\gamma q^3}{\rho}\right) \tag{A.7}$$

The first term of equation A.7 express the third sound spectrum. The capillary wave spectrum is expressed in second term.

The capillary mode is damped in the direction down into the liquid, the phonon mode become dominant in the liquid. Its spectrum is

$$\omega_n^2 = c_1^2\left(\left(\frac{(n-\frac{1}{2})}{h}\right)^2 + q^2\right) \tag{A.8}$$

The n indeces refers to the phonon branch mode. The maximum number of phonon branches to include in the thermodynamics calculation depends on temperature. A sufficient number of phonon modes were included to assure quantitative accuracy for T< 0.75 K. The speed of sound in the liquid helium is c_1. The wavenumber q can be expressed as the sum of wavenumber in the x and y direction.

When the temperature is raising up, the roton spectrum start to be included in the calculation. It also important for the purposes of connecting to the thick film limit. The roton spectrum is

$$\omega = \omega_{gap} + \hbar\frac{(q-q_0)^2}{2m_r} \tag{A.9}$$

which ω_{gap}, q_0 and m_r are 8.65 K, 19.1 nm^{-1} and 0.16 m$_{^4He}$, respectively.

Layer modes [17] have not been included for simplicity, but would be important in thinner films. Those three spectra were integrated numerically with the Planck distribution to obtain the thermodynamics functions for the film specific entropy and specific heat. The partial entropy was evaluated using equation. The energy for each spectrum is

$$U = \sum_j \frac{\hbar\omega_j}{e^{\frac{\hbar\omega_j}{kT}} - 1} \tag{A.10}$$

The ripplon energy is calculated in 3D since the ripplon exist at the surface. The phonon spectrum shown in equation A.8 clearly explain that the calculation of the energy is in x-y plane (2D). However, the 3D calculation is needed for energy of roton since it is a bulk excitation.

The energy per mass for 2D calculation is

$$u = \frac{1}{\rho h L^2} \int_0^\infty \frac{\hbar\omega(q)}{e^{\frac{\hbar\omega(q)}{K_b T}} - 1} \frac{1}{\left(\frac{2\pi}{L}\right)^2} 2\pi q \, dq \tag{A.11}$$

The energy per mass for 3D calculation is

$$u = \frac{1}{\rho L^3} \int_0^\infty \frac{\hbar\omega(q)}{e^{\frac{\hbar\omega(q)}{K_b T}} - 1} \frac{1}{\left(\frac{2\pi}{L}\right)^3} 4\pi q^2 \, dq \tag{A.12}$$

The energy per mass for 3 elementary excitations are shown in figure A.1.

Figure A.2(a) and A.2(b) show the effect of the partial entropy for a range of film thickness expressed in terms of quantities relevant to the third sound equations of motion.

A.3 Discussion

The partial entropy emerges from the two fluid model applied to films due to unique combination of the mechanical constraint imposed by the free surface and the thickness dependence of the excitations themselves. As the volume available to excitations expands or contracts with the movement of the free surface, the nature of the excitations involved dictates the character of thermal response. Three idealized cases can help clarify this concept, again taken in the adiabatic sound limit and with the simplified excitation spectrum to emphasize the role of the partial entropy. All three cases are visible in the numeric data of figures A.2(a) and A.2(b).

Consider first the case where the film is taken as a slab of bulk as would be expected for thick films at high temperatures. Since the entropy per area grows proportional to the film thickness, the partial entropy per mass from equation A.5 is just the bulk entropy per mass, $\bar{S} = S_{bulk}$. At this limit, the dominant excitations are phonon and roton. As mass and heat move around in the film, the intensive quality of the thermal excitations as the normal component dominates. This is perhaps the historic reference frame that allowed film entropy to displace partial entropy in the literature.

Next, consider low temperatures where the very long-wave free-surface excitations are populated. This is the third sound limit where capillarity is negligible compared to the Van de Waals force. With $\omega = q\sqrt{g(h)h}$, the thermodynamics can be analytically determined. The partial entropy with $g(h) \propto h^{-4}$ is $\bar{S} = 3S$. This limit has a partial entropy significantly greater than the film entropy. Converging superfluid at a wave crest not only dilutes the normal component, but

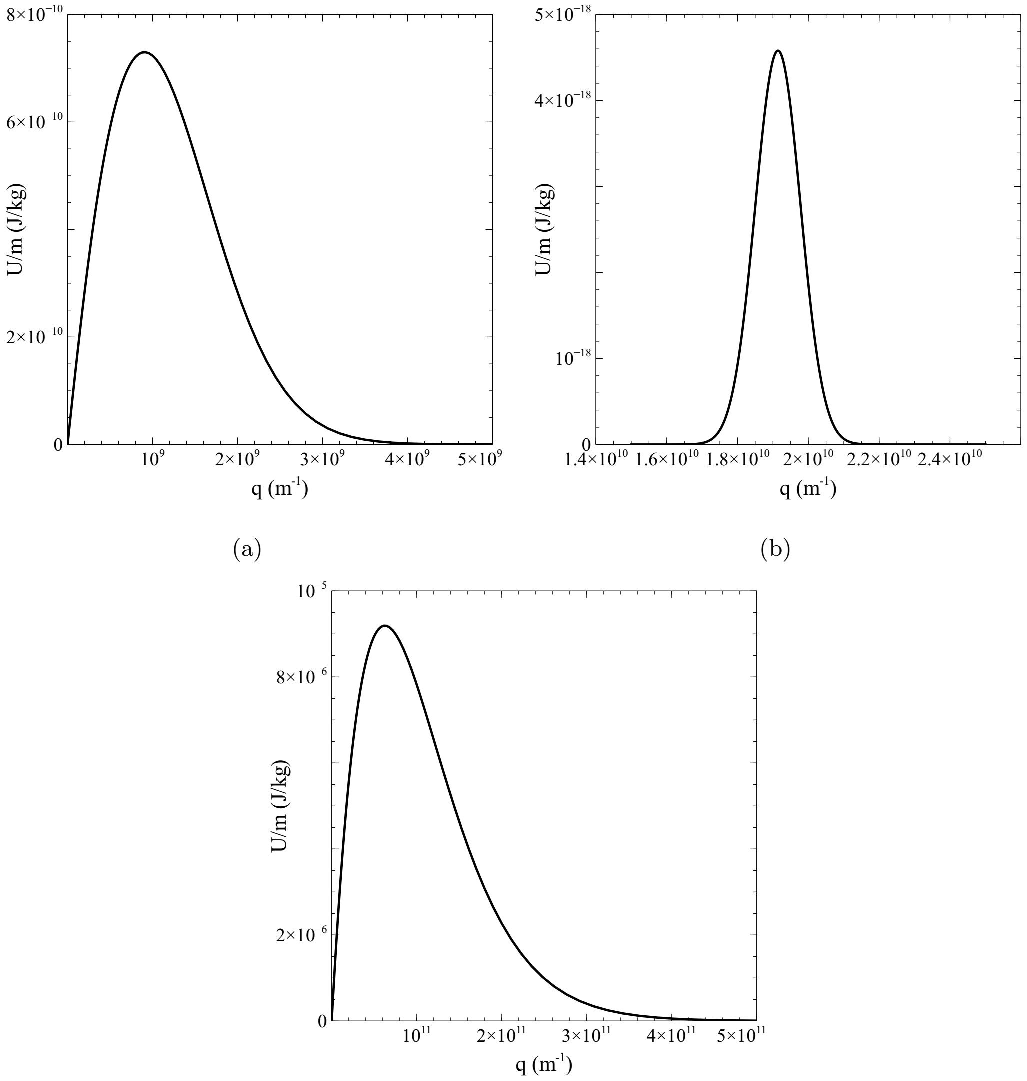

(a)

(b)

(c)

Figure A.1: The energy per mass of 3 elementary excitations in the superfluid Helium-4 as a function of wavenumber. There are ripplon, roton and phonon first branch as shown in figure A.1(a), A.1(b) and A.1(c), respectively. The temperature is 0.3 K and the film thickness is 3 nm.

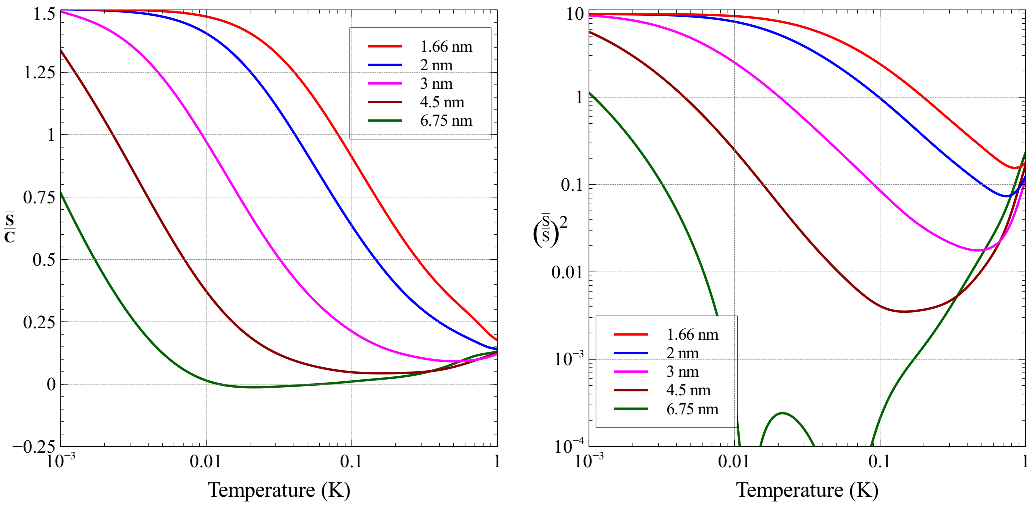

(a) (b)

Figure A.2: (a) The ratio of partial entropy to the heat capacity as a function of temperature for five film thicknesses giving the adiabatic temperature oscillations for third sound. (b) The ratio squared of partial entropy the entropy as a function of temperature for five film thicknesses. They are representing the effect on the thermomechanical force. The film thicknesses are 1.66, 2, 3, 4.5 and 6.75 nm.

softens the excitation spectrum as the film thickens. The partial entropy expresses this constraint analogous to adiabatic demagnetization.

Finally, consider the case where *all* of the thermal energy is associated with the surface excitations having no connection to the thickness. This would be the case of moderate temperature and thickness dominated by high-q ripplons. This begins around 0.5 K and extends down to where the ripplons begin to sense the substrate. Here, the entropy per area (σ) is independent of h. The entropy is

$$S = \frac{\sigma}{\rho h} \tag{A.13}$$

The partial entropy from equation A.5 is 0. This would also apply to the layer modes.

Surprisingly, the partial entropy for films with $h > 6.36$ nm has a negative value. Figure A.3 maps this range of thickness and temperature for our simplified excitation spectrum. The curve line is the line temperature and thickness when the partial entropy become zero. It become zero as the derivative of excitation frequency respect to thickness become zero. We have investigated the behavior of derivative of excitation frequency in the region where the surface ripplons dominate.

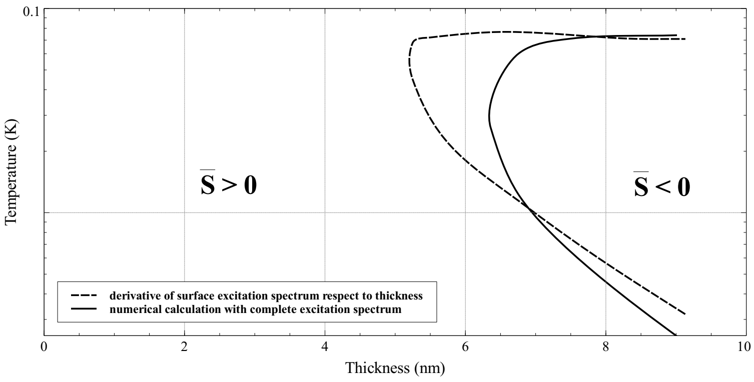

Figure A.3: The region within the solid arc shows the range of negative partial entropy predicted by the simplified excitation spectrum. The shaded region is described in the text. The red and blue lines are the function of $T = To\left(\frac{h}{ho}\right)^{-3/2}$ and $T = To\left(\frac{h}{ho}\right)^{-7/2}$, respectively. To is 0.135 K and ho is 2.135 nm.

For $\omega = \alpha(h)q$, the energy per mass in 2D is

$$u \approx \frac{T^3}{h\alpha(h)^2} \tag{A.14}$$

The entropy is

$$S \approx \frac{T^2}{h\alpha(h)^2} \tag{A.15}$$

Hence, the partial entropy from the equation A.5 is

$$\bar{S} \approx \frac{\partial}{\partial h}\left(\frac{T^2}{\alpha(h)^2}\right) = -2S\frac{h}{\alpha(h)}\frac{\partial}{\partial h}\alpha(h) \tag{A.16}$$

We can see from the equation A.16 that the partial entropy becomes negative as the derivative of excitation velocity respect to thickness becomes positive. We create contour plot of the derivative of excitation frequency respect to thickness as shown in figure A.4. We are interested in the line when the derivative becomes zero. This is related to the zero partial entropy. The temperature corresponds to that line can be determined by looking for the maximum value of $\frac{du}{dq}$ versus q graph. The figure A.3 also shows the temperature and thickness of zero partial entropy. The line shape for two type of calculations are similar. The only different is the zero partial entropy for the derivative calculation is sooner than for the complete excitation numerical calculation. Note that at negative partial entropy, both the thermomechanical force and the temperature oscillations in third sound would be reversed.

Equation A.16 also explain the behaviour of the liquid helium at low temperature limit. At this limit, the liquid helium can be treated as 2D film. The entropy is a half of the heat capacity.

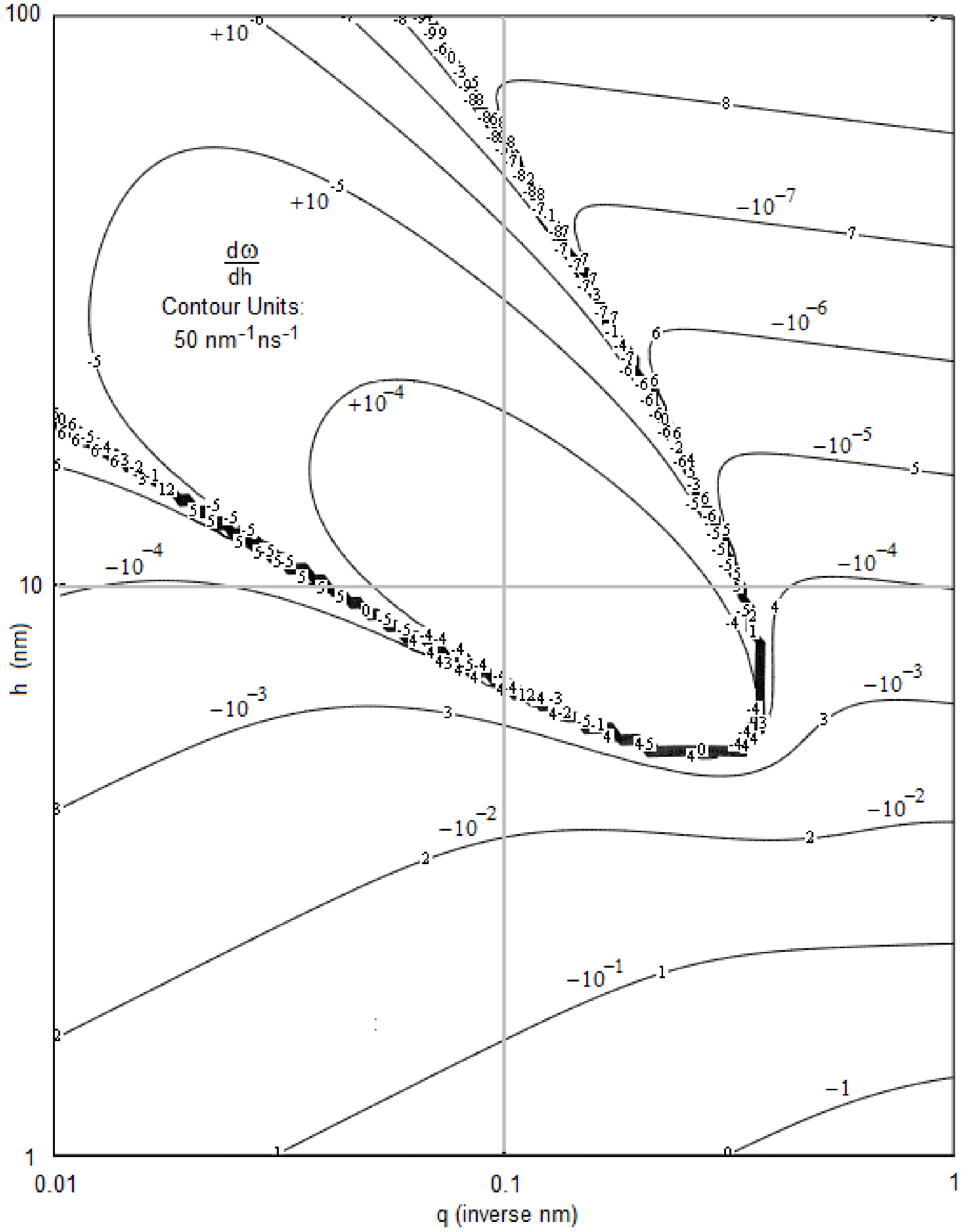

Figure A.4: The contour plot of the derivative of excitation frequency respect to thickness.

The $\alpha(h)$ which is equal to Van der Waals acceleration for third sound frequency is proportional to $h^{-3/2}$. Hence, the partial entropy is three times the entropy. At this limit, the ratio of partial entropy and the heat capacity is three-half as shown in figure A.2(a).

A.4 Conclusion

A proper treatment of partial entropy within two-fluid third sound hydrodynamics significantly alters the magnitude of thermal effects where surface excitations dominate the population of thermal excitations. The distinction between film entropy is smaller than the film entropy for intermediate thickness and temperatures, and larger than the film entropy for all thicknesses at very low temperatures. These conclusions are based on the qualitative character of the excitations and are not limited to our simplied spectrum.

The region of negative partial entropy at intermediate thickness and temperature is however, susceptible to the details of the excitation spectrum. Its occurrence in the simple film-ripplon spectrum illustrates how the reversal of thermomechanical attributes of the two-fluid model could occur in films. In spite of the reversal, the sign of the modified fifth sound speed remains positive under all conditions.

Appendix B

Stray capacitance

We calculated the detail of the several stray capacitances based on their geometry. It helps us to understand the possible value of the total stray capacitance. They are

1. Capacitance between the disk post and the disk.

   The disk post is glued to the disk. The glue may crack as temperature increases or decreases. The crack can open the connection between post and plate. We calculated its capacitance using reasonable dimensions. Xiang calculated the perpendicular plates capacitance [23]. The figure B.1 shows the configuration of two perpendicular plates. The total capacitance per unit length is

   $$c = c_{in} + c_{out} \tag{B.1}$$

   which c_{in} and c_{out} are the capacitance per unit length between the inner part of the perpendicular plate and the capacitance per unit length between the outer part of the perpendicular plate, respectively.

   The solution for this configuration is obtained by conformal mapping the original plane into another plane that has two parallel plate capacitors, since the solution for that plane is already known. c_{in} and c_{out} are

   $$c_{in} = \epsilon \frac{K'\left(k_{R\,in}\right)}{K\left(k_{R\,in}\right)} \tag{B.2a}$$

   $$c_{out} = \epsilon \frac{K'\left(k_{R\,out}\right)}{K\left(k_{R\,out}\right)} \tag{B.2b}$$

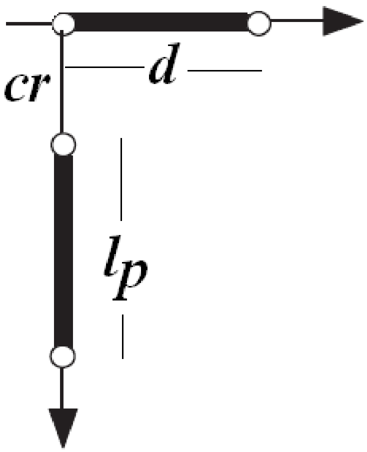

Figure B.1: The configuration of the perpendicular capacitor to model the capacitance between the disk and the disk post due to glue crack in the connection point.

which $K(k)$ is the complete elliptic integral of the first kind. The identity of the complete eliiptical integral is

$$K'(k) = K(k') \tag{B.3}$$

which k' is the complementary modulus of k. The modulus and the complementary modulus are

$$k_{R\,in} = \frac{cr}{lp + cr}\sqrt{\frac{(lp+cr)^2 + d^2}{cr^2 + d^2}} \tag{B.4a}$$

$$k_{R\,out} = \sqrt{\frac{cr^{(2/3)}\left((lp+cr)^{(2/3)} + d^{(2/3)}\right)}{(lp+cr)^{(2/3)}\left(cr^{(2/3)} + d^{(2/3)}\right)}} \tag{B.4b}$$

$$k'_{R\,in} = \sqrt{1 - k^2_{R\,in}} \tag{B.4c}$$

$$k'_{R\,out} = \sqrt{1 - k^2_{R\,out}} \tag{B.4d}$$

which cr, lp and d are the glue crack gap, the effective disk post height and the effective disk length, respectively. The effective disk post height is $2r_{post}$ which r_{post} is the post radius. The effective disk length is the space between the edge of the electrode plate hole (r_{hole}) and the disk post. It is

$$d = \frac{1}{2}\left(r_{hole} - r_{post}\right) \tag{B.5}$$

Hence, the capacitance per unit length of the perpendicular plate is :

$$c = \epsilon \left(\frac{K'(k_{R\,in})}{K(k_{R\,in})} + \frac{K'(k_{R\,out})}{K(k_{R\,out})} \right) \tag{B.6}$$

Since the disk post has a circular shape, we assume that we can unfold it to be a sheet-like shape. The sheet length is the disk post perimeter $2\pi r_{post}$. Hence, the total capacitance is

$$C = c\ (2\,\pi\, r_{post}) \tag{B.7}$$

We can calculate the value of the total capacitance as a function of the glue crack gap cr. Hence, we can have a good estimation of what the capacitance should be if there is glue crack in the joint point between the disk post and the disk. For example, the capacitance will be 1.4 fF when the cell empty and the glue crack length is 0.3 μm (1/10 of the capacitor gap size).

2. Capacitance between evaporator ring and the disk

The evaporator ring is located 1.3 mm above the disk. Its diameter is 9 mm. We used conformal mapping to map the equipotensial line. The equipotensial line is the real part of the complex potential.

$$V = V_0\, Re \left(\frac{ln \frac{z+c}{z-c}}{ln \frac{c+h}{c-h}} \right) \tag{B.8}$$

which z is $x + iy$, V_0 is the potential amplitude, h is the distance between the surface of the disk and the ring, c is $\sqrt{h(h+D)}$ and D is the evaporator wire diamater. The imaginary part of the complex potential describes the stream function. This function can be used to calculate the total charge that can be stored in the capacitor.

$$Q = \epsilon_0\, W\, V_0\, Im \left(\frac{ln \frac{z+c}{z-c}}{ln \frac{c+h}{c-h}} \right) \tag{B.9}$$

which W is the disk diameter. The equation B.9 is evaluated at x=0 and y from $-\infty$ to $+\infty$ since the disk is located along the y axis. Hence, we can rewrite equation B.9 into

$$Q = \epsilon_0\, W\, V_0\, Im \left(\frac{ln \frac{iy+c}{iy-c} - ln - \frac{iy+c}{iy-c}}{ln \frac{c+h}{c-h}} \right) \tag{B.10}$$

In the nominator of the above equation we have

$$ln \frac{iy+c}{iy-c} - ln - \frac{iy+c}{iy-c} = ln\,(-1) = i\pi \tag{B.11}$$

Hence, the total charge is

$$Q = \frac{\epsilon_0 \, W \, V_0 \, \pi}{ln\left(\frac{c+h}{c-h}\right)} \tag{B.12}$$

The capacitance equation is $Q = C \, V_0$. Hence, the capacitance is

$$C = \frac{\epsilon_0 \, W \, \pi}{ln\left(\frac{c+h}{c-h}\right)} \tag{B.13}$$

The denominator can be write as

$$ln\left(\frac{\sqrt{h(h+D)}+h}{\sqrt{h(h+D)}-h}\right) = y \tag{B.14}$$

We divide the right hand side of the equation above by h/h to be

$$y = ln\left(\frac{\sqrt{(1+D/h)}+1}{\sqrt{(1+D/h)}-1}\right) \tag{B.15}$$

The equation above can be expressed as

$$\sqrt{1+D/h}\,(e^y - 1) = 1 + e^y \tag{B.16}$$

Using the relationship identity of $tanh(x)$ to the exponential function, we can write the above equation as

$$tanh^2(y/2) = \frac{1}{1+D/h} \tag{B.17}$$

Since $tanh(x) = sinh(x)/cosh(x)$ and $tanh(x) = -1 \, tanh(ix)$, we have

$$cosh(y/2) = \sqrt{\frac{1+D/h}{D/h}} \tag{B.18}$$

Hence, y is

$$y = 2 \, cosh^{-1}\sqrt{1+h/D} = ln\left(\frac{\sqrt{h(h+D)}+h}{\sqrt{h(h+D)}-h}\right) \tag{B.19}$$

We substitute equation B.19 into equation B.13 to get the capacitance between evaporator ring and the plate equation. It is

$$C = \frac{\pi \epsilon_o W}{cosh^{-1}\left(1+\frac{h}{D}\right)} \tag{B.20}$$

The capacitance is 0.3 pF when the cell is empty.

3. capacitance between ring holder and the plate

   The ring holder is a metal circle that holds the evaporator ring on the top of the plate. Because of that configuration, we can write the capacitance between the ring holder and the plate as

   $$C = \frac{\epsilon_o A}{d} \tag{B.21}$$

   which d is the distance between the ring holder and the plate is 2.5 mm. The capacitance is 0.4 pF.

Hence, we calculated the total stray capacitance that includes the three capacitances and coupling capacitance as mentioned in the chapter 4. The total capacitance is about 2.2 pF.

Bibliography

[1] Jerebets, S. *Resonator Design for the Observation of Third Sound Amplification by Stimulated Condensation (TASC).* PhD thesis, Wesleyan University, (2002).

[2] Annett, J. F. *Superconductivity, Superfluids and Condensates.* OXFORD University Press, (2004).

[3] Penrose, O. and Onsager, L. *Physical Review* **104**, 576 (1956).

[4] Takeo Matsubara, Akira Morita, N. H. *Progress of Theoretical Physics* **16**, 447 (1956).

[5] D. R. Tilley, J. T. *Superfluidity and Superconductivity.* Institute of Physics Publishing, (1970).

[6] Tisza, L. *Nature* **141**, 913 (1938).

[7] Landau, L. *Physical Review* **60**, 356 (1941).

[8] Atkins, K. *Physical Review* **113**, 962 (1959).

[9] C.W.F. Everitt, K. A. and Denenstein, A. *Physical Review* **136** (1964).

[10] Landau, L. D. and Lifshitz, E. M. *EFluid Mechanics.* Pergamon Press, (1959).

[11] R. P. Henkel, E. N. S. and Reppy, J. D. *Physical Review Letters* **23** (1969).

[12] Feynman, R. P. *Physical Review* **94**, 262 (1954).

[13] Lounasmaa, O. V. *Experimental Principles and Methods Below 1K.* Academic Press, (1974).

[14] Leissa, A. W. *Vibration of Plates.* NASA, (1969).

[15] J.H. Scholtz, E. M. and Rudnick, I. *Physical Review Letter* **32**, 147 (1974).

[16] Saam, W. and Cole, M. W. *Physical Review B* **11**, 1086 (1975).

[17] C.E. Campbell, B.E. Clements, E. K. M. S. *Physical Review B* **55**, 3769 (1977).

[18] Bergman, D. *Physical Review* **188**, 370 (1969).

[19] Putterman, S. *Superfluid Hydrodynamics.* North-Holland, (1974).

[20] J.E. Rutledge, W. M. and Mochel, J. *Physical Review B* **18**, 2155 (1978).

[21] Krotscheck, E. and Miller, M. *Physical Review B* **73**, 134514 (2006).

[22] Isadore Rudnick, Jay Maynard, G. W. S. P. *Physical Review B* **20**, 1934 (1979).

[23] Xiang, Y. *Journal of Electrostatics* **66**, 366 (2008).